DEVELOPMENT OF A CIRCULATING FLUIDIZED BED REACTOR MODEL FOR THE FAST PYROLYSIS OF BIOMASS FOR PROCESS SIMULATION

by

Anna A. Trendewicz

A thesis submitted to the Faculty and the Board of Trustees of the Colorado School of Mines in partial fulfillment of the requirements for the degree of Doctor of Philosophy (Mechanical Engineering).

Golden, Colorado

Date _____

Signed: _____
Anna A. Trendewicz

Signed: _____
Robert J. Braun
Thesis Advisor

Signed: _____
Abhijit Dutta
Thesis Advisor

Golden, Colorado

Date _____

Signed: _____
Gregory Jackson
Professor and Head
Department of Mechanical Engineering

ABSTRACT

Biomass fast pyrolysis is one of the possible methods for converting solid biomass into liquid fuels or chemicals. Obtaining liquid fuels (especially for transportation) from renewable sources is of increasing interest due to concerns about economics and environmental impact of using depleting fossil fuels. The viability of fast pyrolysis pathways to liquid fuels is typically assessed by performing system-wide techno-economic analyses (TEAs) of biorefineries. This analysis requires system models capable of predicting fast pyrolysis products and process energy requirements from different biomass feedstocks (chemical composition, alkali) and under different operating conditions (temperature, particle size, residence time). The TEA system models currently used are computationally simple and based on a small amount of experimental results which significantly limits their utility. The goal of this work is to develop an engineering reactor model for future integration with process simulations in order to gain a better understanding of the impact of fluid dynamics, heat transfer and reaction kinetics on the products yields and composition. The current work addresses the issues of providing an engineering approximation of the effects of biomass composition variations, residence time and reaction temperature on pyrolysis process by incorporating the following features: (1) a flexible pyrolysis reaction mechanism inclusive of the catalytic effect of intrinsic contaminants, (2) one-dimensional, steady-state momentum balance for solids-gas flow, and (3) one-dimensional, steady-state energy equation. Simulation results regarding pyrolysis product yields are validated with the available experimental results and literature data. The fluid dynamics results are verified with the results from a transient, 2-D reactor model developed in MFIX. The simplifying assumptions related to the biomass particle geometry and properties are verified by comparison with simulation results from a 3-D, microstructure biomass particle model. The results show that the two most influential parameters on product yields and composition are the reaction temperature and biomass

composition. Changing the remaining operating parameters (besides reaction temperature and biomass feedstock) causes changes in velocity profiles, temperature profiles, point of reaction onset, and reaction rates. However, the final product yields at the reactor outlet remain unchanged provided that the residence time is sufficient for full conversion. The employed reaction model gives good predictions of product classes for the low ash content feedstocks such as pine, however it significantly overpredicts the organics yields from high ash content feedstocks. This is because the catalytic effect of intrinsic contaminants is not included in the reactions. Therefore, the reaction mechanism was corrected for potassium as a representative of the intrinsic contaminants in order to improve the predictive capabilities of the model from feedstocks with high ash content. Validation and verification efforts show that the temperature profiles, product yields and composition are in good agreement with higher order models and experimental data. However, the model overpredicts particle velocities and consequently underpredicts pressure drop, as the effect of particle clustering is not captured in the 1-D, steady-state flow representation. Therefore, a drag model adjustment is required for improved particle residence time predictions. The developed model provides valuable information about the temperature distribution, velocity profiles and species concentration profiles along the rector at a low computational cost and it offers better product predictions compared to the yield reactor models used in TEAs.

TABLE OF CONTENTS

LIST OF FIGURES

LIST OF TABLES

LIST OF SYMBOLS

Nusselt number . . . . . Nu

Prandtl number . . . . . Pr

Reynolds number . . . . . Re

activation energy . . . . . E_a

coefficient of restitution . . . . . e_{s-b}

density . . . . . ρ

dynamic viscosity . . . . . μ

empirical drag coefficient . . . . . C_d

enthalpy of reaction for reaction j . . . . . ΔH_j

friction coefficient . . . . . f

gas-to-biomass ratio . . . . . $R_{gas/bio}$

gravity . . . . . g

interphase momentum exchange coefficient . . . . . β

mass flow rate of species i . . . . . M_i

overall heat transfer coefficient between biomass and gas . . . . . h_{bg}

overall heat transfer coefficient between sand and gas . . . . . h_{sg}

particle collision coefficient . . . . . F_{s-b}

particle diameter . . . . . d_p

particle friction coefficient . . . . . $c_{f,s-b}$

pre-exponent . . . . . k

pressure . . . . . p

radial distribution function at contact . . . . . $g_{0,s-b}$

reaction rate for reaction j . . . . . R_j

reactor diameter . . . . . $D_{reactor}$

reactor height . . . . . $H_{reactor}$

sand-to-biomass ratio . . . . . $R_{sand/bio}$

specific heat . . . . . c_p

stoichiometric coefficient for species i in reaction j . . . . . $\nu_{i,j}$

temperature . . . . . T

terminal velocity of the solids . . . . . $V_{r,s-b}$

thermal conductivity of the gas . . . . . k_g

velocity v

volume fraction . . . . . ϵ

LIST OF ABBREVIATIONS

Circlulating Fluidized Bed Reactor	CFB
Molecular Beam Mass Spectrometry	MBMS
tons per day	TPD
refuse derived fuel	RDF
direct numerical simulations	DNS
constructive solid geometry	CSG
computational fluid dynamics	CFD
partial differential equation	PDE
multiphase flow interactions with exchanges	MFIX
two-fluid model	TFM
no-slip wall	NSW
partial-slip wall	PSW
vapor phase upgrading	VPU

ACKNOWLEDGMENTS

I would like to thank my advisor Robert Braun and co-advisor Abhijit Dutta for their advice and commitment to completing this project. I would also like to thank Dr. Robert Evans for his help with the experimental work and guidance, which was crucial in analyzing and interpreting the experimental data. I would like to thank Dr. Jack Ziegler and Dr. Peter Ciesielski for collaboration which added great value to this project by providing simulation results for model verification. In addition many thanks to Dr. Pejman Kazempor for his help with programing in gPROMS. I would also like to thank my parents for their tremendous support during the entire process. In addition, special thanks to all the great friends from NREL: Paul Ndione, Petr Zvolsky, Smritikana Dutta, Carolin Ulbricht, Benjamin Lee, Sergio Casimiro, Edwin Wojdarernko, Stefan Oosterhaut, Christopher Kinchin, Jeremy Fields, Stephanie Essig, Sebastian Siol, Henning Doscher and Aleksiej Mialisin who are and will always remain great companions. Lastly special thanks to my friends from CSM: Cooper Minetti, Daniel Fullerton, Arlen Kostival, Andreas Wiedermann, J ustin Blasi, Christopher Wendel, Kevin Albrecht, Alexis Dubois, and Gladys Anyenya for the great, cheerful times together.

CHAPTER 1

INTRODUCTION

Biomass fast pyrolysis is a potentially attractive method for producing liquid fuels from solid biomass. Obtaining liquid fuels (especially for transportation) from renewable sources is of increasing interest due to concerns about economics and environmental impact of using depleting fossil fuels. About 97% of transportation fuels are derived from non-renewable petroleum and 63% of the entire oil consumption in the United States is due to transportation [1]. Development of renewable fuels is stimulated by government policies such as Renewable Fuel Standard (RFS2) in the United States. This policy imposes an increase in renewable fuels production to 36 billion gallons by 2022, where 21 billion gallons are required to be obtained from lignocellulosic materials [2]. Fast pyrolysis is one of the possible pathways for converting low quality biomass into liquid fuels or chemicals. Therefore, it could help with both fulfilling RFS2 requirements and utilization of large resources of organic waste such as nut shells, coffee grounds, straw, bagasse, urban and forestry wood waste. The advantages of using pyrolysis liquid as a fuel are as follows: i) CO_2/GHG neutral, ii) low SOx emissions, and iii) low NOx emissions compared with diesel oil. However, thermochemical conversion of biomass resources is challenging due to large variations in feedstock chemical composition, which are reflected in different product yields and composition. Techno-economic analyses (TEAs) are needed for each individual biomass fast pyrolysis system before implementation, in order to estimate the plant efficiency and products cost. These parameters are of crucial importance for investment decision making process [3–5]. Thus it is necessary to develop pyrolysis system models for TEAs, which give reasonable predictions of pyrolysis oil yield and composition from different feedstocks, at different reactor scales and under different operating conditions. These results are used for optimization of plant size and operating conditions for a given biomass feedstock.

Predicting pyrolysis product yields and composition is challenging as pyrolysis reaction mechanism and the effects of biomass feedstock composition on products yield are still not well understood. One of the biggest problems with developing kinetic mechanisms is due to alkali metals present within biomass structure, which are known to have an adverse effect on pyrolysis oil yield from pyrolysis reactors [6]. Detailed qualitative and quantitative information about the effect of inorganic compounds on biomass pyrolysis oil yield, composition and reaction kinetics is not provided in the scarce literature data on this topic. The importance of the inorganic compounds has been acknowledged and there are ongoing efforts aiming at incorporating a correction for this effect in the pyrolysis mechanism. The first biomass pyrolysis reaction mechanism corrected for the alkali was proposed by Anca-Couce et al. [7]. The impact of the inorganic compounds was evaluated for large biomass particles (1cm) and under slow heating rate conditions. It was approximated by introducing secondary cracking reactions described with an empirical coefficient. This scheme however might not be applicable to fast pyrolysis conditions prevailing in CFB reactors where heating rates are very high and particle size usually does not exceed 2 mm.

Most biorefinery system models are not equipped with any reaction mechanism for describing biomass fast pyrolysis. Instead, they are based on yields and use a static snapshot of experimental results [3, 5]. This technique is computationally simple, however, the results cannot be extrapolated to describe systems equipped with other reactor types, operating under different conditions, or supplied with alternative biomass feedstocks. There is a need to improve the reactor models currently used within process simulators by incorporating a description of reaction kinetics coupled with heat transfer and fluid dynamics. Reactor models with varying complexity and focus are currently available in the literature, but do not meet the needs of process simulations. Single particle models provide detailed description of intraparticle heat and mass transfer. They are typically coupled with a simplified kinetic

mechanism [8]. Fluid dynamics and particle interactions in the reactor, which affect particle residence time, are not captured in these models. Existing 1-D pyrolysis reactor models [9, 10] are also coupled with oversimplified reaction mechanisms, which do not provide any information about products speciation. Moreover, fluid dynamics are often described with purely empirical correlations which cannot be extrapolated to represent different reactor geometries [11]. Finally, isothermal conditions are commonly assumed in order to simplify calculations [10]. Since reaction kinetics depend exponentially on the temperature, even small temperature changes might be significant for reaction kinetics.

Computational fluid dynamics (CFD) models provide a detailed description of fluid dynamics and heat transfer inside a reactor, which can be coupled with a complex reaction kinetics mechanism [12]. However, complex CFD models are too computationally expensive for the purpose of evaluating multiple techno-economic scenarios and quickly optimizing operating parameters of large scale reactors. Moreover, they do not always offer improved accuracy of flow prediction [13]. Therefore, there is a need to bridge the gap between simple yield reactor models, single particle models and CFD reactor models by developing a 1-D, steady-state CFD reactor model computationally compatible for integration with a biorefinery process model.

The reactor model proposed in this work offers several advantages over currently existing 1-D fast pyrolysis reactor models in that it: i) provides information about products speciation, ii) is coupled with a momentum balance in place of empirical correlations, and iii) is coupled with an energy balance in place of an isothermal assumption. As a result, the reactor model is computationally compatible with a biorefinery system model and still captures much of the chemistry and physics affecting product composition. The advantage over multi-dimensional CFD models is a significantly lower computational cost which allows for employing a complex kinetic mechanism, thus giving more detailed information about

product yields and composition. A steady-state model is assumed to be a reasonable approximation of a pyrolysis reactor for the purposes of techno-economic analyses because a continuous operation is desired.

The main goal of this work is to develop a framework which could be used in the future in order to provide guidelines for adjusting and optimizing operating parameters of the circulating fluidized bed reactors for fast pyrolysis application. Moreover, it is desired to evaluate the effect of fluidization parameters (gas mass flowrate, inert solids mass flow rate, particle size), heat transfer and biomass composition (contaminants) on the fast pyrolysis product yields and composition. As previously mentioned, the currently used reactor models are yield reactors with limited predictive capabilities. Therefore, this work is focused on improving process simulations by identifying and incorporating the most influential parameters into the biomass fast pyrolysis reactor model. This will result in improved predictions of product yields and composition, which are critical for evaluating the economics of fast pyrolysis projects. The detailed research questions with respect to a fast pyrolysis reactor addressed in this work are the following:

1. Is a 1-D reactor model an acceptable engineering approximation?
    - How do the 1-D model prediction, 2-D model prediction and experimental results compare?
    - What are the sources of the differences between the results and what are the possible errors of each method?
2. How do the operating parameters (temperature, residence time, olivine mass flux, olivine temperature, particle size) affect pyrolysis products yield and composition?
    - Which parameters are the most important?

- What are the differences in operating strategy for different biomass feedstocks (if any)?

3. How do the alkali metals affect pyrolysis process, product yields and composition?

   - Is potassium a reasonable approximation of alkali metals?
   - Which product classes are the most affected?
   - How do the product yields change with increasing amount of alkali?
   - Is modification of cellulose kinetics sufficient to approximate the effect of alkali or should other biomass building blocks be considered?
   - What are the errors and uncertainties related to the proposed experimental procedure?

Beyond these very specific research questions, the additional research outcomes are the following:

1. Understanding of the principles of a solid - gas flow and heat transfer inside riser reactors.

2. Understanding of the limitations resulting from simplifying assumptions applied in 1-D and 2-D mathematical description of solids - gas flow and heat transfer.

3. Understanding of the difficulties related to describing biomass pyrolysis reactions resulting from complex and highly heterogeneous and anisotropic biomass structure and chemical composition.

The thesis is comprised of nine chapters. Chapter 1 introduces the readers to the topic of the thesis, gives the context for the research and lists the objectives of this work based on identified needs. Chapter 2 of this work gives an overview of fast pyrolysis characteristics, CFB reactor design and operating principles and biorefinery process flow diagram. Chapter

3 provides a literature review of modeling CFB reactors for biomass fast pyrolysis, inclusive of the fast pyrolysis reaction models, biomass particle models, solid - gas flow models, heat transfer models and experimental efforts focused on describing and understanding of the catalytic effect of inorganic compounds on biomass pyrolysis process. The CFB model assumptions and governing equations are presented in Chapter 4. Chapter 5 presents the simulation results from the 1D non-reactive riser model and comprehensive model verification with multiple sources in order to justify the proposed modeling methodology for the reactor. The fluid dynamic and heat transfer results are compared to the results from a transient, one-dimensional and two-dimensional CFD model developed in MFIX. The convective heat transfer coefficient to biomass particle is verifieded by comparison to the results from a three-dimensional particle model developed based on particle imaging. Due to the high computational cost of both the single particle model and the CFD riser model, chemical reactions were not included in simulations. Both riser models were validated with cold flow publicly available experimental data from a cold flow riser at the National Energy Technology Laboratory (NETL) as described in chapter 6. Chapter 7 presents the biomass fast pyrolysis simulation results obtained with the developed 1-D reactor model inclusive of the evaluation of the effect of chosen operating parameters such as particle size, sand-to-biomass ratio, biomass composition, and fluidizing gas composition on the fluid dynamics, heat transfer and pyrolysis product yields and composition. Chapter 8 describes the experimental approach and data analysis methods employed in order to develop a methodology for mathematically describing the effect of inorganic compounds on cellulose pyrolysis kinetics. The findings and identified challenges related to the proposed experimental methodology, mathematical processing of the collected data and interpretation of the results are presented. Chapter 9 lists the conclusions from the performed analysis, summarizes the advantages and disadvantages of the developed model and proposed methodology and points out the identified attractive directions for further research regarding the development of a CFB reactor model for biomass fast pyrolysis.

CHAPTER 2
OVERVIEW OF BIOMASS FAST PYROLYSIS

This chapter provides general information about the fast pyrolysis process characteristics, reactor types and fast pyrolysis plant components. The chapter first provides the basic definitions regarding pyrolysis process parameters, product yield and properties of the pyrolysis liquid. Next, a short summary of historic development of fast pyrolysis reactors is presented. The advantages and disadvantages of different reactor designs for fast pyrolysis applications are reviewed. Finally, the process flow diagram of a typical biomass fast pyrolysis plant equipped with a CFB reactor is described in details.

2.1 General Characteristics

Biomass fast pyrolysis is defined as rapid thermal decomposition in the absence of oxygen to produce non-condensable gases, char, and vapors. The goal of fast pyrolysis is to maximize the liquid yield. Relative product yields are dependent on operating conditions and biomass feedstock, and typically range between 60-75 wt% pyrolysis condensate, 15-25 wt% char and 10-20 wt% non-condensable gases [1, 3]. Fast pyrolysis, conventional pyrolysis, and slow pyrolysis (carbonisation) differ in the operating conditions and product yields. Carbonisation is performed at lower temperatures (400^oC) with very low heating rates and long residence times (in the order of days) [1]. The main product from carbonisation process is char. Conventional pyrolysis is typically performed at intermediate temperatures (500-600^oC), at residence times between 5-30 minutes and with low heating rates. The products from the conventional pyrolysis process are typically uniformly distributed among oil, gas and char (approximately 30-35 %wt). Fast pyrolysis, which is the focus of this study is performed at intermediate temperatures ($400 - 650^oC$), very high heating rates (1000-$10000^oC/s$) and residence times between 0.5-5 sec. Fast pyrolysis condensate is comprised of fragments of decomposed cellulose, hemicellulose and lignin. The chemical composition

and physical properties of pyrolysis liquid vary depending on the feedstock, however, several general characteristics are summarized in Table 2.1. Pyrolysis liquid contains up to 30% water by weight, and has a pH between 2.5-3 due to large amounts of oxygenated compounds. It is miscible with polar solvents but not miscible with petroleum derived fuels. Pyrolysis oil is chemically unstable (due to high oxygen content), which causes increased viscosity, reduced volatility or phase separation over time. The relatively low heating value of pyrolysis condensate is between 16-19 MJ/kg due to both high water and oxygen content. Pyrolysis liquids are comprised of thousands of different compounds, which can be characterized by the following major functional groups: hydroxyaldehydes, hydroxyketons, sugars and dehydrosugars, carboxylic acids and phenolic compounds.

Table 2.1: Pyrolysis liquid composition and physical properties

Bio-oil Properties	
water content (%wt)	15-30
pH	2.5-3
HHV (MJ/kg)	16-19
Bio-oil Composition (%wt)	
C	54 -58
H	5.5-7.0
O	35-40
N	0-0.2

2.2 Biomass Fast Pyrolysis Technologies

The history of biomass pyrolysis for liquid fuels production begins in 1970s. The high oil price was the motivation for considering conversion of biomass into transportation fuels. One of the first pyrolysis plants was built in 1970s in San Diego, USA. The plant was co-processing biomass, waste plastics and rubber at the capacity of 200 tons per day (TPD) to produce Refuse Derived Fuel (RDF). The liquid product was to be used as a substitute for the No. 6 fuel oil. However, the plant was closed due to economic reasons related to the low liquid yield of 40%wt. [14]. The development of biomass pyrolysis technology continued with

the entrained flow pyrolysis reactor developed at Georgia Tech in the 1980s. The reactor was operated at 500^{o}C resulting in liquid yields of 50% of the feedstock mass. The entrained flow reactor operates at a high gas flow rate, which results in high parasitic power and low heat transfer rate due to the lower gas heat capacity compared to solids. In addition, the entrained char particles cause cracking of the produced vapors, thus resulting in a lower oil yield.

Bubbling fluidized bed reactors are a much more promising reactor type for fast pyrolysis application as they exhibit good heat transfer characteristics and are a well established technology. Fluidized bed reactors were first employed for the fast pyrolysis process at the University of Waterloo, Canada in 1980s. Bio-oil yields of up to 80% mass of biomass feedstocks were achieved in a 3 kg/h pilot plant. This achievement was followed by the construction of the first demonstration plant with the capacity of 200 kg/day in Union Fenosa, Spain [14]. The Resource Transforms International (RTI) developed a deep bed fluidized reactor concept, which was implemented in a pilot scale plant (10 kg/hr). The advantage of this process was a low gas flow rate, which results in lower power and heat requirements and thus improved process efficiency. Dynamotive Energy Systems built a 100 TPD demonstration plant in West Lorne and a 200-250 TPD plant in Guelph based on this concept. Although both plants exhibited a good technical performance with several days of operation, they were closed due to the economic reasons.

The most promising reactor technology for biomass fast pyrolysis seems to be the circulating fluidized bed reactors, with a few industrial scale reactors successfully operated by Ensyn and VTT. One of the most successful applications is a CFB based plant operated by Red Arrow company, where the produced chemicals are used for food flavoring. Ensyn designed 7 units at the capacity of 100 TPD in North America and announced 7 new installations at 150-400 TPD in Europe, North America, South America and Asia. VTT

currently operates a pilot scale (20 kg/h) fast pyrolysis plant equipped with a CFB reactor. The produced bio-oil can be used as a substitute of the heavy fuel oil or as a substrate for biofuels production.

The most mature and promising chemical reactor types for fast pyrolysis process are summarized in Table 2.2. The reactors can be classified as follows: i) fluidized bed, ii) circulating fluidized bed, iii) ablative, iv) rotating cone, and v) vacuum reactors [14, 15]. The fluidized bed reactors are well established, easy to build and operate. The biggest

Table 2.2: Advantages and disadvantages of most common pyrolysis reactors

Reactor Type	Advantages	Disadvantages	Locations
Fluidized Bed	uniform temperature, proven technology	not scalable, char accumulation	Dynamotive, RTI, Wellman
Circulating Fluidized Bed	short residence time, uniform temperature, scalable	attrition, erosion	EnsyN (Red Arrow, VTT), ENEL, CRES
Ablative	large particles, no carrier gas	high cost, not easily scalable, erosion	Aston University, Fortum
Vacuum	lower temperature, no carrier gas	slow heat transfer, larger equipment required, lower liquid yield	Pyrovac
Rotating cone	no carrier gas requirement	complex system, scale-up difficulties	

advantage of this technology for fast pyrolysis is the high heat transfer which ensures uniform temperature distribution. However, the reactors are not easily scalable, as horizontal temperature gradients might exist in large-scale fluid bed reactors. Moreover, char particles might accumulate on top of the bed and cause cracking of the produced pyrolysis vapors.

Circulating fluidized bed reactors ensure short residence time, fast heat transfer rates and therefore uniform temperature in the reactor. Moreover, they are easily scalable and well suited for large scale applications. However, they require a higher volumetric gas flow

rate. Due to higher velocities, more fine char particles are formed, which are difficult to separate and cause higher char contents in bio-oil.

In an ablative pyrolysis reactor, biomass particles are pressed against hot surfaces. The pyrolysis reactions occur at the contact surface. The advantage of this approach is the high heat transfer at the surface, where the reactions occur. Therefore, the reaction rates are not limited by the low thermal conductivity of biomass. Moreover, there are no restrictions related to biomass particle size and no carrier gas is required, which reduces operating cost. However, due to mechanical complexity, the scale-up feasibility of this technology is questionable.

An auger reactor shares some characteristics with the ablative pyrolysis technology. In this reactor, biomass is transported through a hot tube by two augers. The auger reactor is well suited for small scale applications, as it is compact. Moreover, it does not require fluidizing gas and the particle size is not restricted. However, the presence of moving parts in the hot zone might lead to operational problems and increased maintenance.

Finally, the last reactor type is a vacuum reactor, which typically operates at 450^{o}C and 15 kPa pressure. The heat transfer rates in vacuum pyrolysis are lower compared to other pyrolysis technologies. However, the produced pyrolysis vapors are quickly removed from the reactor, therefore secondary cracking reactions are minimized. Vacuum pyrolysis generally gives lower oil yields compared to other technologies and it requires larger and more complex equipment, which leads to higher capital cost and increased maintenance cost.

2.3 Biomass Fast Pyrolysis Plant Description

Figure 2.1 shows a schematic of a biomass fast pyrolysis plant equipped with a circulating fluidized bed reactor (CFB). The system is comprised of a biomass feeder, a riser reactor, cyclones, a condenser, and a burner. Biomass, inert solids (typically sand) and fluidizing

gas are supplied at the bottom of the circulating fluidized bed (CFB) reactor. Biomass is heated from the carrier gas and sand, and pyrolyzed in the reactor. Since pyrolysis reactions are endothermic, sand is used as a heat source for the process. Pyrolysis gases and vapors are separated from the char and inert solids in a cyclone. Gases and vapors are directed to a condenser, where oil is separated from the gases and collected. Non-condensable gases are partially recycled and used as a carrier gas for the reactor. Char and sand are conveyed into a combustor. The sand is heated with the heat of combustion and recycled to the riser reactor.

The fast pyrolysis riser reactor is a long tube of a circular cross-section, as shown in Figure

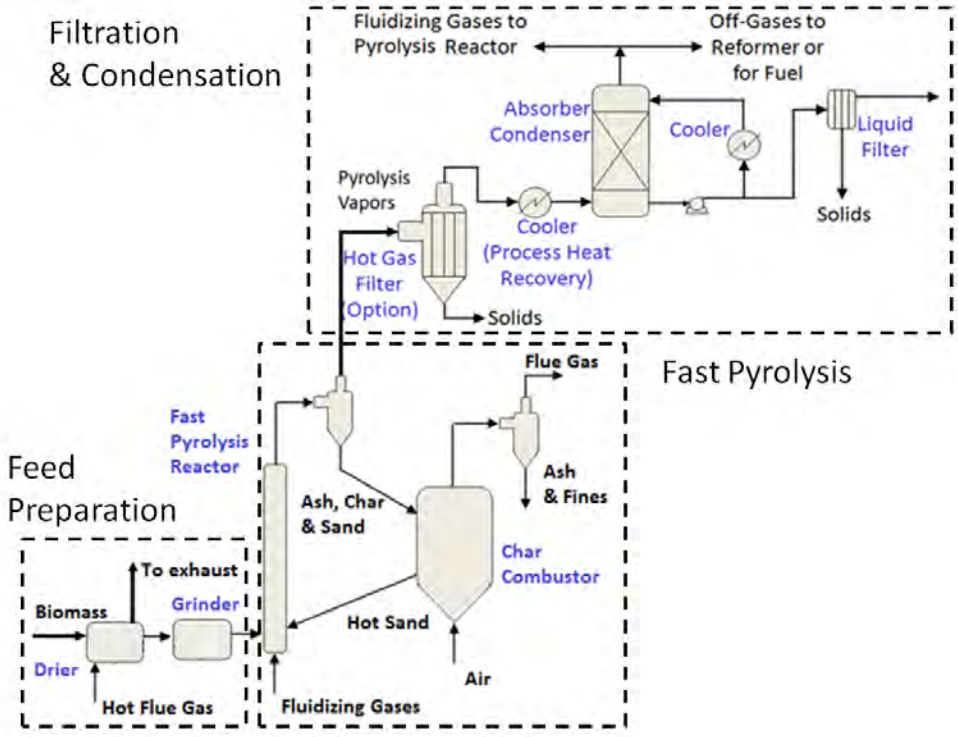

Figure 2.1: Circulating Fluidized Bed Reactor System Schematic.

2.2. Biomass particles are typically ground to particle size of 1-2 mm and dried to approximately 10%wt moisture for industrial applications [3, 4]. Biomass particles enter the reactor after the drying process at approximately 100^{o}C. They are heated to the optimal pyrolysis temperature of approximately 500^{o}C with hot sand recycled from the combustor. The flu-

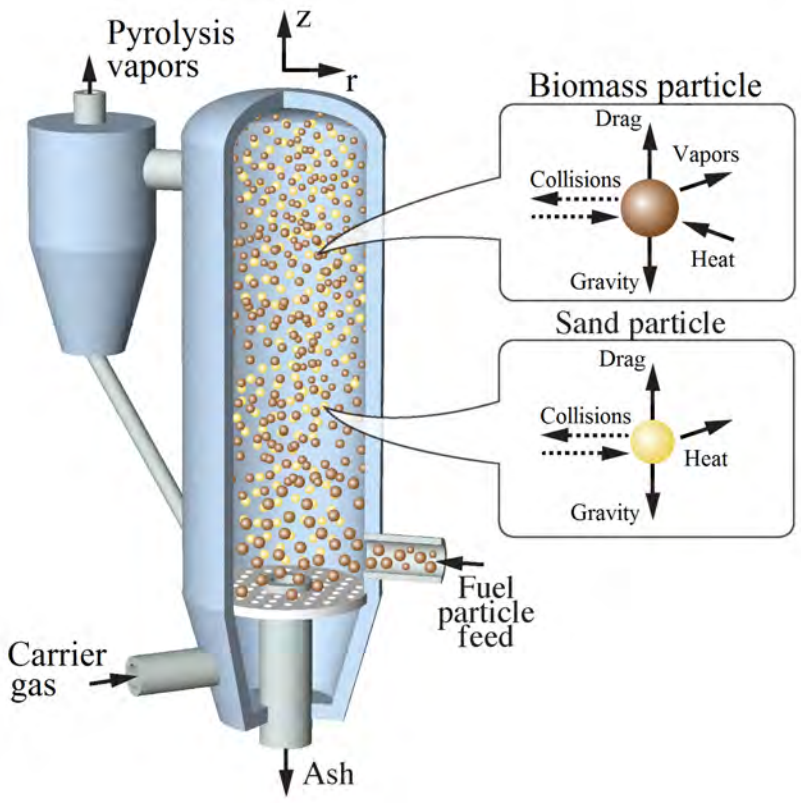

Figure 2.2: Circulating Fluidized Bed Reactor Schematic.

idizing gas is typically recycled pyrolysis gas. It serves as a momentum source, required for transporting solid particles from the bottom to the top of the reactor. The velocity of the fluidizing gas is optimized for a specific average particle size in order to ensure enough drag required to overcome gravity force and to obtain the desired average particle upward velocity at specified solids and gas mass flow rates. Fluidizing gas is typically preheated with the exhaust gases from the combustor before entering the pyrolysis reactor. The temperature and mass flow rate of both sand and fluidizing gas are dependent parameters optimized for an individual application. Intense momentum and heat transfer occur at the reactor inlet. Biomass and sand particles are accelerated in the upward direction by high velocity fluidizing gas. This is accompanied by a simultaneous rapid, convective heat transfer from sand to fluidizing gas and from fluidizing gas to biomass particles. As a result, biomass particles are heated and the pyrolysis reactions occur. Biomass pyrolysis reactions go to completion

within 1-2 s at 500^{o}C [3]. Within a few seconds pyrolysis products, sand particles and fluidizing gas reach the reactor outlet. The provided description is only a simplified, high level picture of the pyrolysis process inside a riser reactor. The solid - gas flow in a CFB reactor is very complex due to particle collisions and clustering. The existence of turbulent particle clusters and their interactions with the reactor walls might lead to local downward particle motion or other deviations from bulk flow characteristics. The detailed description of fluid dynamics of the gas-solids flow is beyond the scope of this study.

CHAPTER 3
LITERATURE REVIEW

This chapter provides a literature review on previous work on modeling biomass fast pyrolysis reactors. The following aspects of reactor modeling are included: biomass conversion chemistry, biomass particle and intraparticle heat and mass transfer phenomena, fluid dynamics of solid - gas flow and heat transfer between the fluidizing gas and solids in CFB reactors.

3.1 Reaction Mechanism

Biomass pyrolysis reaction mechanisms are usually derived from thermogravimetric analysis (TGA) experiments, which allow determination of the rates of product formation [16]. These experiments are performed at much lower heating rates compared with practical fast pyrolysis conditions. However, it is believed that this approach is reasonable because the experiments are free of heat and mass transport limitations. The repeatability of experimental results is often poor even for the same biomass sample batch and the same experimental equipment type [16]. This is because of differences in thermal lag, applied heating rates, and compositional differences within the biomass sample batch. Despite a large number of experimental results reported in the literature, a general conclusion is that a robust and flexible mechanism for biomass pyrolysis is not available due to systematic errors [17, 18]. The published data for activation energy and pre-exponential factors for simple, one component models vary over a wide range and it has been concluded that they are not reliable for quantitative predictions outside of the experimental range that they were derived from [16, 18]. As shown in Figure 3.1 (incorporated from reference [16]) there is no qualitative agreement among different models with respect to product yields as a function of temperature.

Multicomponent models were found to give better product predictions compared with

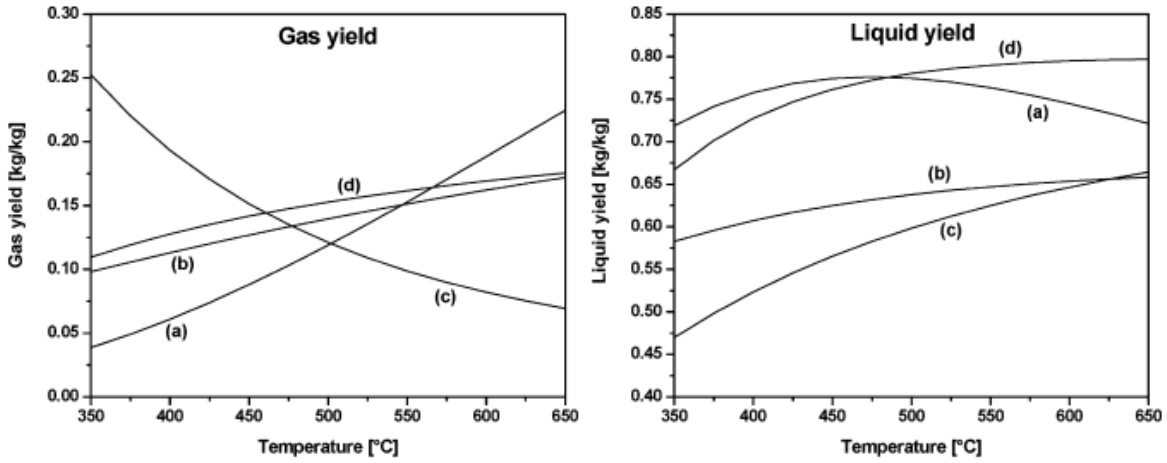

Figure 3.1: Comparison of products predictions from different reaction models presented in the literature [16]

single component models [19]. Therefore, one of the most sophisticated multicomponent model, developed by Ranzi et al. [20], was adopted as a first approximation for the proposed reactor model. The primary reaction mechanism was found to generally give good predictions of product yields for feedstocks with low ash content [21, 22]. However, the model might not be appropriate for biomass heavily contaminated with alkali metals. Moreover, the model does not include the so called "secondary reactions", which are the thermal cracking and repolymerization reactions of the biomass fast pyrolysis product species.

The secondary reactions are known to have a significant contribution at temperatures above 500^oC [23]. However, Hoekstra et al. [24] observed cracking reactions above 400^oC. Experimental results show that secondary reactions lead to formation of mostly CO with other major products being H_2O, CH_4 and H_2 [22]. Ranzi et al. [20] used a general detailed kinetic model of pyrolysis and combustion of hydrocarbons to describe the secondary vapors cracking. This is a very complex mechanism with over 10,000 reactions. A simpler approach is presented by Blondeau and Jeanmart [25], where secondary cracking is described with ten lumped reactions. The mechanism has not been validated up to present. Secondary reactions

include both homogeneous and heterogeneous reactions. The latter might involve inorganic compounds bound to biomass structure or char particles. An established secondary reaction mechanism is currently not available according to the newest review on this topic [18] and further research is highly encouraged.

3.2 Alkali Metals

The major inorganic elements found in biomass are sodium, potassium, magnesium and calcium. The form in which they exist in the biomass structure is uncertain. Over 90% of the alkali metals in biomass structure are found in water soluble or ion exchangeable forms [26]. The weight fraction of ash is commonly used as a quantifier of the weight fraction of alkali metals. Ash content is typically low for woody biomass (<0.5%) and increases for herbaceous species and organic waste (up to 30% ash) [27–29]. The ash content and its chemical composition depend on the environment of individual plants. Therefore the values vary over a wide range even for the same feedstock type [28]. This chemical composition variability and uncertainty about the type of bond formed between inorganic elements and biomass structure is what makes modeling biomass pyrolysis process or extrapolating any experimental results a very difficult task. However, some general qualitative trends describing the effect of alkali on pyrolysis process can be distinguished. Inorganic compounds generally promote gas and char formation and therefore cause a reduced oil yield [27, 30]. Moreover, the composition of pyrolysis oil is altered; the yield of levoglucosan decreases and the yield of glycolaldehyde, formic acid and acetol increase with an increased amount of metal salts [30].

The effect of alkali metals on biomass pyrolysis has been investigated by several researchers [6, 27, 30–33]. Scott et al., [6] first observed that alkali metals cause a reduced oil yield. Varhegyi et al., [30] investigated the effect of magnesium, sodium, iron and zinc on cellulose and biomass pyrolysis. He observed that magnesium did not change the overall weight loss characteristics or the formation of water and carbon dioxide. However, the yields

of minor organic compounds (aldehydes, ketones, etc.) were significantly lower. Sodium was found to increase the yields of char, water, carbon dioxide and carbon monoxide at the expense of the oil yield. Iron and zinc were found to promote water and char formation. Patwardhan et al., [27] found that potassium and sodium had a strong effect on cellulose pyrolysis products, leading to a severe reduction of the levoglucosan yield and increased yield of formic acid, glycolaldehyde and acetol. They also found that calcium and magnesium had a much weaker effect on the levoglucosan yield and negligible effect on the yields of formic acid, glycolaldehyde or acetol [27]. Despite these studies the underlying kinetic mechanism causing the observed changes in product yields is still not well understood.

Some researchers have suggested that the catalytic cellulose pyrolysis mechanism might be either acidic or alkaline [34, 35]. According to this theory, acid catalysts promote dehydration reactions, thus causing increased formation of levoglucosenone, various furan derivatives and char. Alkaline catalysts promote fission and disproportiation reactions, causing increased formation of glyoxal, acetaldehyde, carbonyl compounds and char. However, it has been shown that neutral salts also caused reduced levoglucosan yield and increased char yield [36, 37]. Therefore, it was concluded that the catalytic mechanism was ionic and that alkalinity, acidity or neutrality was of secondary importance [32]. Piskorz et al., [38] found that levoglucosan formation and aldehydes formation during cellulose pyrolysis were competing reactions. The temperature had a weak influence on promoting either of the pathways and it has been concluded that metals determined the product composition [33]. It was suggested that metal cations might inhibit levoglucosan formation by capping the free ends of cellulose chain and thus preventing the unzipping reactions from proceeding. Williams and Horne [32] found that the weight loss curves recorded during cellulose pyrolysis in the presence of salts were characterized by several distinct slopes. As a result, several activation energies for different temperature zones were reported, however the kinetic mechanism of cellulose pyrolysis in the presence of alkali was not explained [32]. The findings on the catalytic effect

of alkali metals on the cellulose pyrolysis mechanism are summarized in Table 3.1.

Table 3.1: Summary of the research findings on the catalytic effect of alkali metals on cellulose pyrolysis reaction mechanism

Research Paper	Proposed Catalytic Effect on Reaction Mechanism
Madorsky et al., 1958 [36]	neutral salts suppress levoglucosan formation and promote char formation
Shafizadeh, 1968 [34], Antal, 1985 [35]	acid catalysts promote the formation of glucosenone, furan derivatives and char; alkaline catalysts promote the formation of glyoxal, acetaldehyde, low molecular weight carbonyl compounds and char
Fung et al., 1972 [37]	acid, alkaline and neutral salts inhibit the formation of levoglucosan
Evans et al., 1987 [39]	alkali metals inhibit the formation of levoglucosan by disrupting the transglycosylation, they promote the formation of carbonyl groups, double bonds and substituted furans
Piskorz et al., 1989 [38]	alkali metals suppress levoglucosan formation by capping the free ends of cellulose chains and inhibiting the unzipping reaction; they promote the formation of glycolaldehyde via the alternative pathway
Williams and Horne, 1994 [32]	the catalytic effect of alkali metals is likely through ionic catalysis with a negligible impact of the acidity, alkalinity or neutrality of the salts
Patwardhan et al., 2010 [40]	inorganic salts/ash promote the formation of formic acid, glycolaldehyde and acetol; they suppress the competing reaction leading to levoglucosan formation

Despite the lack of an established mechanism, the general observations are that inorganic compounds promote water and char formation and therefore, cause a reduced oil yield [27, 30]. Moreover, the composition of pyrolysis oil is altered; the yield of levoglucosan decreases and the yield of glycolaldehyde, formic acid and acetol increase with an increased amount of salts [30]. However, it is not clear whether the observed changes in pyrolysis products are due to alterations in primary reaction pathways, promotion of secondary cracking reactions or a combination of both.

The changes in cellulose pyrolysis product yields as a function of the amount of different alkali metals are illustrated in Figure 3.2 (incorporated from reference [27]).

The effect of alkali metals on the pyrolysis of hemicellulose and lignin are largely un-

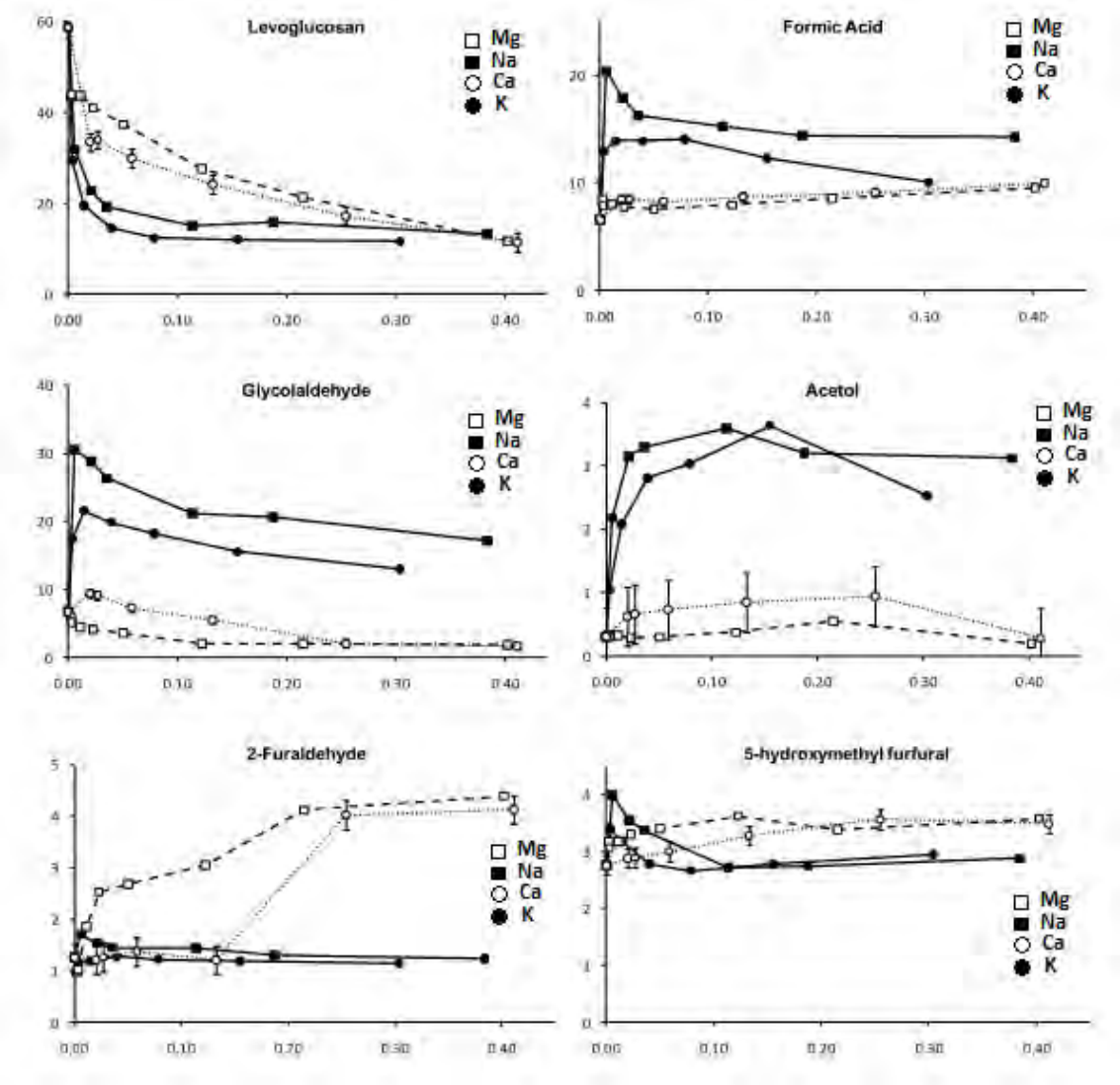

Figure 3.2: Effect of alkali metals on the cellulose pyrolysis products. X axis, mmoles of inorganic metal chloride/g of cellulose; Y axis, % wt of the compound formed [27]

known. Commercially available hemicellulose contains significant amounts of alkali metals which are difficult to remove [27]. The study by Patwardhan [27] comparing product distribution from pyrolysis from purified hemicellulose (0.9 %wt ash) and hemicellulose treated with different metal salts concluded that increased amount of alkali metals promoted pro-

duction of non-condensable gases, light oxygenates and char accompanied by a decreased yield in sugar dehydration products. The results were therefore similar to the trends observed for cellulose. However, it is important to note that a complete removal of alkali was never achieved in this study. Lignin pyrolysis was not significantly affected by the presence of alkali metals according to Patwardhan [27].

The effect of potassium and calcium ions on pyrolysis of wood at low temperatures were studied by Pan and Richards [31]. The study compared pyrolysis products from native wood, purified wood and purified wood treated with potassium and calcium by ion exchange. It was found that potassium treated wood behaved similarly to native wood and calcium treatment did not result in significant changes of pyrolysis process. Therefore it was concluded that potassium had a dominant catalytic effect on pyrolysis process. The mechanism of catalytic reaction remains unknown.

3.3 Biomass Particle

The goal of biomass particle models is to describe coupled effects of heat transfer, mass transfer and anisotropic biomass properties on pyrolysis reactions. After entering a CFB pyrolysis reactor biomass particles are subjected to heat transfer from the surrounding gas and particle-to-particle interactions. As large biomass particles (Bi >0.2) are being heated, temperature gradients form inside the particle due to relatively low thermal conductivity. Therefore, drying and pyrolysis occur first near to particle surface and proceed toward the inside of the particle as the thermal wave propagates. The vapors leave the particle through the pores [41].

The most comprehensive particle models incorporate chemical kinetics, water evaporation, particle shrinkage, heat transfer (conduction, convection, radiation) and convective mass transfer inside the particle [17, 19, 42, 43]. The simulation results performed by Di Blasi [42] show that there are large temperature gradients between the reactor temperature

and particle temperature at particle sizes of approximately 2 mm during particle heating process. However, the pyrolysis reactions occur at a nearly constant temperature due to the cooling effect, which prevents the further increase of the particle temperature. The simulation results also show that the pyrolysis reactions occur at temperatures lower by 40-90K than the reactor temperature for particles between 0.2-0.5 mm. The model was validated only by comparing the product yield with experimental results. The validation of findings with respect to temperature gradients and actual reaction temperature was done only for biomass particles greater than 20 mm because determining the temperature distribution inside smaller biomass particles during fast pyrolysis is a difficult task. The validation results were described as acceptable, however, the general validity of engineering particle models was not proven. Moreover, single particle models were found insufficient for reactor design efforts because of their primary focus on intraparticle phenomena instead of capturing the effect of reactor operating conditions on product yields [16]. Therefore, it is reasonable to seek engineering approximations of single particle models for reactor models.

Kersten et al. [16] found that intraparticle heat transfer can be approximated by using an average particle temperature for evaluating reaction rates. They also showed that intraparticle mass transport phenomena do not affect pyrolysis oil yields for particle sizes between 0.4 mm and 2.4 mm. Janse et al. [44] also showed that the intraparticle transport phenomena do not affect the oil yields under the conditions typical for fluidized bed reactors, however the conversion time was dependent on particle size. Although these results were confirmed by several other modeling studies, as reported by Di Blasi [17], they were assessed not to be conclusive due to simplifying assumptions used in the models.

In addition to reaction temperature and intraparticle mass transport, water evaporation, particle shrinkage and biomass physical properties need to be approximated in the reactor model. Water evaporation could be represented with an Arrhenius type of expression, as it

has been found that water is chemically adsorbed on a biomass surface below the saturation point of 30%wt of dry biomass [41]. There is no consistency in the literature with respect to describing particle shrinkage. Bryden and Hagge [43] assume shrinkage to be a parameter due to uncertainty about its actual value, while Haseli et al. [45] entirely neglect shrinkage. Moreover, Thunman and Leckner [46] found that biomass structure and physical properties are anisotropic, heterogeneous and temperature dependent. Reactor models typically adopt effective properties obtained by applying various averaging techniques [46, 47].

3.4 Fluid Dynamics

Engineering models are usually based on a very simplified fluid dynamics description [17]. Some are simply single particle models, where the reactor is represented by a changing boundary condition, as done by Hastaoglu and Hassam [8]. A slightly more advanced approach to describing hydrodynamics of CFB reactors is to use empirical correlations. The fluidization regime, drag coefficient and pressure drop are described with dimensionless particle diameter and dimensionless velocity. The dimensionless diameter is expressed with the Archimedes number and the dimensionless velocity is expressed with the Reynolds and Archimedes numbers [11]. Although computationally simple, this approach is not reliable or flexible beyond specific conditions for which the correlations were developed.

A more detailed description of solid-gas flow can be obtained by solving Navier-Stokes and Newtonian equations. However, the huge number of particles (typically $> 10^6$) necessitates averaging the equations to reduce computational cost. Typically an Eulerian-Eulerian two phase model is used [48]. It is computationally less demanding compared to Eulerian-Lagrangian models or direct numerical simulations (DNS). This is because an Eulerian-Eulerian model assumes that both the gas and the solids are continuous. The solid - gas interactions are described with the drag models and averaged collision models. Detailed flow models are solved with CFD software packages such as Fluent, CFX, MFIX or others.

The cold flow investigations of CFB reactors hydrodynamics show that the flow is turbulent and unsteady with transient particle clusters and high speed jets forming inside the reactor [49]. The presence of these flow instabilities poses a challenge to using experimental data for determining coefficients and correlations describing the drag or particle collisions. It also poses challenges for experimental measurements of the heat transfer coefficient and developing empirical correlations describing it. Nevertheless, advanced 2-D CFD models can be useful in describing and understanding the physics of gas-solid flows inside CFB reactors, such as the one used for verification of the 1-D model proposed in this work. Since both models include some simplifying assumptions, it is necessary to validate simulation results with cold flow experimental data.

3.5 Heat Transfer

In CFB reactors heat is transferred between gas-solid, solid-solid, solid-wall, gas-wall. All three heat transfer modes (conduction, convection and radiation) coexist. The relative importance of individual heat transfer modes is dependent on the operating conditions and the size of an individual reactor. The contribution of radiation to overall heat transfer was found to be approximately 1% in fast pyrolysis CFB reactors [50]; convection and conduction are the dominate heat transfer modes due to relatively low solids volume fraction in CFB reactors and relatively low temperatures required for fast pyrolysis ($\approx 500^o$C) [1, 50].

There are numerous empirical correlations for evaluating the heat transfer coefficients between the solid-gas phases in fluidized bed reactors. These correlations are typically functions of the Reynolds and Prandtl dimensionless numbers in order to generalize their applicability to a range of fluid conditions and system parameters. In some cases, using the heat transfer coefficient for a single spherical particle is a reasonable approximation [11]. However, there also exist correlations for an average heat transfer coefficient for the entire solid phase. Yang [51] shows that the correlations are able to practically predict the heat transfer coefficient within $\pm 25\%$. The vast majority of existing correlations are determined based on

experiments performed with nearly spherical particles. Biomass particle geometry is known to be very irregular and challenging to describe. Therefore there is some uncertainty about the correlations for the external heat transfer coefficient. This problem was investigated by Ciesielski et al. [52] who developed a sophisticated 3-D microstructure particle model based on multimodal microscopy and quantitative image analysis. The collected data on Feret diameters, aspect ratios and projected areas for over 60,000 particles were subjected to statistical analysis. Next, the constructive solid geometry (CSG) algorithm was used to generate the particle geometry. The simulation results and comparison of the volume averaged particle temperature of the developed particle model with Feret diameter of 2 mm and a spherical particle model of the same heat capacity show that particle geometry and microstructure have a relatively small effect on heat transfer.

The challenges related to determining the actual biomass particle temperature and heat transfer rates are summarized by Jaque Lede [18] in his newest critical review on the research challenges regarding biomass fast pyrolysis reactors. He points out that measuring the temperatures of very fine biomass particles rapidly moving through the reactor in the presence of very fast endothermic reactions with a thermocouple is nearly impossible. For this reason the heating rates and temperatures are evaluated by solving mathematical models, which are built on simplifying assumptions regarding biomass particle geometry, intraparticle heat and mass transfer and physical constants. Therefore, he concludes that the results are highly uncertain. Lede and Authier [53] expand on the topic of reaction temperature and heating rates in their newest study. By solving a simple particle model under different operating conditions, they show that pyrolysis reactions typically occur at temperatures between 620K and 780 K regardless of the heat source temperature or heating rates. They conclude that the biomass temperature during reactions is often significantly lower than the heat source temperature or measured reactor temperature, which might lead to significant errors in determined kinetic parameters.

There is also uncertainty regarding the heat of pyrolysis reaction. It is often reported that pyrolysis reactions are moderately endothermic. However, the heat of reaction is relatively small compared with the sensible heat required for heating up biomass particles and other heat requirements, thus it is often neglected in engineering applications [54].

3.6 Reactor Models

Although CFB reactors are well established in the industry, very little is known about the characteristics of fluid dynamics and heat transfer in the solid - gas flows inside these vessels due to complex nature of the flow multiphase reactive flows. The computational models describing CFB reactors available in the literature are summarized in Table 3.2.

The most common approach to dealing with the complexity of the problem is to employ empirical correlations [55]. However, the flow is affected by several factors such as particle size, physical properties of solids and gas or operating temperature. Therefore, the correlations are mostly applicable to small scale systems and over a limited range of operating conditions. Mechanistic models are more flexible than purely empirical correlations as the effect of the most influential physical parameters on the flow is included. These models are still oversimplified as the common assumptions are axial symmetry and perfect core-annular flow or plug flow.

The one-dimensional steady-state CFB reactor models were developed by several researchers as described in references [63, 67–75]. The approach to describing the hydrodynamics in the axial direction varies; some researchers assume uniform hydrodynamics [67, 68, 78], while others adopt an exponential decay function or other experimentally determined function to describe axial solids distribution [69–72] or a series of well mixed compartments with different solids concentration [73–75]. All of the 1-D models assume uniformity in the radial direction, which is an oversimplification. Therefore the 1-D models only provide rough esti-

Table 3.2: Summary of the literature information on the CFB reactor models

Reactor Model	Literature	Characteristics
Empirical Correlations	[55]	axial volume profiles predictions, non reactive flows, inflexible
Mechanistic Models	[56–66]	core - annulus models describing the solid and gas volume fractions in risers, models fitted with different empirical factors to describe the mass transfer
1-D models	[9, 10, 63, 67–75]	different approaches to fluid dynamics description (uniform flow, empirical functions, series of well mixed compartments) coupled with simplified reaction mechanisms, which do not provide information about products speciation
Computational Fluid Dynamics (CFD)	[12, 76, 77]	bubbling bed simulations, mostly Eulerian-Eulerian approximation
Single Particle Models	[8, 16, 17, 19, 42, 43]	detailed description of intraparticle heat and mass transfer coupled with simplified pyrolysis reaction mechanism, in some cases inclusive of water evaporation

mates of the reactor operation.

The core-annular flow models, which offer an improvement over 1-D approach, were developed by many researchers as described in references [57–64, 66**? ?**]. The core and the annulus region are assumed to be in plug flow. The annular region is assumed to be either stagnant or plug flow. Some of the models include axial variations in the flow while others do not. The mass transfer between the lean core region and dense annulus region is determined by the inter-region mass transfer coefficients determined by fitting with experimental data.

The most detailed mathematical description of the solids - gas flow is obtained from computational fluid dynamics (CFD) models. These models are based on fundamental equa-

tions for mass, momentum and energy balance. However, even in these models the use of empirical correlations is required to describe the drag force. The CFD modeling efforts regarding biomass fast pyrolysis were focused on bubbling bed simulations as shown in references [12, 76, 77]. The CFD simulations can be performed in one-dimensional, two-dimensional and three-dimensional domains. Increasing the complexity of the model results in an increased computational cost. As a result, 3-D models are often too complex to be used as an engineering tool for reactor sizing or tweaking operating parameters. Therefore, there is a need to evaluate the error of flow description due to the simplifying assumptions and choose a reasonable trade-off between accuracy and computational cost.

CHAPTER 4
MODELING METHODOLOGY

This chapter describes the modeling assumptions regarding biomass pyrolysis reaction mechanism, biomass particle, fluid dynamics and heat transfer in a riser reactor used in the 1-D steady state reactor model. Moreover, model equations together with accompanying empirical correlations are provided.

4.1 Assumptions

The primary reaction mechanism chosen for implementation in this work was developed by Ranzi et al. [20, 22]. It is the most detailed and comprehensive mechanism currently available in the literature. The reaction mechanism schematic is presented in Figure 4.1. Biomass is represented by its three primary constituent building blocks (cellulose, hemicellulose and lignin). This leaves the opportunity to account for variability in biomass composition through changes in fractions of the three constituents. Another advantage of the adopted reaction mechanism is the speciation of products. As illustrated in Figure 4.1, pyrolysis vapors are represented with multiple representative compounds, which provide information about relative yields of different functional groups in bio-oil (acids, aldehydes, alcohols etc.). The mechanism is comprised of both primary reactions and secondary reactions. Only the primary reactions from this mechanism are implemented in the reactor model because the secondary reaction mechanism is too complex. As mentioned in section 3.1, Fagbemi et al. [23] showed that secondary reactions are not significant at temperatures optimal for fast pyrolysis (below 800 K). Finally, the only existing simplified secondary reaction mechanism [25] has not been validated. Therefore a secondary reaction mechanism is not included in the model. However, in order to ensure flexibility of the model at higher temperatures (600-650^oC), it is recommended to include secondary reactions once a simplified mechanism is available. Although higher temperatures result in lower oil yield, they

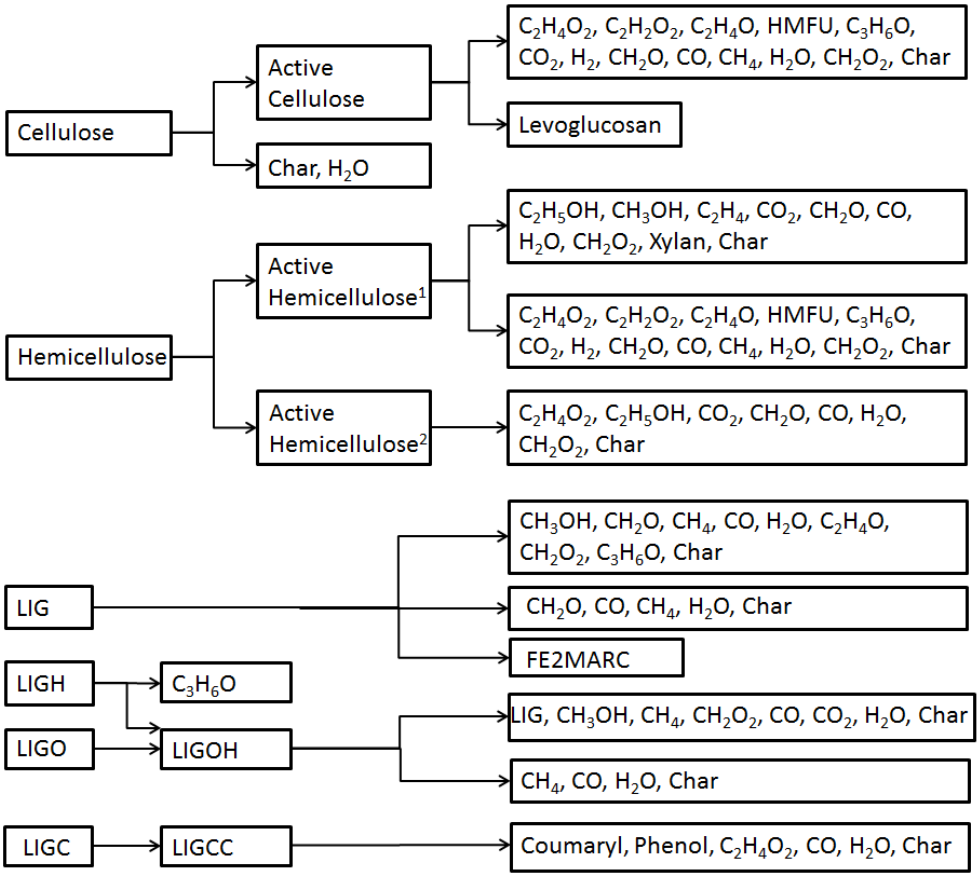

Figure 4.1: Primary biomass pyrolysis reaction mechanism.

might be desirable. As more CO_2 and H_2O are produced in secondary reactions, the oxygen content in the produced oil decreases. Lower oxygen content in the oil is desired and might result in eliminating a hydrotreater, therefore investigating higher pyrolysis temperatures should be included in reactor simulations once a validated reaction mechanism is available.

Physical properties of biomass and char species are taken from Corbetta et al. [22] and are listed in Table 4.1 for completeness. The simulations performed with the 3-D particle model by Ciesielski et al. [52] proved that the particle microstructure which determines the effective properties has a limited impact on heat transfer for relatively small particles (size class <2mm) of the same heat capacity. The properties of the remaining components are determined with Aspen Properties. Particle behavior is modeled based on the following sim-

Table 4.1: Physical Properties of biomass [22] and sand

Property	Biomass	Sand
Density (kg/m^3)	650	2580
Conductivity (W/m-K)	0.2	0.25
Heat capacity (J/kg-K)	703	1600

plifying assumptions: i) particles are identical spheres, ii) physical properties are isotropic, iii) particles behave like a lumped heat capacity (uniform temperature), iv) intraparticle mass transport is not rate limiting, v) particle attrition and shrinkage are neglected. The simplifying assumptions are not realistic, since particle images show that biomass particles are not spherical and the properties are heterogeneous and anisotropic. However, it is important to understand that a single biomass particle size is several orders of magnitude smaller than the reactor length scale. Therefore, providing a detailed description of heat and mass transport phenomena at both the single particle scale and the reactor scale simultaneously is not possible. The proposed 1-D reactor model requires numerous simplifying assumptions regarding biomass and sand particles. These assumptions are justified based on the results from the 3-D microstructure particle model simulations described by Ciesielski et al. [52].

4.2 Governing Equations

The reactor model is comprised of equations representing 1-D, steady-state conservation of species, continuity, momentum, and energy for a solid-gas flow system. The model equations were derived by simplifying the general Euler-Euler solid - gas flow representation. The equations for mass, momentum and energy conservation (and their derivation) can be found in reference [79]. The equations (in their general form) are provided below as a starting point for describing the simplifying assumptions.

Gas phase continuity:

$$\frac{d}{dt}(\epsilon_g \rho_g) + \frac{d}{dz}(\epsilon_g \rho_g v_g) = \sum_{n=1}^{N_g} R_{gn}(z) \tag{4.1}$$

where the first term on the left hand side describes mass accumulation and was neglected in the steady state model, the second term represents convective mass flux and the term on the right hand side describes the mass transfer due to chemical reactions or physical processes (i. e. evaporation) and R_{gn} is the rate of generation of gas-phase species n of the total of N_g gas phase species.

Solid phase continuity:

$$\frac{d}{dt}(\epsilon_m \rho_m) + \frac{d}{dz}(\epsilon_m \rho_m v_m) = \sum_{n=1}^{N_m} R_{mn}(z) \tag{4.2}$$

where the R_{mn} is the generation of solids phase m, species n and N_m is the total number of species in solids phase m. Similarly to the gas phase continuity, the mass accumulation was neglected in the steady state model. Solids density is constant and fluid continuity is supported by the ideal gas law to describe density changes:

$$\rho_g = \frac{P_g \cdot M_w}{R \cdot T_g} \tag{4.3}$$

Momentum equation for gas phase:

$$\frac{d}{dt}(\epsilon_g \rho_g v_g) + \frac{d}{dz}(\epsilon_g \rho_g v_g v_g) = -\epsilon_g \frac{dp}{dz} + \frac{d}{dz}(\tau_{gij}) + \sum_{m=1}^{M} I_{gmi} + f_{gi} + \epsilon_g \rho_g g \tag{4.4}$$

where the first term on the left hand side is the momentum accumulation and was neglected in the steady state model, and the second term is the convective mass flux. On the right sand side, the first term is pressure drop, the second term represents the gas stress with τ_{gij} being the stress tensor, I_{gmi} is the momentum transfer between the gas phase and the m^{th} solids phase, f_{gi} is a general body force and the last term is the body force due to gravity. The gas stress term was neglected in the steady state model as initial simulations showed that it was relatively small compared to other terms. This result was in accordance with the literature [79], as it has been found that the drag force is the most significant term in the momentum equation. The general body force term was also neglected because gravity is the

only significant body force in this problem. Momentum equation for m^{th} solids phase:

$$\frac{d}{dt}(\epsilon_m \rho_m v_m) + \frac{d}{dz}(\epsilon_m \rho_m v_m v_m) = -\epsilon_m \frac{dp}{dz} + \frac{d}{dz}(\tau_{mij}) + \sum_{l=0}^{M} I_{mli} + \epsilon_m \rho_m g \tag{4.5}$$

where the first term on the left hand side is the momentum accumulation and was neglected in the steady state model, and the second term is the convective mass flux. On the right sand side, the first term is pressure drop, the second term represents the solid stress with τ_{mij} being the stress tensor, I_{mli} is the momentum transfer between the m^{th} and l^{th} solid phase (l=0 is the gas phase), and the last term is the body force due to gravity. The solid stress term was neglected in the steady state model due to it's relatively small significance compared to other terms.

Momentum transfer between the gas and solid phase occurs by different mechanisms such as: drag force, buyoancy, virtual mass effect, Saffman lift force, Magnus force, Basset force and Faxen force. The detailed discussion of the individual forces is provided in reference [79]. It is concluded that the drag force is the most significant term in the gas - solid momentum transfer term. Therefore, only the drag force is included in the steady-state model for simplicity. The multiparticle drag coefficient is expressed with the following general equation:

$$I_{gm} = \frac{3}{4} \frac{C_{Dm} \epsilon_g \epsilon_m \rho_g}{d_m} |U_g - U_m| \tag{4.6}$$

The drag coefficient C_{Dm} for the m^{th} solid phase can be determined from different empirical drag models. The Syamlal - O Brien model was chosen for this study. The detailed drag model equations will be provided later in this chapter together with the simplified model equations.

The solids - solids momentum transfer between the m^{th} and l^{th} solid phase is expressed as follows:

$$I_{ml} = F_{ml} |U_m - U_l| \tag{4.7}$$

The expression for the drag coefficient (F_{ml}) was derived from simplified version of kinetic theory [79]. The expression was adopted in the steady state model. The hindrance effect caused by particles in enduring contact expressed with an empirical hindrance coefficient (s_{coef}) was neglected due to the lack of experimental data. The gas phase and solid phase stress tensors were neglected in the steady state model. Conservation of species for the gas phase species n:

$$\frac{d}{dt}(\epsilon_g \rho_g X_{gn}) + \frac{d}{dz}(\epsilon_g \rho_g v_g X_{gn}) = \frac{d}{dz}(D_{gn}\frac{d(X_{gn})}{dz}) + R_{gn} \tag{4.8}$$

where X_{gn} is the mass fraction and R_{gn} is the rate of formation of gas species n. Conservation of species for the solid phase m species n:

$$\frac{d}{dt}(\epsilon_m \rho_m X_{mn}) + \frac{d}{dz}(\epsilon_m \rho_m v_m X_{mn}) = \frac{d}{dz}(D_{mn}\frac{d(X_{gn})}{dz}) + R_{mn} \tag{4.9}$$

where X_{mn} is the mass fraction and R_{mn} is the rate of formation of solids phase m species n. The species accumulation and species diffusion terms were neglected in the steady - state model. Axial diffusion terms are negligible in CFB reactor applications due to high gas velocities resulting in convection being the dominant transport mode. The mass transport limitations expressed with the Sherwood number were neglected in the model at this initial stage. This is because inclusion of the intraparticle mass transfer effect carries large uncertainty regarding the diffusion coefficients, empirical correlations for the Sherwood number and assumptions regarding the particle model. Moreover, the available literature information on the single particle modeling indicates that the intraparticle heat and mass transfer do not affect the product yields for particles smaller than 2 mm. Therefore a detailed investigation of the mass transfer phenomena is outside of the scope of this study because it would introduce additional complexity to the model without necessarily improving the model results. Without proper validation (which is not possible at present), the results could be misleading due to incorporated simplifying assumptions and uncertainly about the biomass transport properties. However, it is recommended to investigate the effects of mass transfer in the future, evaluate the ucertainty, validate the results and incorporate mass transfer limitations

into the model, if necessary. The conservation of internal energy for the fluid phase:

$$\epsilon_g \rho_g c_{p,g} [\frac{d(T_g)}{dt} + \frac{v_g d(T_g)}{dz}] = -\frac{d(q_g)}{dz} + \sum_{m=1}^{M} \gamma_{gm}(T_m - T_g) + \gamma_{Rg}(T_{Rg}^4 - T_g^4) - \epsilon_g(\frac{d(p_g)}{dt} + v_g \frac{d(p_g)}{dz}) - \Delta H_g \tag{4.10}$$

where the first term on the left hand side is energy accumulation (neglected in the steady-state model) and the second term is the convective term. The first term on the right hand side is the fluid phase axial conduction, the second term is the solid - fluid interfacial heat transfer, the third term is the radiative heat transfer, the fourth term is the interfacial work term and the last term is the heat of reaction. The conservation of internal energy for the m^{th} solid phase:

$$\epsilon_m \rho_m c_{p,m} [\frac{d(T_m)}{dt} + \frac{v_m d(T_m)}{dz}] = -\frac{d(q_m)}{dz} + \gamma_{gm}(T_m - T_g) + \gamma_{Rm}(T_{Rm}^4 - T_m^4) - \Delta H_m \tag{4.11}$$

where the first term on the left hand side is energy accumulation (neglected in the steady-state model) and the second term is the convective term. The first term on the right hand side is the solid phase axial conduction, the second term is the solid - fluid interfacial heat transfer, the third term is the radiative heat transfer, and the last term is the heat of reaction. These equations were derived based on two simplifying assumptions as described in reference [79]. Firstly, heat transfer due to viscous dissipation and interfacial momentum transfer were neglected, as they are only significant when the relative velocities between gas and solids are large. Secondly, the direct heat transfer between different solids was neglected. In addition to these assumptions, the energy accumulation terms were neglected in the steady state model. The axial heat conduction in the gas and solid phase was also neglected as diffusive terms are negligible in CFB reactor applications. The radiation terms were neglected for simplicity. This choice is justified based on the literature, as it has been found that radiation accounts for approximately 1% of heat transfer in CFB reactors. This assumption is verified by comparing the model results with the CFD simulation results, where the radiative heat transfer was included. Finally, the interfacial work term is neglected. The solid - gas interfacial heat

transfer coefficient is expressed with empirical correlations provided later in the chapter together with simplified energy equations. Based on the aforementioned simplifications of the Euler- Euler solid - gas flow descriptions the following model equations were derived: The conservation of species n in m^{th} solid phase is represented by:

$$\frac{d}{dz}(\epsilon_m \rho_m v_m X_{mn}) = R_{mn}(z) \tag{4.12}$$

where R_{mn} is the rate of formation of species n in m^{th} solid phase. There are two solid phases: biomass and sand, where biomass is comprised of 13 species (produced char is included in biomass phase). Biomass density constant and equal for all the species. There are 19 primary pyrolysis reactions $N_{rxn} = 19$ and an additional water evaporation reaction, given by the general Arhennius formula:

$$R_j(z) = k \cdot e^{-\frac{Ea}{R \cdot T}} \cdot M_{mn} \tag{4.13}$$

where R_j is the rate of reaction j and M is the mass of species n in solid phase m reacting in reaction j. There are no gas phase reactions included in the model. The conservation of species n in gas phase (g):

$$\frac{d}{dz}(\epsilon_g \rho_g v_g X_{gn}) = R_{gn} \tag{4.14}$$

where R_{gn} is the rate of formation of species n in gas phase. The gaseous species are formed only in the solid phase phase reactions, therefore the rate is based on the mass of biomass species and the stoichiometric coefficients are used to determine the rate of gas formation. All reactions follow an Arrhenius form. Moreover, the reactions are first order, as commonly reported in the literature [19, 20]. The details of the employed reaction mechanism (activation energies, pre-exponents and stoichiometry) are provided in Appendix A. The continuity equation for the gas phase is represented by:

$$\frac{d}{dz}(\epsilon_g \rho_g v_g) = \sum_{n=1}^{N_g} R_{gn}(z) \tag{4.15}$$

where ϵ_g, ρ_g, v_g are the volume fraction, density ($kg \cdot m^{-3}$) and velocity ($m \cdot s^{-1}$) of gas mixture. The continuity equation for the biomass phase is represented by:

$$\frac{d}{dz}(\epsilon_b \rho_b v_b) = \sum_{n=1}^{N_b} R_{bn}(z) \tag{4.16}$$

where ϵ_b, ρ_b, v_b are the volume fraction, density ($kg \cdot m^{-3}$) and velocity ($m \cdot s^{-1}$) of biomass. The continuity equation for the inert sand is represented by:

$$\frac{d}{dz}(\epsilon_s \rho_s v_s) = 0 \tag{4.17}$$

where ϵ_s, ρ_s, v_s are the volume fraction, density ($kg \cdot m^{-3}$) and velocity ($m \cdot s^{-1}$) of sand. The momentum balance for the biomass phase is represented by:

$$\frac{d}{dz}(\epsilon_b \rho_b v_b v_b) = -\epsilon_b \frac{dp}{dz} + \beta(v_g - v_b) - F_{s-b}|v_s - v_b| - \frac{2 f_b \epsilon_b \rho_b v_b v_b}{D_{reactor}} - \epsilon_b \rho_b g \tag{4.18}$$

where F_{s-b} is the particle collision coefficient, which represents the momentum loss due to particle collisions, β is an interphase momentum exchange coefficient, f_b - is the friction coefficient, and $D_{reactor}$ is the reactor diameter (m). The convective term on the left hand side of the equation is due to the combined impact of the following forces: pressure drop $\epsilon_b \frac{dp}{dz}$, gravity force $\epsilon_b \rho_b g$, momentum exchange between solid and gas phase $\beta(v_g - v_b)$, momentum loss due to collisions with the walls $\frac{2 f_b \epsilon_b \rho_b v_b v_b}{D_{reactor}}$, and momentum loss due to solid-solid interactions $F_{s-b}|v_s - v_b|$. The empirical coefficients in the momentum equation can be calculated from empirical correlations [80]. Particle collision coefficient can be calculated from:

$$F_{s-b} = 3(1 + e_{s-b})(\frac{\pi}{2} + c_{f,s-b}\frac{\pi^2}{8})\frac{(d_{p,s} + d_{p,b})^2}{2\pi(\rho_s d_{p,s}^3 + \rho_b d_{p,b}^3)}\rho_s \rho_b g_{0,s-b}|v_s - v_b| \tag{4.19}$$

where:

$$g_{0,s-b} = \frac{1}{\epsilon_g} + \frac{3 d_{p,s} d_{p,b}}{\epsilon_g^2 (d_{p,s} + d_{p,b})}(\frac{\epsilon_s}{d_{p,s}} + \frac{\epsilon_b}{d_{b,s}}) \tag{4.20}$$

where e_{s-b} is the coefficient of restitution equal to 0.9, $c_{f,s-b}$ is the particle friction coefficient equal to 0.0001, and $g_{0,s-b}$ is the radial distribution function at contact. Interphase

momentum exchange coefficient can be calculated from [80]:

$$\beta = \frac{3\epsilon_{s-b}\epsilon_g\rho_g}{4V_{r,s-b}^2 d_{p,s-b}} C_D(\frac{Re_{s-b}}{V_{r,s-b}})|v_s - v_b| \tag{4.21}$$

where $V_{r,s-b}$ is the terminal velocity of the solids, and C_D is the empirical drag coefficient, which can be calculated from the following correlations:

$$V_{r,s-b} = 0.5(\epsilon_g^{4.14} - 0.06Re_{s,b} + \sqrt{(0.06Re_{s-b})^2 + 0.12Re_{s-b}(2B - \epsilon_g^{4.14}) + \epsilon_g^{8.28}}) \tag{4.22}$$

where

$$B = 0.8\epsilon_g^{1.28} \;\; if \;\; \epsilon_g \leq 0.85 \qquad\qquad B = \epsilon_g^{2.65} \;\; if \;\; \epsilon_g > 0.85 \tag{4.23}$$

$$C_D(\frac{Re_{s-b}}{V_{r,s-b}}) = (0.63 + \frac{4.8}{\sqrt{\frac{Re_{s-b}}{V_{r,s-b}}}})^2 \tag{4.24}$$

where Re_{s-b} is the Reynolds number expressed with:

$$Re_{s-b} = \frac{|v_g - v_{s-b}|d_{s-b}\rho_g\epsilon_g}{\mu_g} \tag{4.25}$$

Friction coefficients for the gas and solid phase can be calculated from [81] as follows:

$$f_g = \frac{16}{Re} \qquad if \;\; Re \leq 2,100 \tag{4.26}$$

$$f_g = \frac{0.0791}{Re^{\frac{1}{4}}} \qquad if \;\; 2,100 \leq Re \leq 10^5 \tag{4.27}$$

$$f_g = [2log(Re\sqrt{f_g} - 0.8]^{-2} \qquad if \;\; Re > 10^5 \tag{4.28}$$

where Re is the Reynolds number for the gas phase given by:

$$Re = \frac{\epsilon_g|v_g|D_h\rho_g}{\mu_g} \tag{4.29}$$

$$f_s = \frac{0.0025}{v_p} \tag{4.30}$$

Similarly the momentum balance for sand is represented by:

$$\frac{d}{dz}(\epsilon_s\rho_s v_s v_s) = -\epsilon_s\frac{dp}{dz} + \beta(v_g - v_s) - F_{s-b}|v_s - v_b| - \frac{2f_s\epsilon_s\rho_s v_s v_s}{D_{reactor}} - \epsilon_s\rho_s g \tag{4.31}$$

The momentum balance for the gas phase is calculated as follows:

$$\frac{d}{dz}(\epsilon_g \rho_g v_g v_g) = -\epsilon_g \frac{dp}{dz} + \beta(v_g - v_s) + \beta(v_g - v_b) - \frac{2 f_g \epsilon_g \rho_g v_g v_g}{D_{reactor}} - \epsilon_g \rho_g g \tag{4.32}$$

The energy balance for biomass phase is calculated as follows:

$$\rho_b c_{p,b} \frac{d(\epsilon_b v_b T_b)}{dz} = -h_{bg}(T_b - T_g) + \sum_{n=1}^{N_{rxn}} R_j \Delta H_j \tag{4.33}$$

where $c_{p,b}$ is the specific heat of biomass ($Jkg^{-}K^{-1}$), T_b, T_g are the average biomass particle temperature (K) and the average gas temperature (K) respectively, h_{bg} is the overall heat transfer coefficient between biomass and gas ($Wm^{-2}K^{-1}$) , and ΔH_j is the enthalpy of reaction for reaction j. The change in biomass temperature along the reactor $\rho_b c_{p,b} \frac{d(\epsilon_b v_b T_b)}{dz}$ is due to heat transfer from the gas phase $h_{bg}(T_b - T_g)$ and heat of pyrolysis reactions $\sum_j R_j \Delta H_j$. Similarly the energy balance for sand is calculated as follows:

$$\rho_s c_{p,s} \frac{d(\epsilon_s v_s T_s)}{dz} = -h_{s,g}(T_s - T_g) \tag{4.34}$$

where $c_{p,s}$ is the specific heat of sand ($Jkg^{-}K^{-1}$), T_s is the average sand particle temperature (K), h_{sg} is the overall heat transfer coefficient between sand and gas ($Wm^{-2}K^{-1}$). The change is sand temperature along the reactor $\rho_s c_{p,s} \frac{d(\epsilon_s v_s T_s)}{dz}$ is due to heat transfer to the gas phase $h_{sg}(T_s - T_g)$. Energy equation for gas phase is calculated from:

$$c_{p,g} \frac{d(\epsilon_g \rho_g v_g T_g)}{dz} = h_{sg}(T_s - T_g) + h_{bg}(T_b - T_g) \tag{4.35}$$

Where $c_{p,s}$ is the specific heat of gas mixture ($Jkg^{-1}K^{-1}$). The change in gas temperature along the reactor $c_{p,g} \frac{d(\epsilon_g \rho_g v_g T_g)}{dz}$ is due to heat transfer from the sand $h_{sg}(T_s - T_g)$ and heat transfer to the biomass $h_{bg}(T_b - T_g)$. The heat transfer coefficient between the solid and gas phase was calculated from the following correlations:

$$h_{sg} = \frac{6 k_g \epsilon_s N u_s}{d_p^2} \tag{4.36}$$

where the particle Nusselt Nu_s number was calculated as follows:

$$Nu_s = (7 - 10\epsilon_g + 5\epsilon_g^2)(1 + 0.7Re_s^{0.2}Pr^{0.33}) + (1.33 - 2.4\epsilon_g + 1.2\epsilon_g^2)Re_s^{0.7}Pr^{0.33} \quad (4.37)$$

where k_g is the thermal conductivity of gas, Pr is the Prandtl number, Re_s is the solids Reynolds number and d_p is particle diameter. Correlations were obtained from MFIX Documentation Theory Guide [80]. Constitutive equations used in order to solve the model were: Ideal gas law:

$$\rho_g = \frac{P_g \cdot MW_g}{R \cdot T_g} \quad (4.38)$$

where the molecular weight of gas mixture is calculated based on the gas composition. Summation of the volume fractions:

$$\sum_{i=1}^{N_{m+g}} \epsilon_i = 1 \quad (4.39)$$

The following parameters were specified at the inlet to solve the model: gas pressure, gas, biomass and sand temperature, biomass mass flow rate and mass fractions of individual species, gas-to-biomass ratio (mass) and gas composition, sand-to-biomass ratio (mass basis) biomass and sand inlet velocity.

4.3 Model Input Parameters

Three well characterized feedstocks were considered for this work: (i) pine, (ii) corn stover, (iii) switchgrass. These feedstocks were chosen so that different biomass categories were represented. The chemical composition information, shown in Table 4.2, was obtained from the data available through collaboration with the Thermochemical Feedstock Interface project at NREL summarized in an internal report. The operating parameters used for the baseline simulations of a small scale reactor ($0.023 kgs^{-1}$) are summarized in Table 4.3. The inlet pressure, inlet sand and biomass velocity assumptions are based on cold flow (non-reactive) information available for a similar size CFB riser described by Sanchez et al. [81]. The inlet gas temperature, biomass temperature, sand temperature, sand-to-biomass ratio

Table 4.2: Chemical composition of biomass feedstocks [82]

Feedstock	Pine	Corn Stover	Switchgrass
Cellulose	0.450	0.380	0.450
Hemicellulose	0.260	0.380	0.27
Lignin	0.263	0.144	0.200
Ash	0.007	0.043	0.042
Water	0.020	0.053	0.038

and gas-to-biomass ratio are assumed based on estimates reported by Ringer et al. [3]. The

Table 4.3: Model input parameters

Biomass	
$M_{biomass}(kgs^{-1})$	0.023
$D_{p,biomass}(m^{-6})$	500
$T_{biomass}(K)$	373
$v_{biomass}(ms^{-1})$	0.15
Sand	
$R_{sand/bio}(-)$	10
$D_{p,sand}(m^{-6})$	500
T_{sand} (K)	900
$v_{sand}(ms^{-1})$	0.15
Gas	
T_{gas} (K)	700
p (bar)	2.3
$R_{gas/bio}(-)$	0.75/0.5
Reactor	
$D_{reactor}$ (m)	0.08
$H_{reactor}$ (m)	4

baseline non-reactive simulation was performed at the gas-to-biomass ratio of 0.75 and the reactive baseline simulation was performed at the gas-to-biomass ratio of 0.5. The gas-to-biomass ratio was lower in the reactive simulations because additional gases and vapors are produced in the reactions. The non-reactive simulations were performed with pine feedstock. In order to evaluate the effect of operating parameters on fluidization conditions inside the riser reactors a parametric sweep was performed for both the non-reactive and reactive simulations. The following parameters were subjected to analysis: particle size, system

pressurization, hydrogen addition to the fluidizing gas, sand-to-biomass ratio, gas-to-biomass ratio, biomass density. The range of parametric sweep is summarized in Table 4.4.

Table 4.4: Range of input parameters subjected to sensitivity analysis

Parameter	Values
$D_{particle}$ (mm)	0.5, 1, 2
P (bar)	2.3 , 8.5
H_2 (%wt)	0.4, 18.9
$R_{sand/bio}(-)$	7.8 , 10, 15
$R_{gas/bio}(-)$	0.5, 0.750 / 0.25, 0.5, 1.0
$\rho_{bio}(kg/m^3)$	325, 650

4.4 Model Discretization

The 1-D, steady-state model was discretized by using the backward finite difference method with a constant step size of 0.05 m for non-reactive simulations. The reactive simulations required a higher resolution near the reactor inlet where the intense heat transfer and reactions occur simultaneously. Therefore, a step size of 0.005m was used for the first 0.5 meters above the reactor inlet in reactive simulations and the remaining part of the domain was discretized with the 0.05m step size. The Newton-Rapson method was used to solve model equations.

CHAPTER 5

MODEL BENCHMARK STUDY OF FLUIDIZATION IN A RISER WITH 1-D AND 2-D SIMULATIONS

A parametric study was performed in order to evaluate the effect of the particle size, temperature, pressure, sand-to-biomass ratio, gas-to-biomass ratio and hydrogen addition to the fluidizing gas on the fluid dynamics of a non-reactive flow in a riser. The simulation results from a 1-D, steady-state model were compared to the simulation results from a 1-D transient model in MFIX and 2-D transient model in MFIX for verification. The implications of the simplifying assumptions used in a 1-D, steady state model on the results were assessed. Moreover, additional simulations were performed with modified correlations for the external heat transfer coefficient derived from detailed, 3-D single biomass particle simulations, in order to evaluate the effect of the external heat transfer on average biomass temperature.

5.1 Base Case

The base-case non-reactive simulation results for the 4 meter tall reactor are illustrated in Figure 5.1. The input parameters for this simulation are summarized in Table 4.3. The results show that thermal equilibrium is reached at 0.4 meters above the reactor inlet at the equilibrium temperature of 794 K. The gas velocity required to maintain the fast fluidization regime is approximately 3.8 m/s. The sand and biomass particles are accelerated at the reactor inlet due to the drag force. The solid and gas volume fractions change accordingly in order to fulfill the continuity equation. The biomass and sand particle velocities stabilize at 0.9 m/s and 0.6 m/s respectively. The total solid volume fraction at the outlet is 4%. After the initial intense momentum exchange, there are no significant changes in the particle and gas velocities along the reactor height. According to the simulation results, both momentum exchange and heat transfer rates are initially very high. Therefore, hydrodynamically and thermally fully developed flow conditions are reached nearly at the reactor inlet.

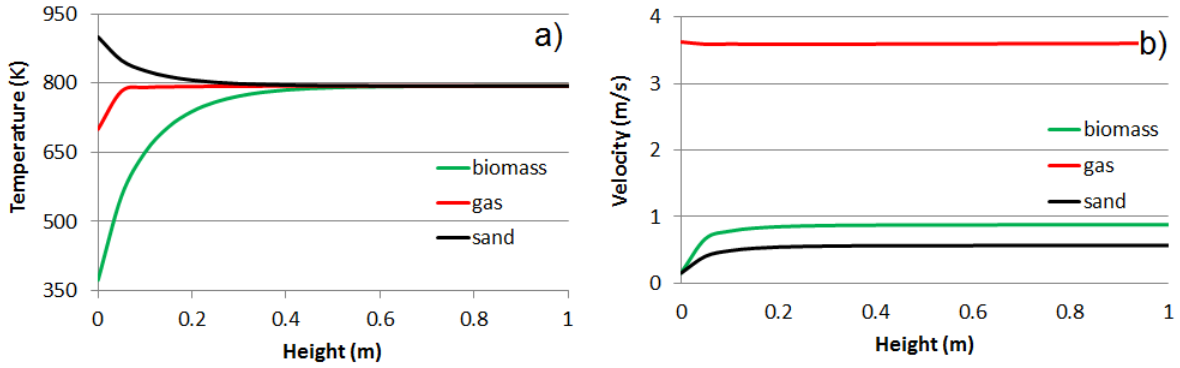

Figure 5.1: Baseline simulation results obtained from the 1D steady state simulations a) temperature profiles, b) velocity profiles

The 1-D model results were compared with four simulations performed in MFIX by Dr. Jack Ziegler; two transient 1-D simulations (one in cartesian and one in cylindrical coordinates) and two transient 2-D simulations in cartesian coordinates (a one inlet and two inlets configuration). The goal of the comparison was to evaluate the differences due to the different simplifying assumptions (steady state, transient, 1-D and 2-D).

The 2-D MFIX model was based on an Eulerian-Eulerian (E-E) continuum and filtered equation assumptions. The two-fluid model (TFM) equations for gas-particle flows, which has been developed and analyzed extensively over the past five decades, are able to model these flows in a robust manner. These continuum partial differential equations (PDEs) model the multicomponent gases and solids through continuity, momentum, and energy conservation for each of the mixture averaged gas and solids species. Interaction terms appear in the momentum and energy PDE's in addition to an equation of state for the gas mixture and a granular energy PDE for the solids. The computational tool is the multiphase flow interactions with exchanges (MFIX) open source research software. MFIX solves the kinetic theory model equations with a finite-volume method using software primarily developed by the U.S. Department of Energy researchers. More details on the TFM equations and the

constitutive models can be found in the MFIX documentation [80].

In order to utilize the partial slip boundary condition available in the MFIX implementation, Cartesian rather than axisymmetric coordinate systems were utilized. This leads to having an rectangle domain approximation a cylindrical riser. It is generally accepted in the literature that for the solids-phase, the Johnson-Jackson (J-J) partial-slip wall (PSW) boundary condition [83] and similar variants yield the most accurate and physically plausible results when compared to experiments. However, there is still a discrepancy in what parameter values should be used for each riser scale and resolution. The specularity coefficient is difficult to measure and experimental values of specularity coefficients have not been reported for riser flows [84]. The J-J BC is a function of the specularity coefficient, and wall coefficient of restitution, e_w. The specularity coefficient ranges from 0 to 1 (smooth to rough) and relates to the angle of reflection for solids particle wall collisions. The wall coefficient of restitution also ranges from 0 to 1 and relates to the elasticity of the wall collisions, where a zero value is similar to a NSW solids-phase boundary condition. In this study, no-slip boundary conditions were used at the walls for the gas and the partial-slip Johnson and Jackson boundary condition was used for the solids with a specularity coefficient of 0.05 and a wall coefficient of restitution of 1.0. The Gidaspow drag model [85] was used to model the gas/solids interaction and particle-particle collisions were modeled with a coefficient of restitution of 0.9 and a collision angle of 30 degrees. This drag model is comprised of Wen and Yu drag model and Ergun equation, and uses the correlation from experimental data of Richardson and Zaki. The Gidaspow drag model and the Syamlal O'Brien drag model implemented in the 1-D, steady state reactor simulation are compared in reference [85]. Both models give nearly identical drag factor values at solid volume fractions below 0.4. A simple pressure outflow condition was utilized for the exit. In all 2-D simulations for the domain size of 0.08 by 4 meters, 24 cells were used in the horizontal direction and 200 cells in the vertical direction, yielding cells of size 0.00333 x 0.02 meters. In the x- or equivalently the

r-direction the cell size is equivalent to 3.33 particle diameters and in the y-direction 10 particle diameters for the base case 0.5 mm particle size. Using the guide of 10-50 diameters [86], the r-direction is fully resolved and the y-direction is marginally resolved.

The transient solutions were run until a statistical stationary state was reached. The obtained results were then averaged radially and over time. The 1-D equivalent velocity profiles along the reactor height were obtained by first obtaining an average mass flow rate for the gas and solids species, which is equivalent to using weighted averages of the vertical velocity profile with the local mass in each cell as a weight. The comparison of the temperature profiles is shown in Figure 5.2 a-c.

The 1-D steady-state results, averaged 1-D transient results and averaged 2-D results are

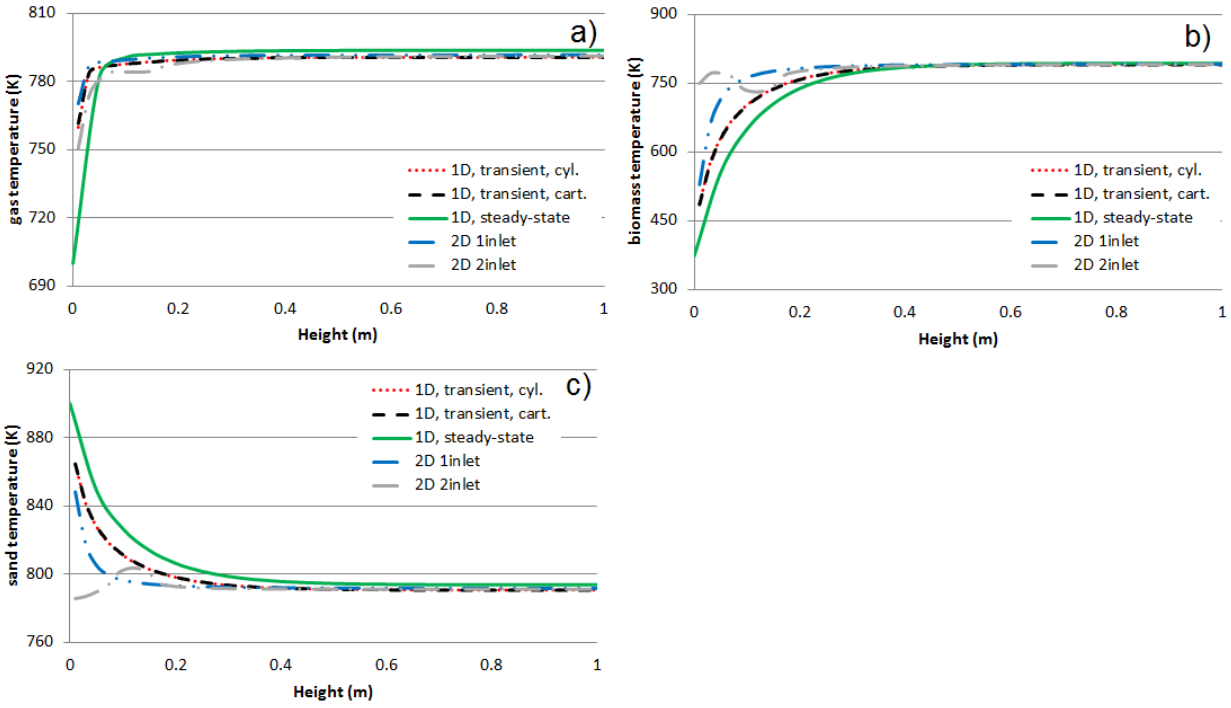

Figure 5.2: Comparison of temperature profiles between the steady-state 1-D simulation results, averaged 1-D MFIX results in cylindrical and cartesian coordinates and averaged 2-D MFIX results with a 1 inlet and 2 inlet configuration for a) gas, b) biomass, c) sand

all in good agreement. There are no significant differences between the simulation results

performed in cylindrical and cartesian coordinates. The inlet configuration does not have a significant effect on the temperature profiles either. Heat transfer rates are high and thermal equilibrium is reached within 0.4 m from the inlet. The averaged 2-D results show slightly higher heat transfer rates compared with the 1-D results, which might be attributed to the effect of clustering and turbulent mixing, which is not captured in the lower order simulations.

Figure 5.3 a-f shows the comparison of the particle and gas velocity profiles and particle and gas volume fractions along the riser height. The 1-D steady state results are in good agreement with the averaged 1D transient MFIX simulation results for both the velocity profiles and the volume fraction profiles. However, the averaged 2-D results show higher solid volume fractions and lower particle velocities compared with the 1-D simulations. This again can be attributed to particle clustering which causes drag reduction. The differences in temperature profiles are not significant due to high heat transfer coefficient rates. The inlet configuration has a limited impact on fluid dynamics and heat transfer. The two inlet configuration results in a slightly higher gas velocity (by approximately 0.1 m/s) and higher gas volume fraction (by approximately 0.01). The differences in solid velocities and volume fractions are negligible.

An additional simulation was performed in order to evaluate the potential impact of the biomass density reduction due to chemical reactions on fluidization conditions. The results are shown in Figure 5.4. Biomass density was reduced by 50% in this simulation. The 1-D steady-state simulation results show no significant effect on velocity profiles, volume fraction profiles or temperature profiles. The inlet volume fraction of the biomass is 9.4% compared to 4.7% in the base-case simulation. As a result, the gas inlet volume fraction decreases from 83.5 % to 78.8 % and the gas inlet velocity increases by 0.4 m/s. However, these differences do not cause any significant changes in temperature or velocity profiles along the reactor.

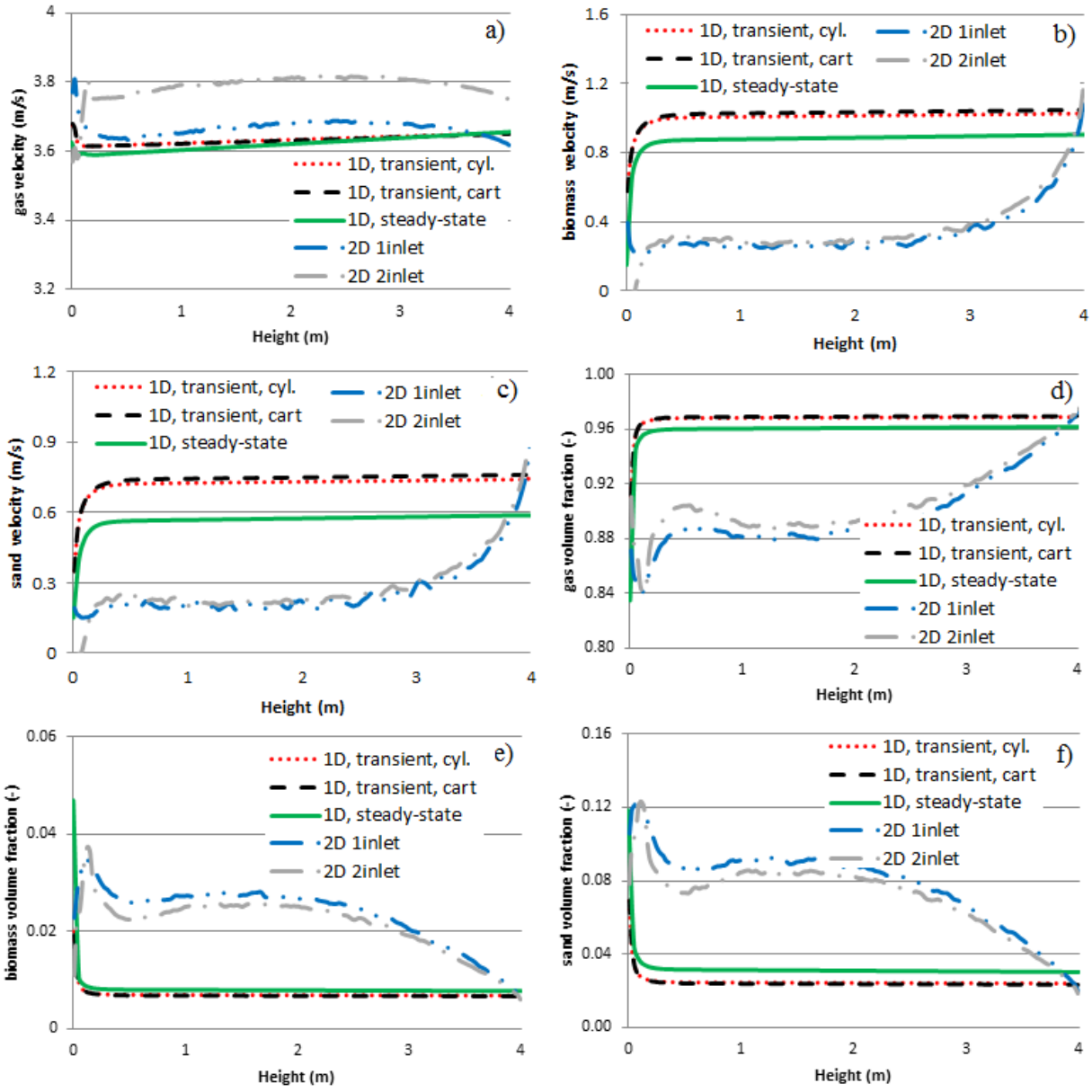

Figure 5.3: Comparison of the velocity and volume fraction profiles between the steady-state 1-D simulation results, averaged 1-D MFIX results in cylindrical and cartesian coordinates and averaged 2-D MFIX results with a 1 inlet and 2 inlet configuration for a) gas velocity, b) biomass velocity, c) sand velocity, d) gas volume fraction, e) biomass volume fraction, f) sand volume fraction

The 1-D MFIX simulation results show higher particle velocities. Biomass particle velocity is 1.4 m/s and sand particle velocity is 1.0 m/s. The predicted gas volume fraction is equal to 0.97 compared to 0.94 in a 1-D steady state solution. The 2-D model consistently predicts

higher solid volume fractions and lower velocities compared to both 1-D models.

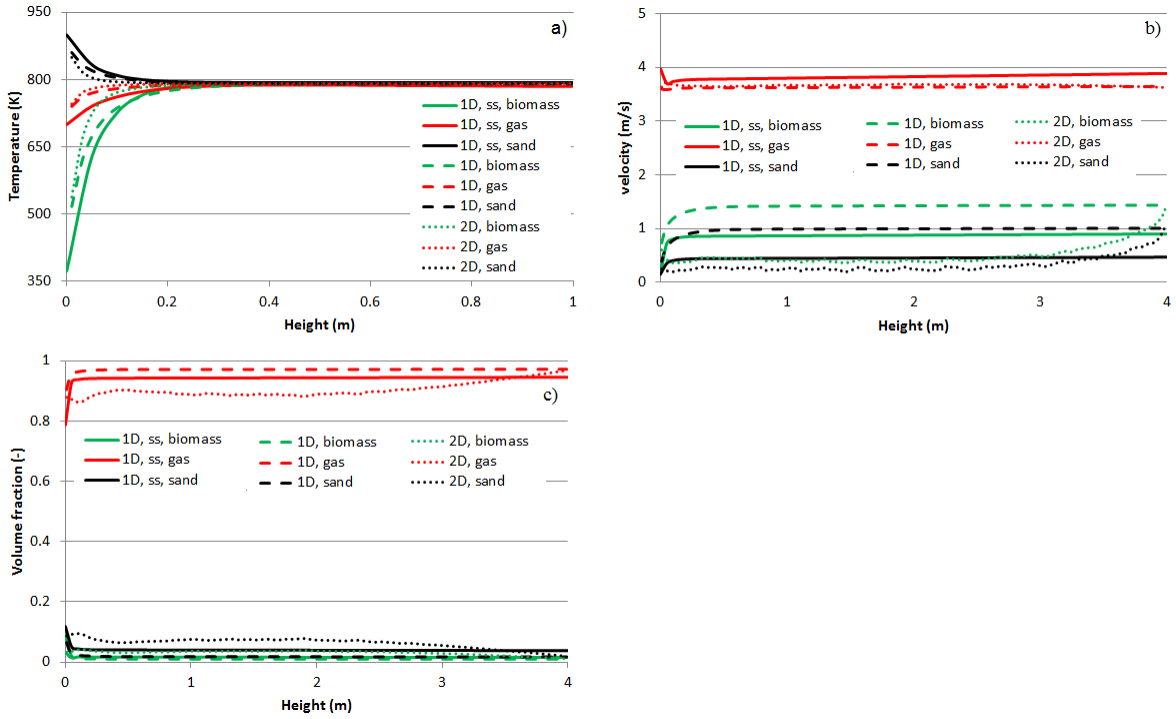

Figure 5.4: Comparison of the simulation results at the biomass density reduced by 50% between the 1-D steady state model, averaged 1-D transient MFIX model and averaged 2-D transient MFIX model a) temperature profiles, b) velocity profiles, c) volume fraction profiles

5.2 External Heat Transfer Coefficient

The external heat transfer coefficient evaluated with the correlation used in MFIX at the reactor inlet is 925 W/m^{2}K. This value is higher than the heat transfer coefficient values reported in the literature between 50-500 W/m^{2}K. In order to verify the value of the external heat transfer coefficient and the simplifying assumptions related to the particle in the 1-D model, simulations of a single particle were performed with a microstructure particle model developed by Dr. Peter Ciesielski at NREL.

The particle model was developed based on the data collected from images of 26,463

poplar particles and 35,977 pine particles. The particles were highly non-spherical, therefore the size and shape of the particles were quantified with the following parameters: Feret diameter, aspect ratio, and projected area. The Feret diameter was defined as the longest distance between two points on the particle diameter and the aspect ratio was evaluated as the ratio of the major axis to the minor axis of an ellipse fitted to the particle. The 3-D particle model was generated by applying a constructive solid geometry (CSG) algorithm to the collected data. The details of the procedure are described in reference [52].

The convective heat transfer coefficient was determined from the following simulations. The biomass particle model was placed in a cylindrical vessel that is initially at ambient temperature and pressure (25 C and 1 atm). Velocity boundary conditions are applied to the top boundary of the simulation vessel, and temperature boundary conditions are applied to all of the walls of the simulation vessel, shown in Figure 5.5. In order to facilitate better numerical stability, these boundary conditions were ramped over time rather than applying them as instantaneous step functions. In the fluid domain of the simulation geometry, coupled continuity, momentum, and energy equations (i.e., the Navier-Stokes equations) were solved for a fully compressible Newtonian fluid. The heat transfer boundary condition at the solid/fluid interface was applied to equate the heat carried to the solid by the fluid the heat conducted into the solid at the interface. The thermal properties of the fluid and the fluid velocity were calculated from the Reynolds and Prandtl dimensionless numbers. Simulations were performed with pine particle of 0.5 mm size class. Simulations were performed for the Reynolds number equal to 10, 100, 500 and 1000 and the Prandtl number equal to 0.1, 0.67, 1 and 3. The Reynolds and Prandtl numbers in the 1-D steady-state reactor were approximately 100 and 0.67. Additional simulations were performed in order to create data points for correlating the heat transfer coefficient to the Prandtl and Reynolds numbers. A new correlation for the Nusselt number as a function of Reynolds and Prandtl numbers was developed by fitting the heat transfer coefficient data with the least squares method in

Figure 5.5: Schematic of the computational domain used for single particle simulations

Matlab by Dr. Ciesielski. The developed correlation is given by equation 5.1.

$$Nu = -0.7438(1 + 2.1016Re^{-0.88}Pr^{0.6553} + 2.2811Re^{0.17}Pr^{0.14}) \tag{5.1}$$

The heat transfer coefficient evaluated at the Reynolds and Prandtl numbers equal to the values in the 1-D reactor model was equal to 513 W/m^2-K, which is roughly half of the 925 W/m^{2}K evaluated with MFIX. This disparity is not surprising, considering that the experiments from which the Gunn correlation were derived were performed using glass spheres, and that glass has a much higher thermal conductivity than biomass and that biomass particles are notably non-spherical. The effect of this disparity for heat transfer in the biomass pyrolysis reactor is evaluated. The comparison of the 1-D steady-state reactor model simulation results with the two different correlations for the Nusselt number for the particle size of 0.5 mm and 2 mm is shown in Figure 5.6 a) and b).

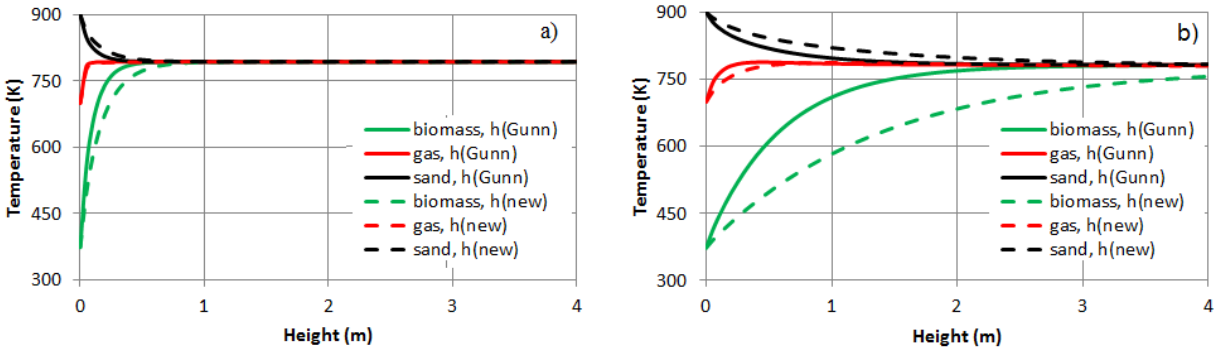

Figure 5.6: Comparison of temperature profiles evaluated with the external heat transfer coefficient evaluated based on the Nusselt number correlations from MFIX documentation and developed based on single particle simulations a) biomass particle size of 0.5 mm, b) biomass particle size of 2 mm.

Although the heat transfer coefficient evaluated with the new correlation is lower by nearly a factor of two, and therefore the heat transfer to biomass particles is slower, the difference between the average biomass temperature profiles is relatively small for the 0.5 mm biomass particles. However, in the case of 2 mm biomass particles, the difference is more significant. This proves that external heat transfer rates could possibly become a limiting

factor for pyrolysis reactions when the reactor operates with larger biomass particles. Therefore the effect of the heat transfer coefficient on the reaction rates will be considered in the next chapter. It is worth noticing that single particle simulations most likely underpredict the values of the external heat transfer coefficients because there are particle collisions are neglected. Therefore the real value of the external heat transfer coefficient is likely in the range between the value predicted by the two considered correlations.

5.3 Particle Size

Increasing the particle size requires an increased gas flow rate in order to maintain the fast fluidization regime. This is due to a larger gravity force resulting from a larger particle mass. Increased mass flow rate of the gas results in an increased gas velocity. The gas velocity required for entrainment of 0.5 mm, 1 mm and 2 mm particles is 3.8 m/s, 6.5 m/s and 10 m/s respectively. The simulations were run such that the biomass particle velocities and sand particle velocities in different simulations were kept constant. This is because the differences in velocities result in different particle residence times in the reactor. The residence time of biomass and sand particles was approximately 4.5 s and 9.5 s respectively. The residence time of the gas decreased with the increasing gas velocity from 1 s in the base-case simulation to 0.4 s at 2 mm particle size. Solid and gas volume fractions were equal to the values in the base case as the particle velocities were equal.

Temperature profiles plotted along the reactor height are shown in Figure 5.7. Heat transfer to biomass particles (represented by the average biomass temperature) slows down with the increased particle size as the intraparticle heat transfer becomes limiting. The thermal equilibrium is reached at 0.5 meters, 1 meter and 2.5 meters from the reactor inlet at particle size of 0.5 mm, 1 mm and 2 mm respectively according to the 1-D steady state simulation results. This result indicates that the heat transfer might eventually impede chemical reactions and cause incomplete conversion in case of using bigger biomass particles in the considered reactor. Moreover, the increased flowrate of fluidizing gas results in a decreased

equilibrium temperature without adjusting either the temperature or mass flow rate of sand. The equilibrium temperatures are 794K, 788K and 782K for 0.5 mm, 1 mm and 2 mm particles respectively according to the 1-D steady state simulation results. Therefore, increasing the particle size will require adjusting both the gas flowrate and the sand temperature in order to maintain the optimum pyrolysis temperature.

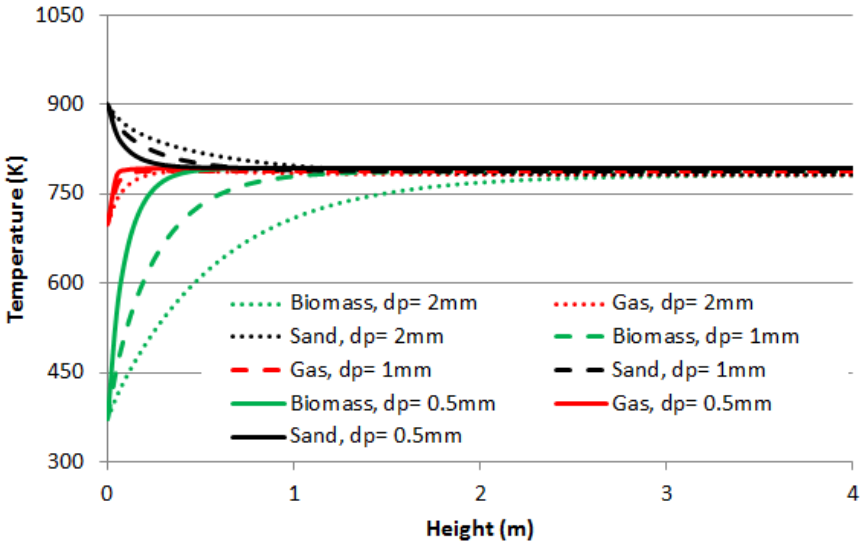

Figure 5.7: Comparison of biomass, sand and gas average temperature profiles along the reactor height evaluated for particle size of 0.5 mm, 1 mm and 2 mm

The 1-D steady state simulation results for 1 mm and 2 mm particles were compared with the 1-D MFIX simulation results in cartesian coordinates and 2-D MFIX simulation results in cartesian coordinates in the one inlet configuration. The cartesian coordinates were chosen for this comparison because this geometry enables the use of partial slip boundary condition at the wall. In the cartesian coordinates, the gas flow rate was adjusted to account for the differences in the cross-section area such that the gas inlet velocity was the same as in the 1-D, steady-state simulation. As shown in figure 5.8 a and c, velocity and volume fraction profiles are in good agreement at the 1 mm particle size. The particle velocities evaluated from the 2-D MFIX model are consistently lower than the velocities evaluated from the 1-D

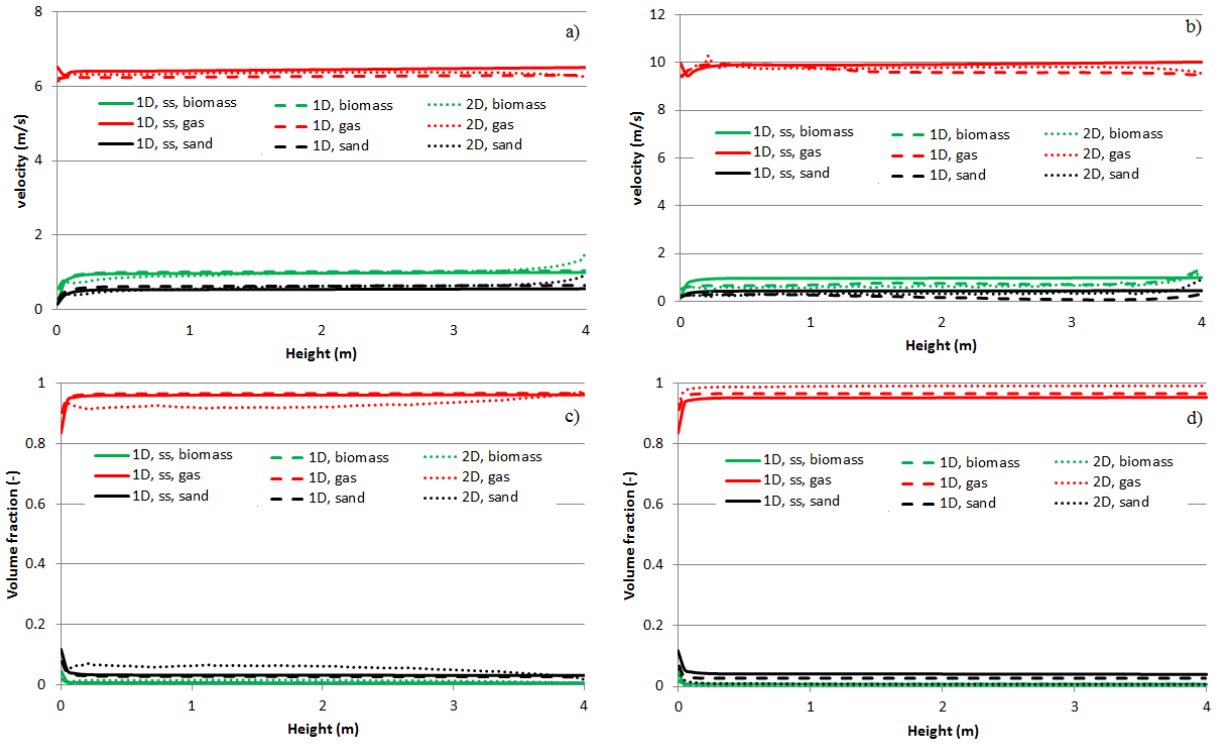

Figure 5.8: Comparison of biomass, sand and gas average velocity and volume fraction profiles along the reactor height between the 1-D steady state model, 1-D MFIX model and 2-D MFIX model evaluated for particle size of a) 1 mm, b) 2 mm

MFIX model due to the aforementioned clustering effect.

As previously described, there is an interest in using the developed reactor model for simulating catalytic vapor phase upgrading (VPU) reactors, which operate at much smaller particle sizes. The catalyst typically used in vapor phase upgrading is zeolite with particle size between 60 and 120 microns. These are type A particles with different fluidization characteristics than type B particles used in the pyrolysis riser reactor. Therefore, there is a concern about the applicability of the drag model to this new application. Moreover, it is important to assess the impact of particle clustering on the results. Small particles have a stronger tendency to agglomerate and form transient clusters which affect the fluidization characteristics and residence time. This phenomenon is not accounted for in 1-D simulations,

therefore it is important to evaluate the magnitude of this effect and develop a correction for the 1D model (if necessary). In order to verify the applicability of the drag model, the additional simulation was performed with the 1-D steady-state model and a 2-D transient model in MFIX.

The riser reactor diameter was 0.01 m and the height was 3 m in this simulation. The 1-D, steady-state model was discretized with a constant step of 0.025 m. The 2-D transient simulations in MFIX were performed in a rectangular computational domain comprised of 96 cells in the horizontal direction and 5088 cells in the vertical direction (cell size of 0.0006 m), which ensured the resolution of less than 8 particle diameters. The no-slip wall (NSW) gas-phase BC and the Johnson and Jackson (J-J) partial-slip solids boundary conditions were employed in the simulations. The simulations were performed under isothermal conditions at 400^{o}C. The inlet gas pressure was 2.73 bar. The particle size was 80 μm and bulk particle density was 1560 kg/m^3. The mass flows of solid and gas were 0.39 g/s and 1.11 g/s respectively. The fluidizing gas was representative of pyrolysis vapors with an average molecular weight of 77.5 g/mol.

The comparison of gas velocity, particle velocity and gas volume fraction for the vapor phase upgrading reactor is shown in Figure 5.9. There is an excellent agreement between the 1-D steady state simulation results and time and spatially averaged 2-D MFIX simulation results. This proves that the 1-D model can be used to describe small FCC particles and therefore can potentially be used to simulate vapor phase upgrading process in a riser reactor. Although a detailed analysis of the flow conditions is beyond the scope of this work, the interesting features of the flow are a very small slip between the particle velocity and the gas velocity and a high gas volume fraction (>99%). The momentum exchange at the riser inlet is very intense and steady velocities and volume fractions are achieved nearly instantaneously with no significant changes farther along the reactor height. The validation of the

simulation results is not possible at present due to the lack of experimental data. However, validation is highly recommended when experimental data become available.

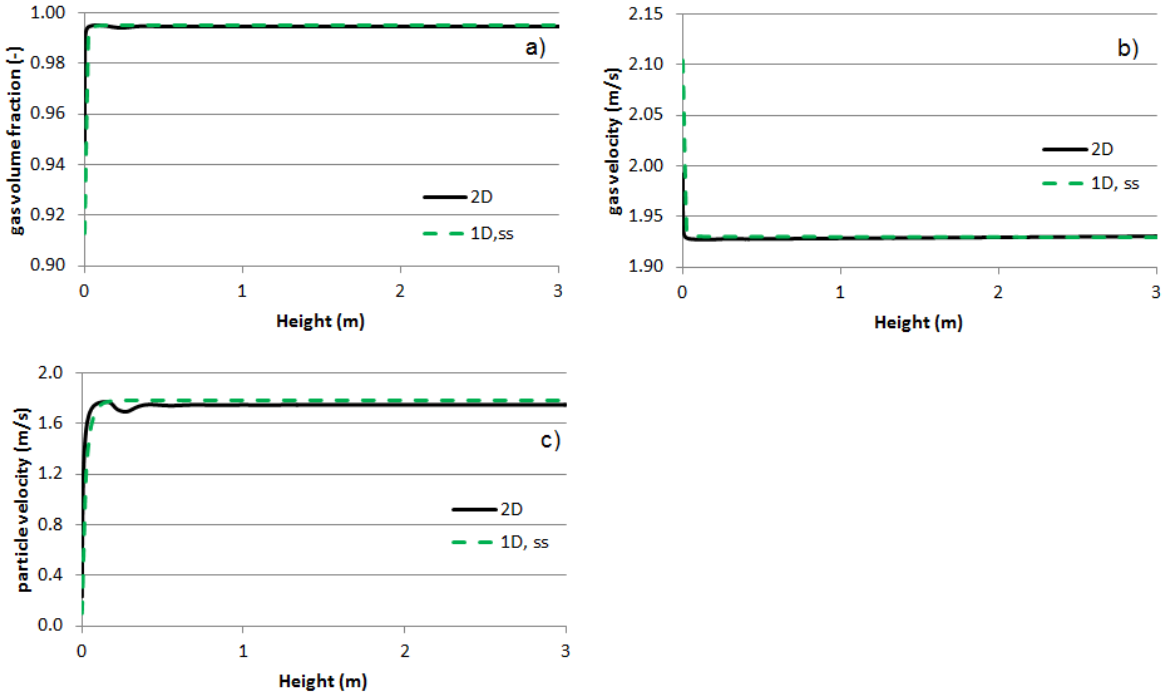

Figure 5.9: Comparison of gas volume fraction, gas velocity and particle velocity obtained from 1-D simulation, 2-D simulation in a riser reactor with Geldart A particles

5.4 Temperature and Pressure

The effect of temperature on fluidization conditions is evaluated by comparing the base-case simulation results to the cold flow simulation results. The elevated temperature has no effect on particle velocities and volume fractions, since these are kept constant in order to ensure equal residence times. However, the mass flow rate needs to be adjusted due to reduced density and increased viscosity at higher temperatures. As a result, the fluidizing gas velocity in cold flow is 2.8 m/s compared with 3.8 m/s at 500°C. The cold flow velocity profiles and volume fraction profiles are in excellent agreement with the 1-D and 2-D MFIX simulation results as presented in Figure 5.10 a and b.

Operation at elevated fluidizing gas pressure requires a higher mass flow rate of fluidizing

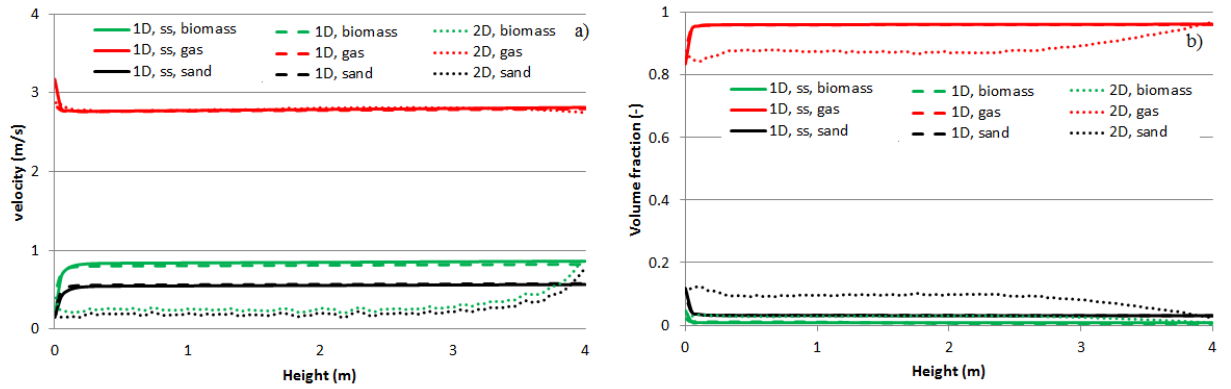

Figure 5.10: Comparison of the cold flow simulation results between the 1-D steady state model, averaged 1-D transient MFIX model and averaged 2-D transient MFIX model a) velocity profiles, b) volume fraction profiles

gas due to increased gas density. The gas velocity required for fast fluidization is 2.5 m/s compared to 3.8 m/s in the base case. The temperature profiles are not significantly affected by reactor pressurization. The equilibrium temperature in the pressurized reactor is 783K, which is lower by 10K compared to the base case due to the increased mass flow rate of fluidizing gas. The comparison of the temperature profiles, velocity profiles and volume fraction profiles to the 1-D and 2-D MFIX simulation results is provided in Appendix B. The particle velocities and volume fraction profiles are in excellent agreement between the 1-D steady state and 1-D MFIX models. The 2-D MFIX model consistently predicts higher solid volume fractions and lower particle velocities due to the particle clustering. Lower velocities result in longer residence times in the reactor which is likely the reason for the faster heat transfer along the reactor height.

5.5 Sand-to-Biomass Ratio

Changing the total mass flow rate of sand affects the temperatures, volume fractions and gas velocities. The comparison of the temperature profiles for sand-to-biomass ratio (R) of 7.8, 10 and 15 is shown in Figure 5.11.

In the simulation, heat transfer rate is not significantly affected by the sand mass flow rate.

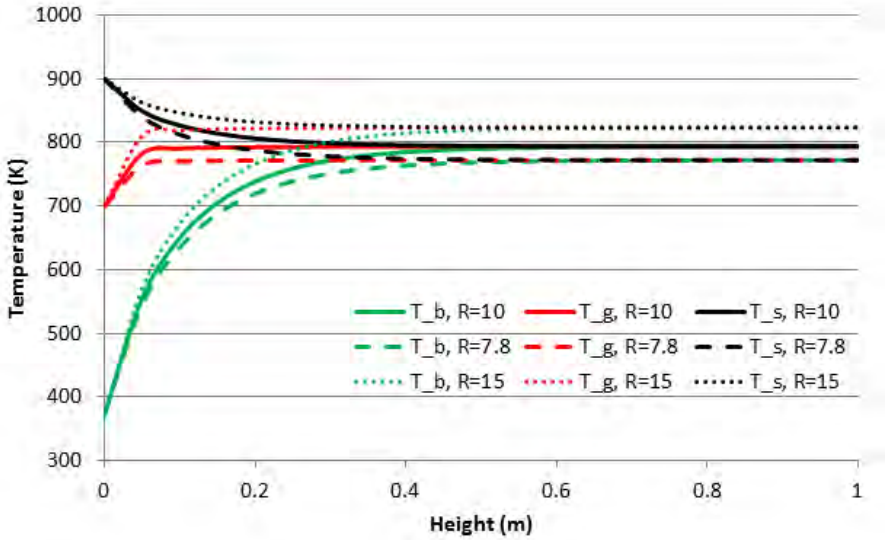

Figure 5.11: Comparison of biomass, sand and gas average temperature profiles along the reactor height evaluated for particle size of 0.5 mm, 1 mm and 2 mm

The equilibrium temperature increases at higher sand-to-biomass ratio due to increased heat capacity. The equilibrium temperature is equal to 772K, 793K and 823K at sand-to-biomass ratio of 7.8, 10 and 15 respectively. Higher mass flow rate of sand also results in a reduced gas volume fraction. The equilibrium gas volume fraction is 0.97, 0.96 and 0.95 at sand-to-biomass ratio of 7.8, 10 and 15 respectively. The respective gas volume fractions at the inlet are 0.86, 0.83 and 0.78. Finally, the mass flowrate of fluidizing gas needed to be adjusted in order to ensure equal particle velocities at changed solid mass flowrate. The gas velocity required in order to maintain equal particle velocities is approximately 3.9 m/s for all considered sand-to-biomass ratios. The comparison between the 1-D steady state, 1-D and 2-D MFIX models shows the same characteristics as in previous simulations; both 1-D model results are in excellent agreement and the 2-D model predicts lower particle velocities and higher solid volume fractions. The Figures illustrating the temperature profiles, velocity profiles and volume fraction profiles are provided in Appendix B.

5.6 Gas-to-Biomass Ratio

Reducing the flow rate of fluidizing gas, at all the remaining parameters kept constant, results in reduced particle velocities. The biomass and sand particle velocities are 0.4 m/s and 0.2 m/s respectively when the fluidizing gas-to-biomass ratio is reduced from 0.75 to 0.5. Further reduction of the fluidizing gas flowrate would eventually result in the insufficient momentum for particle entrainment and transition to the bubbling fluidization regime. Reduced fluidizing gas flowrate also results in an increased equilibrium temperature by 3 K and increased particle residence time. The comparison of the temperature profiles, velocity profiles and volume fraction profiles is provided in Appendix B as the general trends remain consistent with previously described characteristics.

5.7 Hydrogen Addition

Introduction of hydrogen to the fluidizing gas causes changes in the properties of the fluidizing gas mixture; gas density and viscosity are reduced and gas heat capacity (kJ/kg-K) is significantly increased. Since hydrogen becomes more reactive at higher pressures, industrial scale reactors operating with hydrogen rich gas mixtures are typically pressurized (no reactions included in this study). Therefore in order to evaluate the effect of hydrogen addition to the fluidizing gas, simulations with hydrogen rich fluidizing gas at 2.3 bar and 8.5 bar are compared to the base case. The latter pressure is a compromise between pressurizing the system for improved reaction kinetics on one hand and increased material and safety requirements due to elevated pressure on the other hand. The gas velocity required for fluidization with hydrogen rich gas (18.9% H_2 by weight) is 6 m/s and 4 m/s at 2.3 bar and 8.5 bar gas pressure respectively, compared to 3.8 m/s in the base case. It is interesting to notice that the effect of reduced gas density due to hydrogen addition is almost entirely offset by system pressurization at 8.5 bar. The equilibrium temperature is also affected due to the increased heat capacity of the fluidizing gas. The equilibrium temperatures for hydrogen rich

gas operation are 787K and 772K at 2.3 bar and 8.5 bar gas pressure respectively, compared with 793K in the base case. In the pressurized system the lower equilibrium temperature is also due to the increased mass flowrate of fluidizing gas compared to the base case. The comparison of the temperature profiles, velocity profiles and volume fraction profiles is provided in Appendix B as the general trends remain consistent with the previously described characteristics.

5.8 Conclusions

Riser simulations with the 1-D, steady state model show that thermally and hydrodynamically fully developed flow is reached nearly at the reactor inlet due to intense momentum transfer and high heat transfer rates. Model verification with 1-D and 2-D transient models developed with MFIX software shows good aggrement with respect to temperature and gas velocity profiles. However, discrepancies are observed between particle velocity profiles between 1-D and 2-D models. It is suspected that particle clustering (not captured in 1-D simulations) is the cause of these differences. The performed parametric study shows that the two most influential parameters are particle size and fluidizing gas composition. Particle size is an important parameter for fast pyrolysis reactor design because it affects biomass particle temperature. Heat transfer to biomass particle decreases with an increased particle size, as the intraparticle heat transfer becomes limiting due to the low thermal conductivity of biomass. Therefore, it might become rate limiting and lead to incomplete conversion. Fluidizing gas composition is an important parameter for fast pyrolysis reactor design because gas properties affect fluidization conditions. Changing gas properties (for example reducing gas density by hydrogen addition) might lead to the transition from fast fluidization to bubbling fluidization without adjusting the gas mass flow rate. The developed 1-D model allows to resolve the axial temperature profiles and axial velocity profiles and is therefore a useful tool for tweaking the operating parameters, assisting with determining reactor geometry and calculating gas residence time in the reactor. The advantage of the steady state model

is the short computational time (3-10 sec) compared to 1 day required for 2-D, transient simulations to converge.

CHAPTER 6
MODEL VALIDATION

Publicly available literature data on a cold flow CFB riser unit at National Energy Technology Laboratory (NETL) [13] were chosen for validation of the 1-D steady state model, and 1-D, 2-D and 3-D transient riser reactor models in MFIX. The experimental reactor was reported as approximately 16 m tall with a diameter of 0.3 m. The experiments were performed at ambient temperature and pressure with polyethylene particles and air. The average particle size was 0.8 mm. The inlet superficial gas velocity was 5.7 m/s and the solids mass flow was 5.5 kg/s. The available experimental results include radial velocity profiles measured with a fiber optic instrument and high speed particle velocimetry, radial solid mass flux profiles at three points above the riser inlet (6.23 m, 8.88 m and 13.33 m), and pressure drop distribution along the reactor height. A summary schematic with geometry and operational parameters is given in Figure 6.1.

The 1-D model was discretized using a constant step size of 0.05 m. In 2-D the effect of the sideways-oriented outlet is also tested. In the multidimensional simulations, a solid volume fraction of 0.5 was assumed at the horizontally orientated solids inlet, yielding solids velocity of 0.23 m/s in 2-D and 3-D with a 0.23 m x 0.305 m solids inlet. In 2-D the horizontally orientated outlet was also simulated to resemble the NETL experimental setup depicted in Figure 6.1. Initially a 2-D cylindrical coordinate system was used to more easily model the domain, however, it was abandoned due to unphysical solids clustering and negative solids flow at the symmetry boundary condition. Therefore, 2-D cartesian simulations were conducted for an approximation of a 'slice' of physical reactor. A mesh with 48 x 192 cells were used with the Gidaspow drag model [80] to model the gas/solids interaction. The residuals for the implicit method were controlled by error tolerances of 0.001.

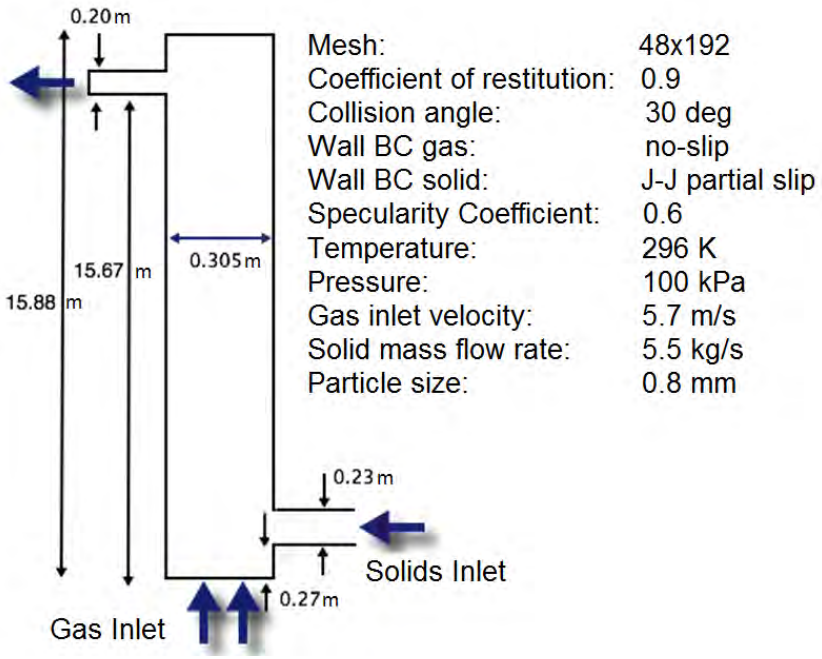

Figure 6.1: Schematic of the 2-D model represtation of the cold flow experimental reactor at NETL.

Particle-particle collisions were modeled with a coefficient of restitution of 0.9 and a collision angle of 30 degrees. At the walls, no-slip boundary conditions were used for the gas and the partial-slip Johnson and Jackson boundary condition was used for the solids with a specularity coefficient of 0.6 and a wall coefficient of restitution of 0.9. A simple pressure outflow condition was utilized for the exit. The time averaged traces for the 2-D simulation were conducted from a simulation time of 20 to 31 seconds, as the mass accumulation stabilized at approximately 20 seconds. The time averaged traces for the 3-D simulation were conducted from a simulation time of 20 to 76 seconds. The 2-D and 3-Dvelocity fields were reduced to one-dimension by finding the time averaged mass flux for each cross section at each height (the average over a line in 2-D and an area in 3-D) and dividing theis by the time averaged volume fraction for each of these crosss sections.

6.1 Pressure Gradient and Solids Inventory

The pressure drop axial profiles, illustrated in Figure 6.2, show that the 1-D models and the 2-D models significantly underpredict the pressure drop in the reactor. The experimental pressure drop is approximately 1.5 kPa/m compared to only 0.3 kPa/m predicted by the 1-D models, and 0.5 kPa/m evaluated from the 2-D models. The bulk of the pressure gradient which determines the total pressure drop across the riser is largely influenced by the static pressure gradient created through gravity by the mass distribution of the solid particles in the riser. Therefore, the total solids mass inventory, as shown in Table 6.1, is also underestimated and related to the pressure drop.

The statistical stationary state (SSS) value of the total solids mass is determined largely by the severity of the drag law and its ability to represent the gas-solid interaction forces on single particles and dense clusters. The 1-D simulations are unable to capture the drag reduction induced by multi-dimensional clustering, overestimate the drag, and propel the particles quickly through the reactor. This leads to a small mass inventory and pressure drop. In 2-D and 3-D, clustering freely forms and the mass inventory increases as spatial dimensions are added. As shown by the experimentally determined pressure gradient, the

Table 6.1: Comparison of the experimental mass inventory with simulation results from the 1D steady-state model, 1-D, 2-D and 3-D models in MFIX

	Exp.	1-D, S-S	1-D	2-D Top-Out.	2-D Side-Out.	3-D Top-Out.
Invent. (kg)	442 ± 11	27	15	80	86	130

actual riser has more solids than in the simulations at every measured location from 1 to 16 meters. However, as shown in Figure 6.3, by estimating the gas volume fraction in the experimental reactor, there is an inconsistency with a larger gas volume fraction at the 3 measured points. These fractions were determined by radially averaging the solids flux and velocities at the 3 positions to determine the volume fraction, and it appears that the solids

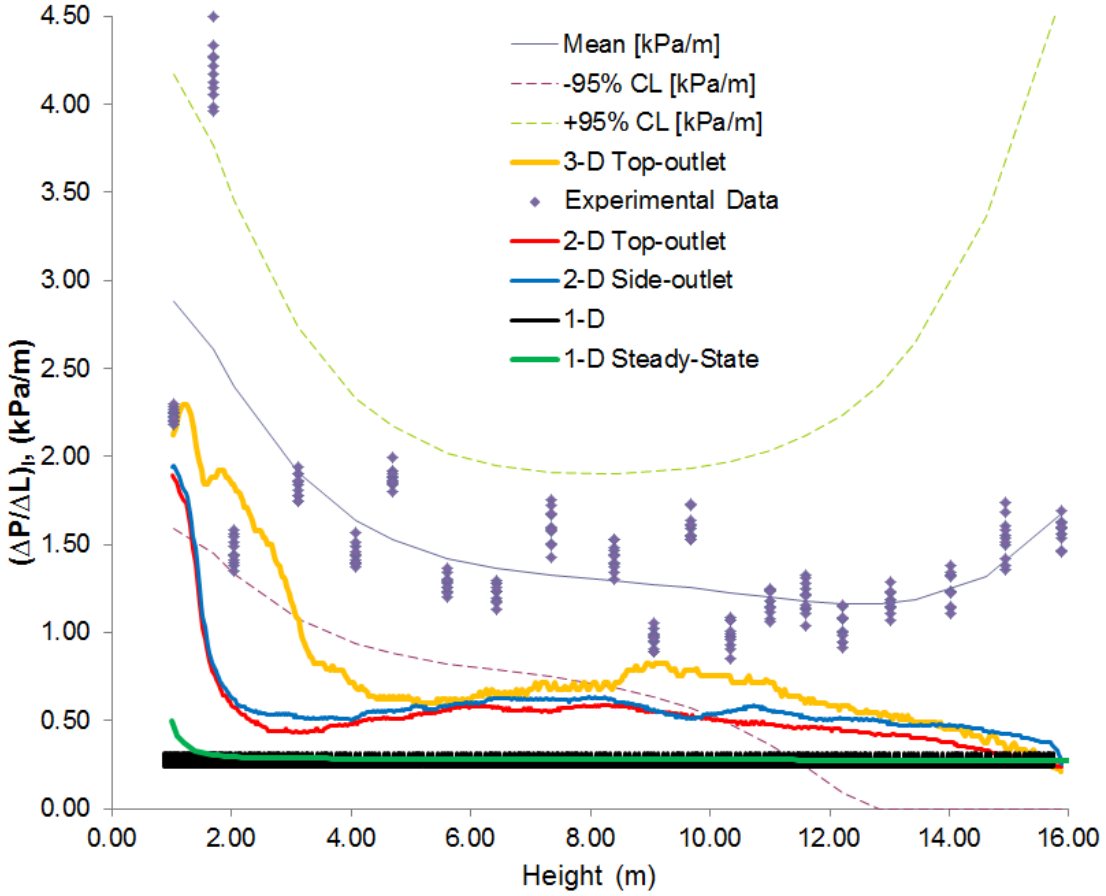

Figure 6.2: Comparison of unit pressure drop profiles (kPa/m) evaluated with a steady-state 1-D model, transient 1-D model and transient 2-D models with different outlet configurations with experimental data.

velocity probe was unable to resolve the very near wall velocities and fluxes, leading to smaller solids volume fractions (higher gas volume fractions) than reality. Also the approximation of the cylindrical riser with a rectangular domain in 2-D and 3-D and the lack of an sideways orientated outlet in 3-D contribute to the disagreement. In the experiment, for the last 2 meters of the riser, there is a large increase in the pressure gradient due to the outlet and this is observed in a small increase in the pressure gradient in the 2-D side-outlet simulation.

6.2 Solids Flux and Velocity Profiles

The 1-D model only allows for a comparison of the radially averaged, steady-state properties. Therefore, the experimental, spatially and mass averaged properties along the axial direction of the riser had to be estimated. Using the relation of the static pressure to the weight of solid mass supported in the riser, the pressure gradient was used to estimate (ignoring friction) the solid volume fraction and through assuming a steady-state operation, the average solids velocity.

Not surprisingly, due to the overestimated drag, the 1-D models are in disagreement for both the 2D/3D models and experimental data. A comparison of the axial gas velocity, solid velocity, gas volume fraction and solid volume fraction profiles evaluated with the 1-D steady state model, 1-D, 2-D models with the top outlet and side outlet configuration, and 3-D MFIX model with the top outlet configuration is shown in Figure 6.3. The inlet effects are best captured in 3-D and the outlet effects with 2-D sideways outlet configuration.

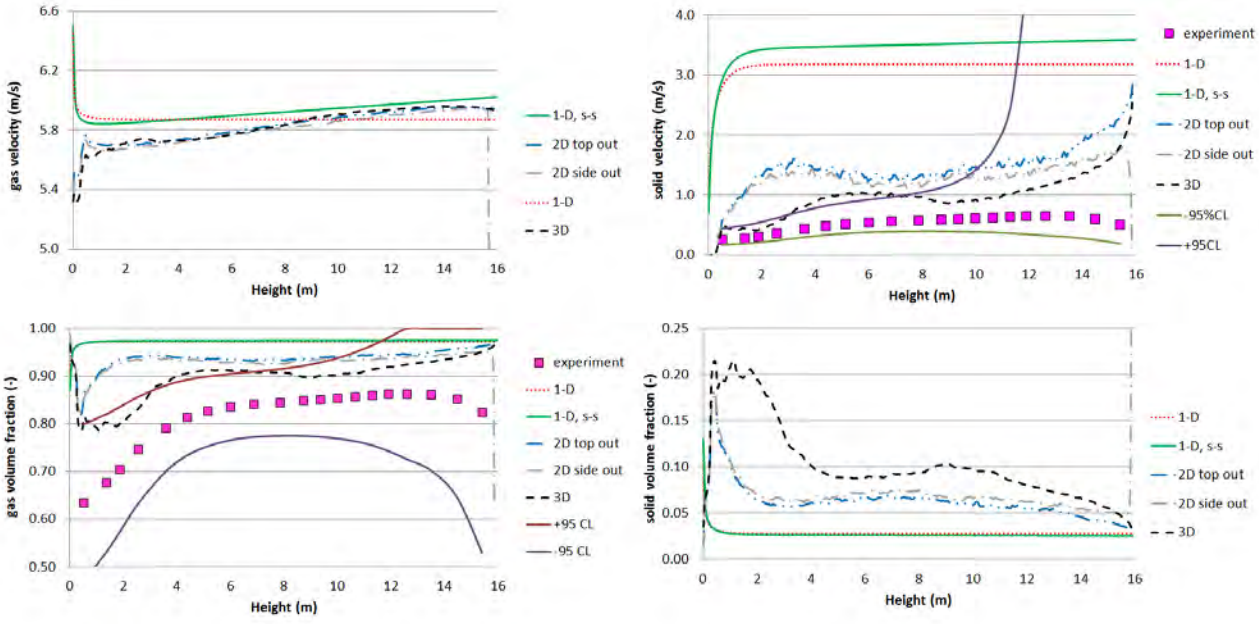

Figure 6.3: Comparison of velocity and volume fraction profiles evaluated with a steady-state 1-D model, transient 1-D, 2-D and 3-D models with different outlet configurations with experimental data.

The gas velocities are less insensitive to the model and spatial dimensions. All the model predictions of gas velocity are in good agreement. The 1-D models (both the steady-state model and MFIX model) consistently overpredict solid particle velocities and consequently underpredict solid volume fraction. The 2-D and 3-D MFIX model predictions of the solid velocities are in better accordance with experimental data. The results show that the outlet configuration has a minor effect on model predictions. The simulation results and the comparison with experimental data leads to the conclusion that the drag model in the 1-D reactor model should be adjusted for particle clustering in order to improve the predictions of the velocity, volume fraction and pressure drop profiles.

The first attempt of adjusting the drag model was made by performing two additional simulations. Firstly, the drag was adjusted by reducing the drag coefficient by a factor of 2. The second approach was to account for particle clustering by increasing the effective particle size to 2 mm. The comparison of the velocity and volume fraction profiles is shown in Figure 6.4. The solid velocity and volume fractions are in better agreement with the experimental data after drag reduction or increasing the particle size. However, the axial velocities are still ovepredicted in the 1-D results. Moreover, the pressure drop and mass inventory are still severely underpredicted. This leads to the conclusion that particle clustering is dependent on many factors, such as particle and gas properties. Therefore, adjusting the drag requires multiple simulations and collection of experimental data which is beyond the scope of this study.

The respective experimental radial particle velocity measurements and MFIX simulation results are shown in Figure 6.5 a) and b) The experimentally determined particle velocity profiles have a parabolic shape at all three measurement points. Under the considered experimental conditions, which correspond to conditions prevailing in CFB risers, the particle velocity is the highest at the centerline and is nearly zero close to the reactor walls. The

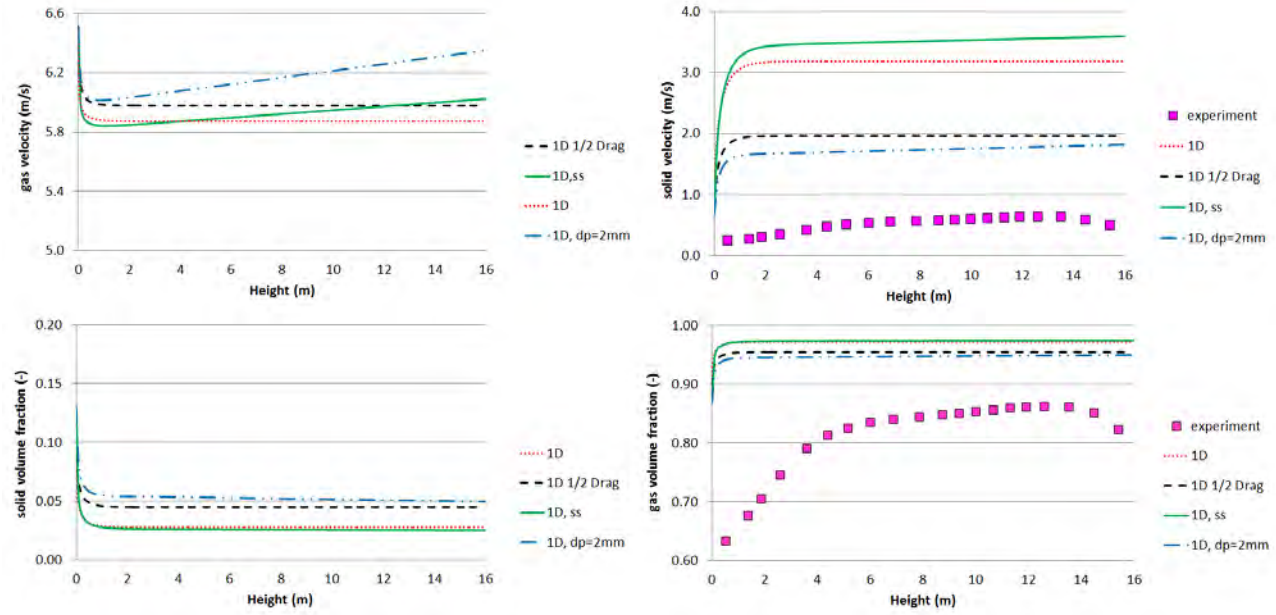

Figure 6.4: Comparison of velocity and volume fraction profiles evaluated with a steady-state 1-D model, transient 1-D model, steady state 1-D models with a reduced drag coefficient and increased effective particle size with experimental data.

experimental radial velocity profiles are in general in agreement with the simulation results. However, 2-D and 3-D MFIX models underpredict particle velocities. This can be explained by looking at the comparison of the mass flux radial profiles, shown in Figure 6.5 b. The downward moving region in the simulations is too wide in 2-D and 3-D. However, the mass inventory and pressure gradient comparison shows that the solids volume fraction is in general also too low compared to the experimental data. It is suspected that this is due to the immeasurable solids wall velocity in the thin region which the mass flux and velocity probes are unable to capture. In the 2-D and 3-D simulations the solid volume fraction is too high near the centerline (because of the down flow at the walls), which leads to the solids velocity peak being too low.

Improvements of the drag law in 2-D and 3-D and inclusion of the cylindrical domain would bring these profiles in agreement. In order to capture the large pressure gradients near the riser inlet, an improved drag law would also need to capture the cluster behavior in the

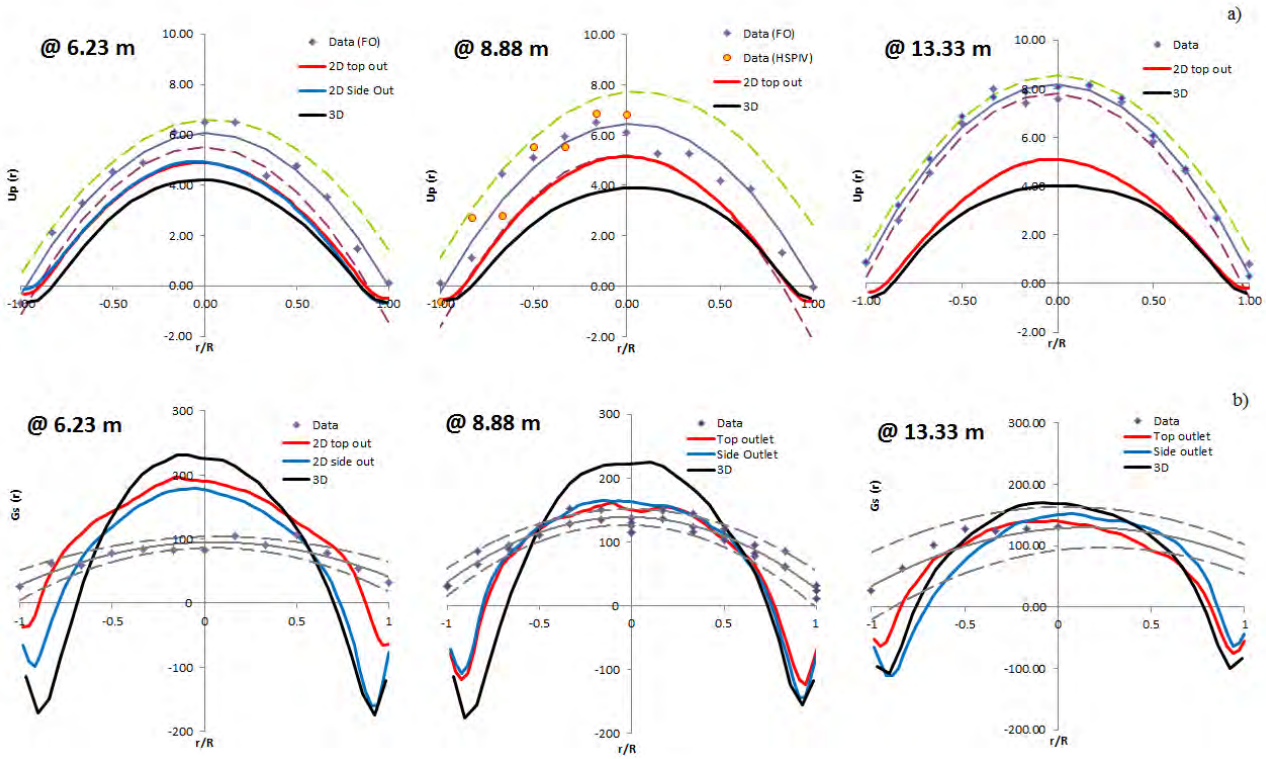

Figure 6.5: Comparison of the experimentally measured radial profiles of a) solid velocity and b) solid mass flux at 6.23 m, 8.88 m and 13.33 m above the cold flow riser inlet to the radial profiles evaluated with the 2-D and 3-D MFIX models.

dense high solids volume fraction regime. The developed riser models currently use the standard Gidaspow drag law, and therefore these results could be greatly improved with a fitting of the drag law using the minimum fluidization velocity. However, a fitted drag-law with the Syam-Obrien method [80] would only apply to these particular polyethylene particles, as the drag is a function of gas properties and the particle diameter, density, and particle size distribution. Therefore even the adjusted drag model would not be directly applicable to the pyrolysis simulation of interest with different particle parameters and an investigation of unknown pyrolysis reactor conditions is warranted through the use of the original non-fitted drag law.

6.3 Conclusions

The presented validation study shows that the 1-D steady-state model is not capable of accurately predicting particle velocities, pressure drop and mass inventory in a riser reactor. The 2-D transient models provide better estimates of particle velocities, however, they are still not able to accurately predict the pressure drop and mass inventory. The very computationally intensive 3-D transient models provide better results compared to the 1-D and 2-D models, however, they are still uncapable of matching the experimental pressure drop and solids inventory. The cause of the discrepancies between the experimental data and model results is due to the drag model. Drag model is based on empirically determined drag coefficients which might not be directly applicable to multiphase flow systems operating with particles and gas of different properties. Therefore, it is recommended to adjust the drag model for a particular application in order to improve the accuracy and flexibility of reactor models. The simulation results also indicate that the experimental data are not free of errors. The comparison of the radial distributions of solids velocity, mass flux and solids inventory leads to the conclusion that the experimental probe did not capture the downward flow of solids near the wall. Therefore, the experimentally measured solid velocities and gas volume fractions are higher than the actual values. The performed analysis proves that plug ow is not a realistic assumption for describing the solids-gas flow in risers, however, with a proper adjustment of the drag model, the 1-D reactor model might still prove practical. This is because of the fact that the main cause of the discrepancies between the models and experimental data is the empirical drag model. Therefore, it might be concluded that increasing model complexity (2-D, 3-D) without implementing a case-specific drag model results in an increased computational cost and not necessarily improved results. With the overpredicted particle velocities, the 1-D models underpredict particle residence times, which is important for evaluating biomass conversion in reactive simulations.

CHAPTER 7

PARAMETRIC STUDY OF A BIOMASS FAST PYROLYSIS RISER REACTOR

The effect of operating conditions and feedstock composition on the fast pyrolysis product yields and composition was evaluated by running 1-D, steady- state simulations of the reactor. The reactor diameter was 0.08 m and reactor height was 4 m, for consistency with the reactor geometry used for non-reactive simulations. The discretization of the computational domain, however, needed to be adjusted due to higher resolution required in order to resolve the fast pyrolysis reactions. The domain was split into two sections; the first section with a cell size of 0.005m and the second section with a cell size of 0.025. The length of the high resolution section was adjusted depending on the needs of a particular simulation. For most simulations it was sufficient to use a 0.5 m high resolution section, however with larger particle size, it was required to extend this section up to 1.5 m. The following parameters were considered in the simulations: particle size, reaction temperature, system pressurization, hydrogen addition to the fluidizing gas, sand-to-biomass ratio, and gas-to-biomass ratio. The base case simulations were performed for three representative biomass feedstocks: pine, corn stover and switchgrass. The chemical composition of the considered feedstocks is summarized in Table 4.2 in chapter 4. All simulations were run such that the temperature at the reactor outlet was 500^{o}C, which is an optimal pyrolysis temperature. The desired outlet temperature was achieved by adjusting the inlet temperature of inert solids. This could be easily achieved in practice by adjusting the air mass flow rate in the char combustor or other control mechanisms such as the adjustment of steam generation.

7.1 Base Case

The base case simulation was run at a gas-to-biomass ratio of 0.5 and sand-to-biomass ratio of 10. The biomass feedstock was pine. The biomass, gas and sand inlet temperatures were 373 K, 700 K and 880 K respectively. The input parameters are summarized in Chapter

4. As shown in Figure 7.1 a, heat transfer between the sand, fluidizing gas and biomass is

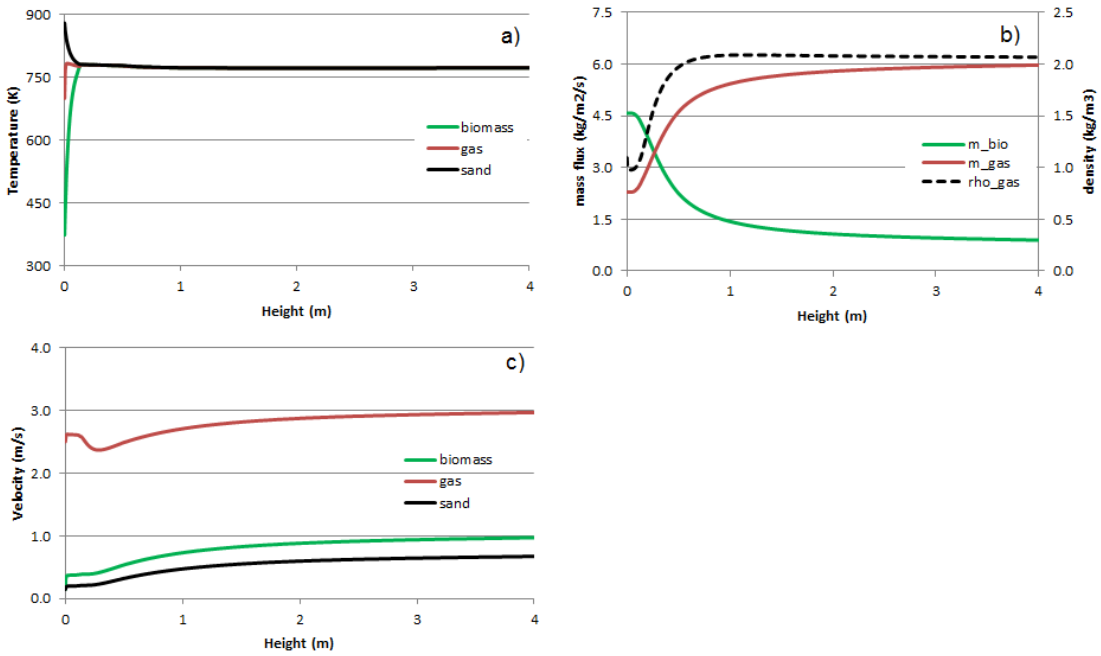

Figure 7.1: Biomass fast pyrolysis simulation results with pine feedstock, a) temperature profiles, b) mass flux and density profiles, c) velocity profiles

very fast and thermal equilibrium is reached near the reactor inlet. As biomass particles are heated up, pyrolysis reactions occur. As biomass is being consumed and pyrolysis vapors are produced, the mass flux of biomass (inclusive of char residue) decreases and the mass flux of gas increases from 2.3 kg/s-m^2 to 6.0 kg/s-m^2, as shown in Figure 7.1 b. The gas temperature increases due to heat transfer from the hot sand resulting in a sharp drop of gas density from 1.1 kg/m^3 down to 0.98 kg/m^3 at the reactor inlet. When pyrolysis vapors are produced, the gas density increases to 2.1 kg/m^3 due to the presence of higher molecular weight compounds produced in pyrolysis reactions. These phenomena affect the gas and particle velocity profiles, shown in Figure 7.1 c. At the reactor inlet, biomass and sand particles are accelerated by the drag force resulting from velocity difference between the solid and gas phase. The gas velocity typically decreases as momentum is transferred to solid particles. However, the simulation results show net gas acceleration at the reactor inlet. This is because of a relatively small mass flow rate of the fluidizing gas. At larger mass

flow rates, the drag force at the inlet is larger (due to a higher gas velocity). As a result, particles are accelerated to higher velocities and solid volume fraction change is larger, as continuity needs to be satisfied. Therefore, the increase in gas volume fraction more than offsets the effect of reduced gas density (due to increased gas temperature). However, in this case momentum loss due to drag is more than offset by the reduced gas density resulting in a net gas acceleration. The onset of pyrolysis reactions causes a decrease in gas velocity. This is because the effect of increased gas density and increased gas volume fraction (as biomass is consumed) initially more than offsets the effect of increased mass flux of the fluidizing gas due to pyrolysis reactions. Finally, the gas velocity increases when the increase in the mass flow rate of the gas starts to dominate. The particle velocity initially increases sharply due to intense momentum transfer by drag force. The initial increase is followed by a continuous increase at a slower rate due to increased density and mass flux of the fluidizing gas accompanied by a reduced mass flow rate of the solids.

In order to better understand the changes in mass flow rates along the reactor due to pyrolysis reactions, a comparison of the mass fraction profiles of organics, gas, solid residue, char, and water for pine, corn stover and switchgrass feedstocks for the base case simulation assumptions is shown in Figure 7.2. The reaction onset occurs close to the reactor inlet and full conversion is reached within 1 meter above the reactor inlet. There are no significant differences in an overall biomass pyrolysis rate due to the differences in chemical composition. The organics yield from corn stover is lower and the gas yield is higher compared with the other two feedstocks. Based on the analysis of the chemical composition information, the higher gas yield is due to the lower cellulose content and higher hemicellulose content compared with the other two feedstocks. Detailed information about product yields and oil composition is provided in Table 7.1. The product yields and oil composition from pine and switchgrass are nearly identical. The oil from corn stover contains less lignin derived compounds and sugar derived compounds, which is due to lower cellulose and lignin content.

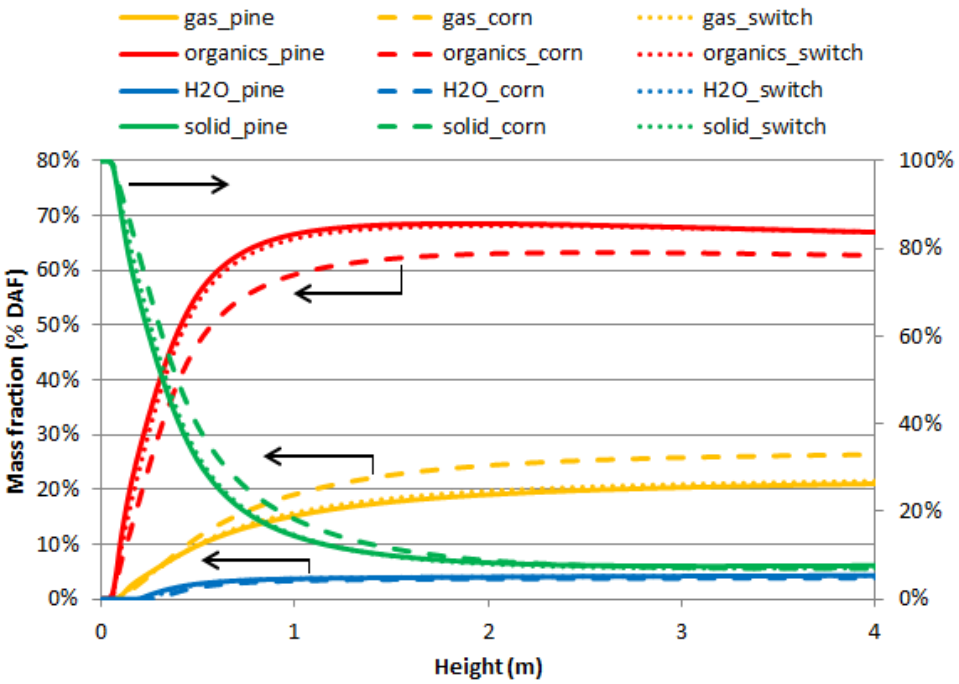

Figure 7.2: Comparison of the organics, solid residue, gas and water mass fraction profiles from pine, corn stover and switchgrass feedstocks

Table 7.1: Comparison of the product yields and oil composition from pine, corn stover and switchgrass

Yields (%wt DAF)	Pine	Corn Stover	Switchgrass
organics	67.0	62.7	67.0
gas	21.1	26.4	21.5
solid residue	7.7	7.0	7.1
water	4.3	3.9	4.3
Oil Composition			
water	8.7	13.4	11.2
acids	7.4	7.7	7.7
alcohols	5.6	7.1	5.5
aldehydes	24.2	24.8	24.6
sugar derived	23.9	21.9	24.3
lignin derived	30.3	25.2	26.8

The water content in the oil is higher because of slightly higher water content in the feedstock and higher water production in pyrolysis reactions. A comparison of the simulation results against experimental data is shown in Figure 7.3. The mass balance closure was 95.8%,

87.0% and 93.3% for experiments with pine, switchgrass and corn stover respectively. The char collection system malfunctioned in the switchgrass experiment, causing low char yield and low mass balance closure. A detailed oil composition analysis was not performed in the experimental study, therefore only a general comparison of oil, char and gas yields was possible. The results show that pyrolysis product predictions for pine are in good accordance with experimental data. However, the model overpredicts the oil yield and underpredicts the char yield from corn stover and switchgrass. This is because corn stover and switchgrass feedstocks have a much higher ash content compared with pine. Therefore, due to the presence of inorganic compounds which have catalytic properties and promote formation of char and gas, the experimental organics yields [29] are lower compared to the presented simulation results. For this reason, an experimental study described in the next chapter was performed

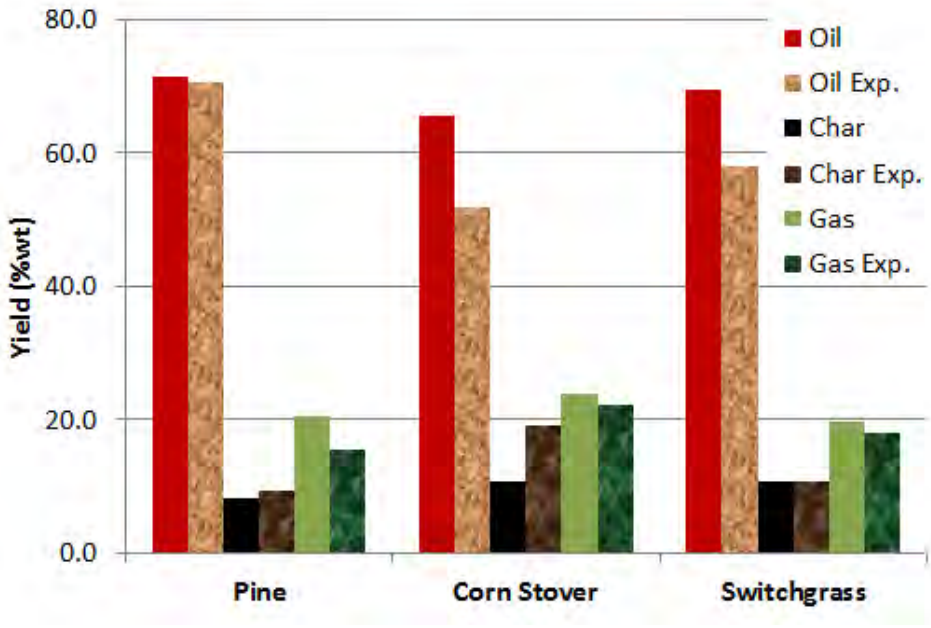

Figure 7.3: Comparison of experimental pyrolysis product yields from pine, switchgrass and corn stover to simulation results

in order to adjust the reaction mechanism in order to better match the actual oil yield and composition from different feedstocks and thus make the reactor model more flexible and robust. The remaining part of this chapter describes the effect of the fluidization parameters

investigated previously in the non-reactive simulations on biomass conversion and product yields.

7.2 Particle Size

Increasing the particle size results in a slower rate of average temperature increase, as shown in Figure 7.4. The thermal equilibrium is reached at approximately 0.15 m, 0.4 m and 1 m above the reactor inlet with 0.5 mm, 1 mm and 2 mm particle sizes respectively. The simulations were performed such that the outlet temperature was equal to 500^{o}C. Since

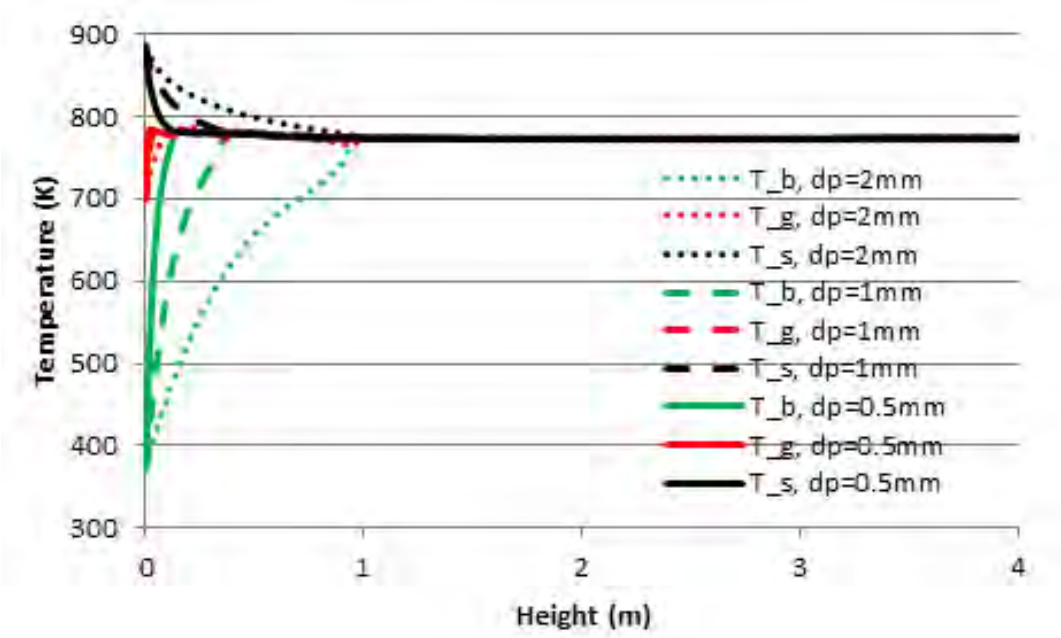

Figure 7.4: Comparison of biomass temperature (T_b), gas temperature (T_g), and sand temperature (T_s) along the reactor for particle size of 0.5 mm, 1mm and 2 mm

the mass flow rate of fluidizing gas needed to be adjusted to ensure entrainment of different particle size, the particle velocities and residence times of the gas, pyrolysis vapors and particles are not equal. The comparison of particle and gas velocities is shown in Figure 7.5. The entrainment of larger particles requires a higher drag force, therefore the inlet gas velocity is 2.5 m/s, 5.0 m/s and 8.8 m/s respectively in simulations with 0.5 mm, 1mm and

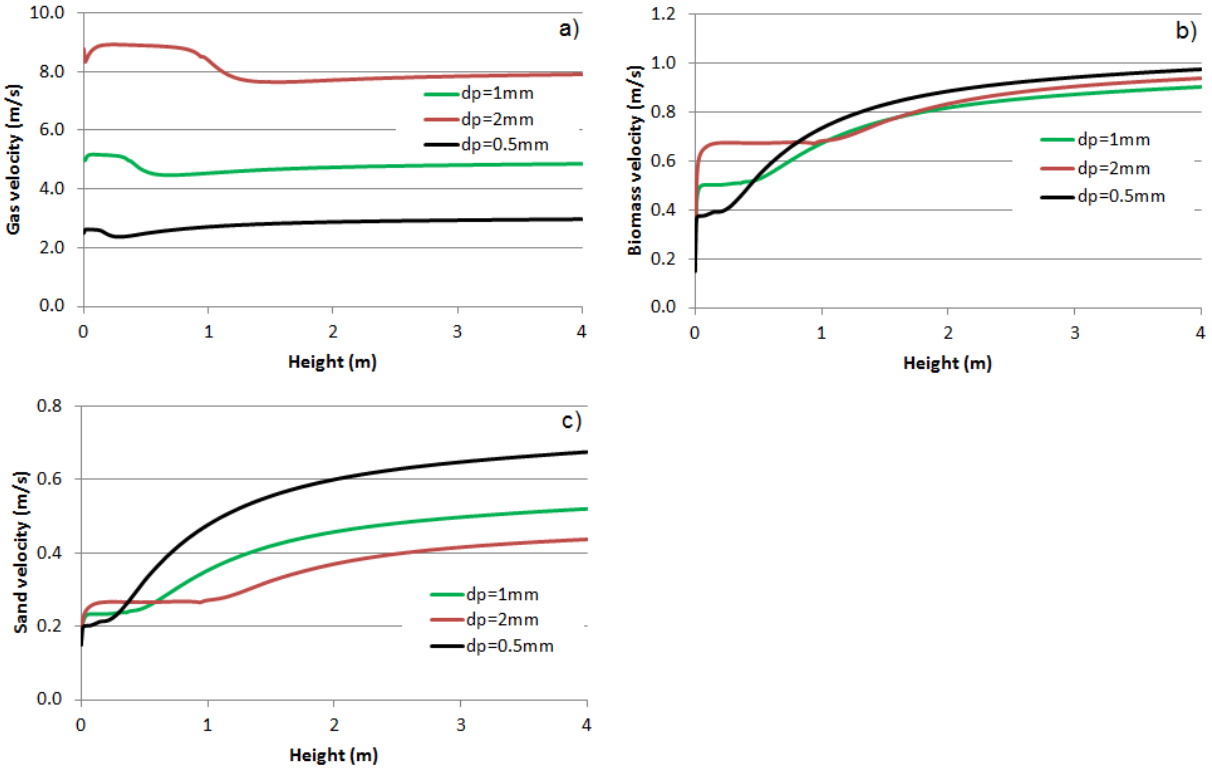

Figure 7.5: Comparison of velocity profiles along the reactor height with different particle sizes a) gas velocity, b) biomass particle velocity, c) sand particle velocity

2 mm particles. As previously mentioned, the gas velocity drops at the inlet and the particle velocity increases due to momentum exchange. As the particle velocity increases, the volume fraction of solids decreases due to conservation of mass. The conservation of mass is inclusive of reactions for the case of biomass, however, the reaction rates are initially slow as the biomass particle temperature is low. After the initial fluctuations, the velocities are stable as the drag and gravity forces reach equilibrium and the biomass particles are being heated up. When the pyrolysis reactions occur, there are several interrelated phenomena affecting the velocities. Firstly, the mass flowrate of biomass decreases and the mass flowrate of gas increases. The changes in mass flow rates directly affect the volume fractions of solids and gas. Moreover, the density of the fluidizing gas changes as high molecular compounds are present. The changes of gas properties affect the drag force. The combined effect of all the aforementioned factors results in the increase of biomass and sand particle velocities and a

decrease in gas velocity. The residence time of gas is approximately 1.4 sec, 0.8 sec, and 0.5 sec with 0.5 mm, 1 mm and 2 mm particles. The biomass and sand particle velocities are not equal. Although the biomass and sand particles are of the same size, biomass particles travel faster due to lower density, which results in a smaller gravity force to be offset by the drag force. Therefore, the biomass residence time is approximately 5 sec at all particle sizes compared to the sand residence time of 8 sec, 10 sec, and 12 sec for 0.5 mm, 1 mm and 2 mm particle size respectively. The general characteristics of the velocity profiles of both particle types are the same. This is because particles collide and exchange momentum with each other. However, the solid mass flux and volume fraction is relatively low, therefore the intensity of the particle-particle collisions is not sufficient to offset the difference in biomass and sand velocity due to the different drag force. For this reason, a so called particle separation exists and biomass and sand particles travel through the reactor at different average velocities. Particle separation means that particles of different sizes or properties are not well mixed but they tend to cluster together.

Particle size also affects the biomass conversion profile in the reactor as shown in Figure 7.6. The reactor height of 4 meters is sufficient for reaching full conversion at all the considered particle sizes according to the simulation results. Biomass is nearly fully converted within 1 meter above the reactor inlet at 0.5 mm particle size. The distance required for full conversion increases to 2.5 m at 2 mm particle size. The onset of the pyrolysis reactions is shifted away from the reactor inlet from 0.1 m to 1 m as the particle size increases from 0.5 mm to 2 mm. The reactor might seem oversized at first, however, it is important to keep a safety margin to account for variations in particle size, model errors in predicting the velocities, heat transfer rates or pyrolysis reaction rates. The comparison of mass fraction profiles shows that the increased particle size causes an offset of the pyrolysis process farther from the reactor inlet, however the final product yields and composition remain unchanged.

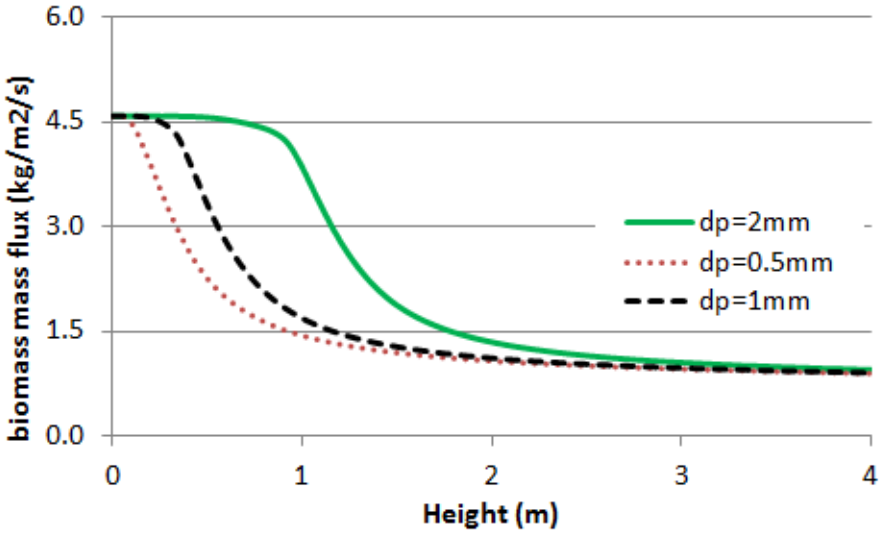

Figure 7.6: Biomass mass flux profiles along the reactor height for 0.5 mm, 1mm, and 2 mm biomass particle sizes

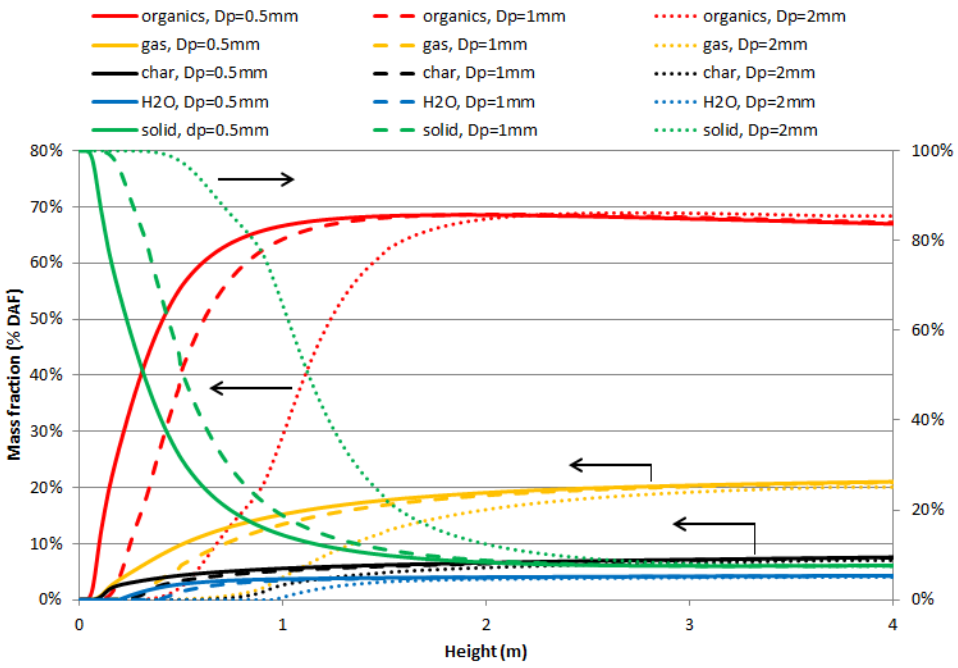

Figure 7.7: Comparison of organics, solid residue, gas, char and water mass fraction profiles along the reactor height for 0.5 mm, 1mm, and 2 mm biomass particle sizes

7.3 Heat Transfer Coefficient

The non-reactive simulations proved that the external heat transfer coefficient might possibly affect the pyrolysis reaction rates and conversion of larger biomass particles in the reactor. In order to further investigate this issue, reactive simulations were performed with the two different correlations for the Nusselt number with particle sizes of 0.5 mm and 2 mm. The comparison of the biomass mass flux illustrated in Figure 7.8 shows that the onset of pyrolysis reaction is shifted further from the reactor inlet as the external heat transfer rate is lower. The reaction onset is shifted from 0.1 m to 0.15 m above the reactor inlet for the 0.5 mm particle size and from approximately 1m to 2m above the reactor inlet for the 2 mm particles. Full conversion is still reached in the reactor and no significant changes in product yields and composition are observed. However, this example shows that the reactor is not oversized and operation with particles larger than 2 mm would require an increase of the reactor height.

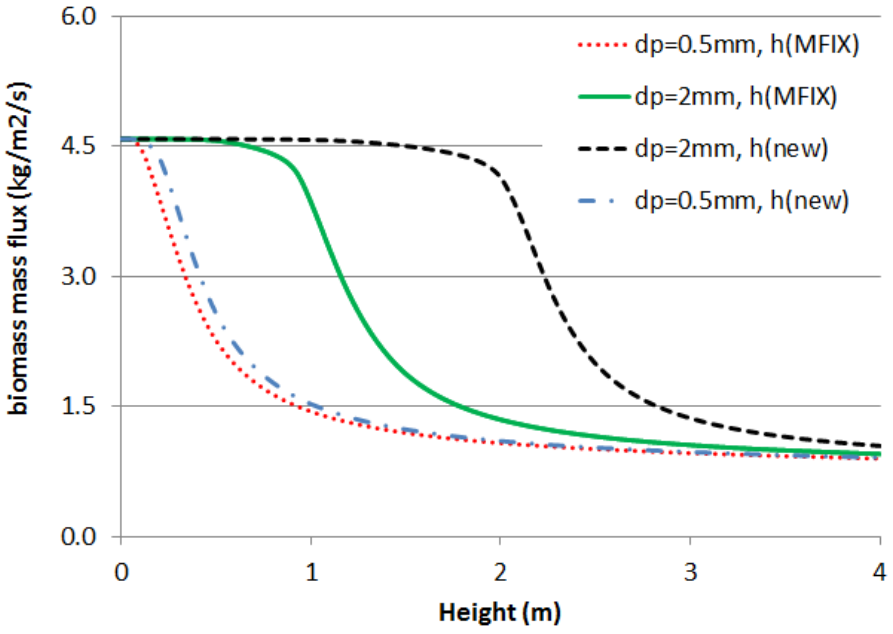

Figure 7.8: Comparison of mass fraction profiles along the reactor height for 0.5 mm, and 2 mm biomass particle sizes with different external heat transfer coefficients

7.4 Temperature and Pressure

It has been found that the optimal temperature for biomass fast pyrolysis was approximately 500^{o}C. However, it is possible that there will be temperature fluctuations during reactor operattion, therefore it was of interest to evaluate the effect of temperature on mass fraction profiles, product yields and composition. The simulations were performed for the following three temperatures: 480^{o}C, 500^{o}C and 520^{o}C with pine feedstock. The different reaction temperatures were achieved by adjusting the inlet temperature of the inert sand.

Simulation results show that the final gas density decreases with increased temperature from 2.2 kg/m^3 at 480^{o}C to 1.9 kg/m^3 at 520 ^{o}C. As a result of both reduced density and increased mass flowrate (due to higher gas yields at higher temperatures) the gas velocity increases from 2.8 kg/m^3 at 480^{o}C to 3.2 kg/m^3 at 520 ^{o}C. Higher gas velocity and viscosity results in higher particles velocities. The reaction rates are also higher at higher temperatures, which is illustrated in Figure 7.9 showing the biomass mass flowrate along the reactor height. Given the higher biomass particle velocities, the differences in the biomass mass flux profiles would be even larger when plotting them against time. The comparison of product yields and oil composition as a function of temperature is shown in Table 7.2. The

Table 7.2: Comparison of the product yields and oil composition from pine, corn stover and switchgrass

Yields (%wt DAF)	480^{o}C	500^{o}C	520^{o}C
organics	69.3	67.0	64.1
gas	19.4	21.1	22.6
solid residue	7.5	7.7	8.5
water	3.8	4.3	4.8
Oil Composition			
water	7.9	8.7	9.6
acids	6.5	7.4	8.3
alcohols	4.8	5.6	6.4
aldehydes	21.4	24.2	27.0
sugar derived	27.3	23.9	21.0
lignin derived	32.1	30.3	27.7

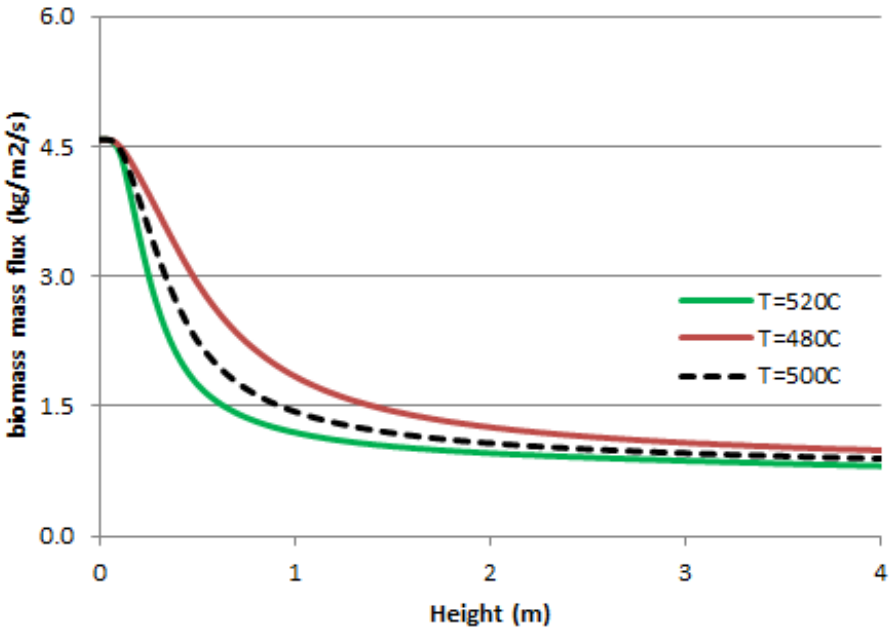

Figure 7.9: Comparison of biomass mass flux along the reactor height at reaction temperatures of 480^{o}C, 500^{o}C and 520^{o}C

organics yield decreases with the temperature increase from 69.3 % at 480^{o}C to 64.1 % at 520^{o}C. The reduced yield of organics is accompanied by the increased yield of gas, char and water. In addition, the oil composition changes. The amount of sugar derived compounds decreases from 27.3% at 480^{o}C to 21.0 % at 520^{o}C. The amount of high molecular weight, lignin derived compounds also decreases from 32.1% at 480^{o}C to 27.7 % at 520^{o}C, as they are decomposed to gas, char and water at higher temperatures. Moreover, the amount of aldehydes, acids and water increases, which results in a decreased pH of the produced oil and reduced heating value. The simulation results lead to the conclusion that the reactor performance with pine feedstock is better at 480^{o}C compared with commonly reported in the literature temperature of 500^{o}C.

Pressurization of the fluidizing gas affects the velocity profiles along the reactor height, as shown in Figure 7.10. For the same reactor size, higher gas density (or lower specific volume) requires a higher mass flowrate of the gas in order to provide a sufficient velocity for drag

force required for maintaining the fast fluidization. However, a smaller reactor volume can also increase gas velocities at the higher pressures. This opens the option of possibly reducing capital costs by reducing reactor volumes, provided there are no significant changes in metallurgical, material and fabrication requirements because of the higher pressures. Since the evaluated reactor is a small scale reactor, volume reduction (although recommended for industrial applications) is not considered in this study for consistency. With the higher initial gas density and higher mass flow rate, the effect of pyrolysis reactions and related change in gas density and mass flow rate is less pronounced than in the base case. Therefore, the changes in particle velocities are relatively small. The effect of increased fluidizing gas pressure on heat transfer and volume fractions is negligible.

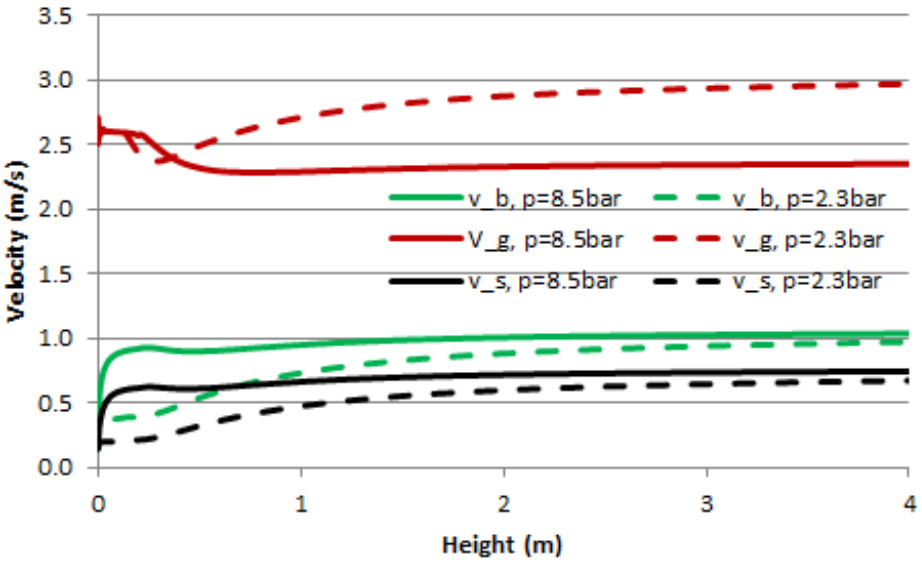

Figure 7.10: Comparison of the gas and particle velocity profiles along the reactor at the fluidizing gas pressures of 2.3 bar and 8.5 bar

7.5 Sand-to-Biomass Ratio

Changes of sand-to-biomass ratio were found not to cause any significant changes in heat transfer rates, velocity profiles or mass fraction profiles. The Figures showing the comparison

of the results were provided in Appendix C for completeness.

7.6 Gas-to-Biomass Ratio

Decreasing the gas-to-biomass ratio results in lower particle and gas velocity magnitudes and higher residence times and solid volume fractions in the reactor. As shown in Figure

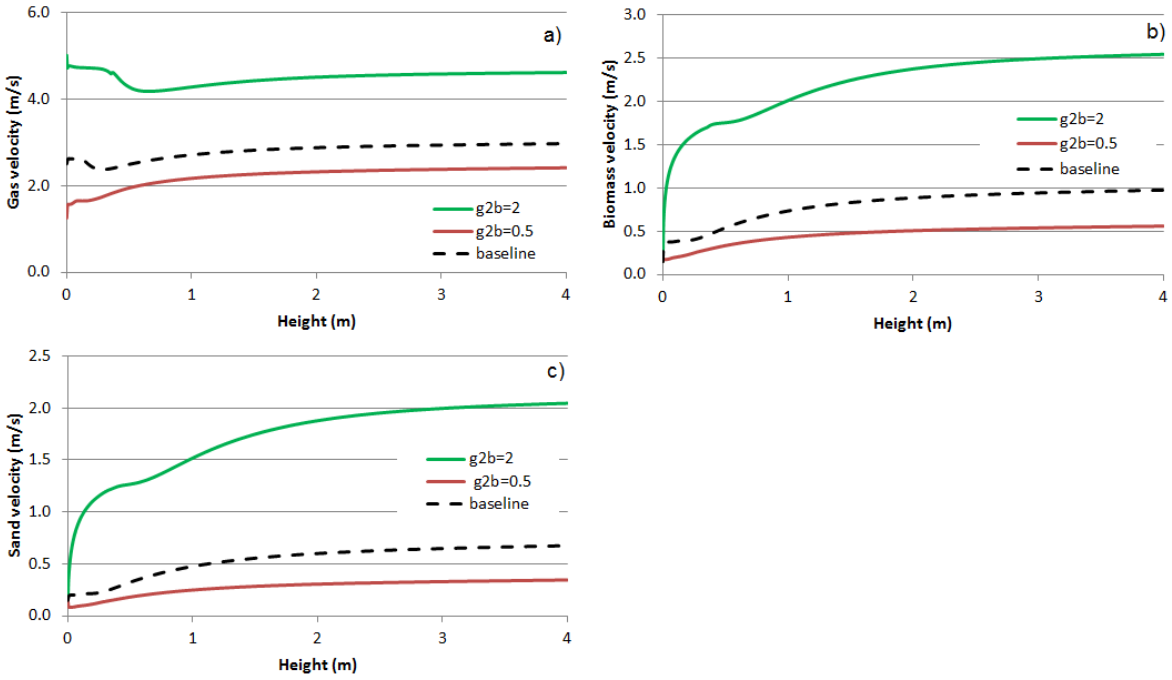

Figure 7.11: The effect of fluidizing gas mass flow rate on velocity profiles a) gas velocity, b) biomass velocity, c) sand velocity

7.11, increasing the fluidizing gas mass flow rate results in a higher inlet gas velocity. The increased drag force results in a higher particle velocity and shorter residence times. Biomass residence time is 9.3 s, 5.3 s, 1.9 s at the R_{gb} of 0.25, 0.5 and 1 respectively. Gas residence time is 1.8 s, 1.4 s, 0.9 s at the R_{gb} of 0.25, 0.5 and 1 respectively. As a result of higher particle velocities, the offset of pyrolysis reactions occurs farther from the reactor inlet, as shown in Figure 7.12. Full biomass conversion is still achieved in the reactor. The comparison of the organics, solid residue, gas, char and water mass fraction profiles is provided in Appendix

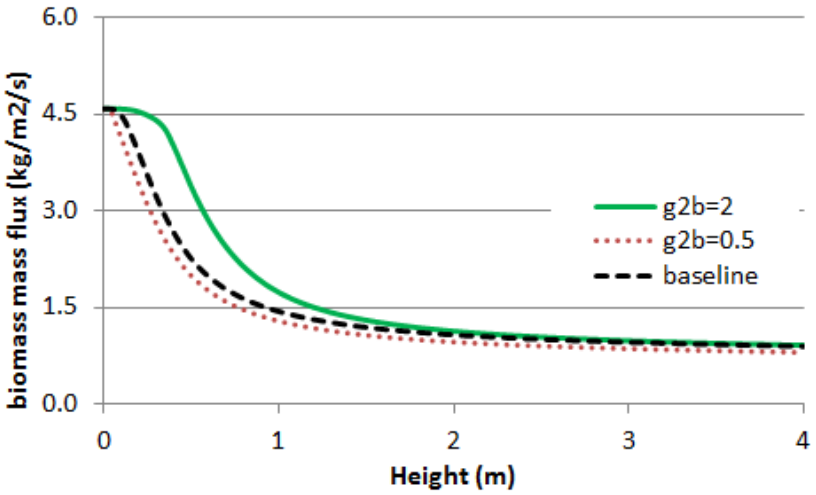

Figure 7.12: Biomass mass flux profiles along the reactor height at the fluidizing gas-to-biomass ratio (R_{gb}) of 0.25, 0.5, and 1

C. Despite the shorter residence time at higher gas mass flow rate, the final product yields and composition remain unchanged.

7.7 Hydrogen Addition

The addition of hydrogen to the fluidizing gas strongly affects the density and viscosity of the fluidizing gas and therefore has a strong influence on velocity profiles. Hydrogen addition was considered for two pressure levels (2.3 bar and 8.5 bar) as it was previously done for the non-reactive simulations. Since the changes in pyrolysis reaction pathways due to the presence of hydrogen are not well understood, hydrogen was treated as inert gas in this study. As illustrated in Figure 7.13, the inlet velocity of the hydrogen rich gas is approximately 6.5 m/s, which is higher than 3.8 m/s in the base case simulation. This causes a large acceleration of the particles at the reactor inlet, which is followed by the deceleration as the drag force becomes insufficient to maintain the high particle velocity. However, as pyrolysis reactions occur, the drag force increases due to increased gas mass flow rate and gas density. As a consequence, particles are again accelerated. Velocity profiles show the same general characteristics at both 2.3 bar and 8.5 bar pressure. Temperature profiles and

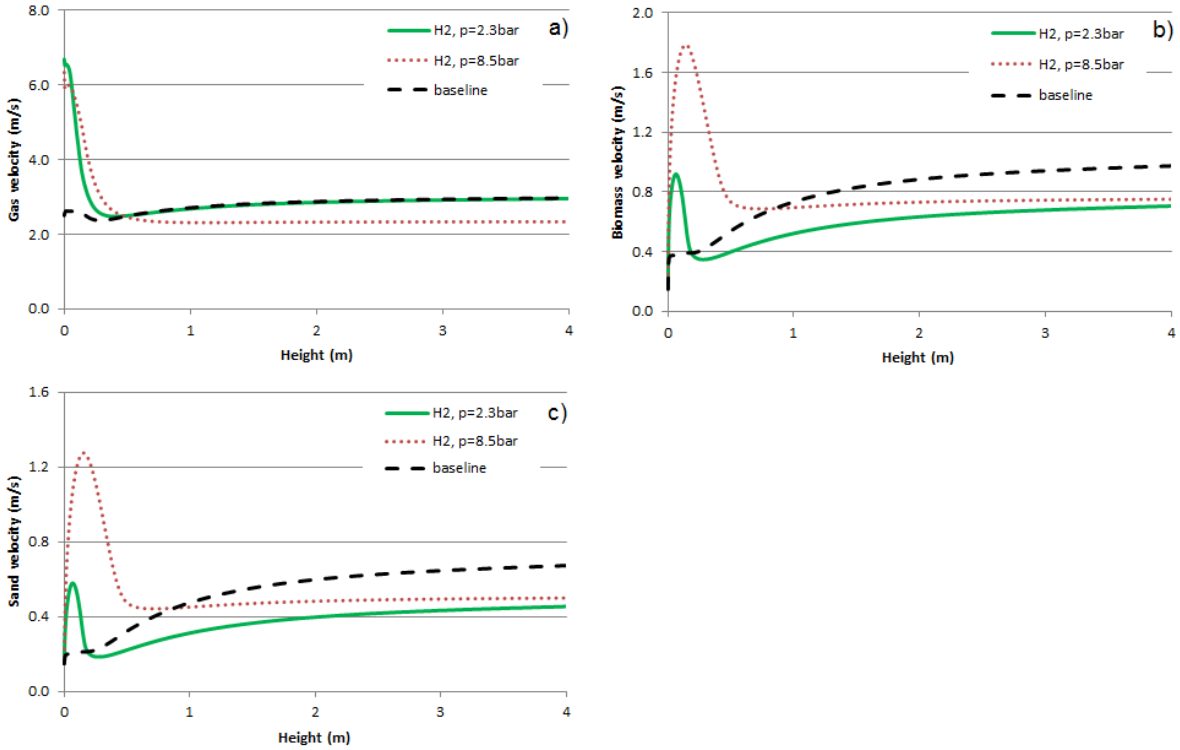

Figure 7.13: The effect of hydrogen addition on velocity profiles a) gas velocity, b) biomass velocity, c) sand velocity

mass fraction profiles do not show any significant differences compared to the baseline results due to hydrogen addition. However, the sand inlet temperature needs to be increased by 15 K compared to the base case due to the increased heat capacity of fluidizing gas. Operation at elevated pressure (8.5 bar) requires an increase of the sand inlet temperature of 55K due to both increased gas mass flow rate and increased gas heat capacity.

7.8 Conclusions

Biomass fast pyrolysis simulations with the developed reactor model show that the 1-D model provides information about the temperature and velocity profiles, pyrolysis reactions and rates of formation of individual product classes along the reactor height, which is useful for determining the reactor height required for high biomass conversion and low vapor resi-

dence time. Moreover, this information is important for better understanding the pyrolysis process and tuning the operating parameters for maximizing the yields of desired products.

The parametric sweep results show that the two most influential parameters for product yields and composition are the reaction temperature and biomass composition. Operating at higher temperature resulted in a reduced oil yield and adverse changes in the oil composition. The mass fractions of water, acids and aldehydes were higher and the mass fraction of sugar derived compounds was lower when the pyrolysis reaction temperature was higher. Therefore, the model could be applied to optimizing pyrolysis reaction temperature for specific feedstocks. The employed reaction model gives good predictions of product classes for the low ash content feedstocks such as pine, however it significantly overpredicts the organics yields from high ash content feedstocks. This is because the catalytic effect of intrinsic contaminants is not included in the reactions. Therefore, the reaction mechanism should be corrected in order to improve the predictive capabilities of the model from feedstocks with high ash content.

Changing the remaining operating parameters (besides reaction temperature and biomass feedstock) causes changes in velocity profiles, temperature profiles reaction onset and reaction rates. However, the final product yields at the reactor outlet remain unchanged provided that the residence time is sufficient for full conversion. This result will most likely change when a validated secondary reaction mechanism is available for integration with the model. The oil yield and composition will become dependent on the vapor residence time in the reactor and the developed model will become a useful tool for optimizing the operating conditions and reactor design for maximizing the oil yield and obtaining the most desirable oil composition.

CHAPTER 8

EFFECT OF POTASSIUM ON BIOMASS FAST PYROLYSIS PRODUCT YIELDS

As shown in the previous chapter, the state-of-the-art biomass pyrolysis reaction mechanism does not capture the effect of inorganic compounds present in the biomass feedstocks on the pyrolysis products, which leads to significant overprediction of the oil yield from biomass feedstock with higher ash content such as corn stover or switchgrass. Therefore, there is a need to develop an experimental procedure and a data analysis methodology that will allow evaluation of the changes in kinetic parameters and adjustment of the reaction mechanism. The goal of the experimental work performed within this thesis is to initiate this process by evaluating of the effect of potassium on cellulose pyrolysis kinetics and incorporating the results into the cellulose pyrolysis reaction mechanism [87]. Cellulose was chosen as a starting point due to lower complexity of its chemical structure compared to hemicellulose and lignin. The remaining biomass building blocks (hemicellulose and lignin) could potentially also be affected by the presence of inorganic compounds, however they are not the subject of the experimental study. This is because the goal of the study is to investigate whether the proposed methodology is appropriate for this application. Therefore, eliminating the additional complexity is desired and performing an extensive study is not recommended as the research is at the very early stage. Potassium was chosen as the first engineering approximation for all alkali metals due to its strong influence on levoglucosan and hydroxyacetaldehyde formation [31, 33], and its relatively large mass fraction in the biomass structure compared to other metals. The detailed ash composition from the three considered biomass feedstocks (pine, corn stover and switchgrass is provided in Table 8.1. This chapter explores the changes in cellulose fast pyrolysis reaction kinetics (reaction order, rate constants, activation energy) and product yields by analyzing the experimental data collected with a molecular beam mass spectrometer (MBMS) using statistical tools (principal component analysis and multivariate

Table 8.1: Elemental analysis of ash obtained from pine, corn stover and switchgrass at NREL

Elemental Analysis	Pine	Corn Stover	Switchgrass
Ash (wt% biomass)	0.71	4.27	4.20
SiO_2 (wt% ash)	45.62	50.73	54.07
Al_2O_3 (wt% ash)	5.14	0.28	0.26
TiO_2 (wt% ash)	0.29	0.01	0.02
Fe_2O_3 (wt% ash)	5.68	1.20	1.79
CaO (wt% ash)	18.06	9.29	7.54
MgO (wt% ash)	6.03	6.26	9.97
Na_2O (wt% ash)	0.94	0.08	1.59
K_2O (wt% ash)	12.50	26.53	17.12
P_2O_5 (wt% ash)	2.34	2.98	4.44
SO_3 (wt% ash)	2.33	2.28	2.71
MnO (wt% ash)	1.20	0.10	0.20
Ash Closure	100.1	99.7	99.7

curve resolution) [39]. The results are incorporated into an existing reaction mechanism [87] and validated with experimental data [88] from a fluidized-bed reactor at the National Renewable Energy Laboratory (NREL).

8.1 Experimental Methods

Experiments were performed with microcrystalline cellulose (Avicel) purchased from Sigma Aldrich and cellulose treated with different levels of potassium as K_2CO_3 (between 0.01 wt% and 1 wt%). Cellulose samples were prepared by impregnating pure cellulose with aqueous solutions of potassium carbonate. The created slurry was then dried in air at room temperature. The sample weight was 4 mg, which was a minimum weight required for the equipment to obtain an acceptable signal-to-noise ratio. Samples were pyrolyzed at five temperatures: 480^{o}C, 490^{o}C, 500^{o}C, 510^{o}C and 520^{o}C in order to build a database for evaluating the reaction rate constant. The experiments were performed in a Frontier Laboratories 2020iD pyrolyzer (Fukushima, Japan) with an autosampler connected to the MBMS device, shown in Figure 8.1. The samples were placed in 80 ml stainless steel cups and pyrolyzed at a cycle time of 90 s. The pyrolysis reactions were completed in less than 30 s in the considered

temperature range. The vapors were swept with helium gas in order to ensure an inert environment for pyrolysis processes. A small sample of the product stream was extracted by the MBMS device through an orifice, where a nearly isentropic expansion occurred. The rapid cooling of the product stream due to expansion helps to eliminate the secondary cracking reactions. Next, the gases and vapors passed through a three-stage vacuum system (p =13 Pa, 0.1 Pa and 10^{-4} Pa), where they were accelerated. The supersonic molecular beam was then ionized with a low-energy (17.0 eV) electron beam. The ions were quantified with an electron multiplier detector. The pyrolysis vapors mass spectra were recorded with an Extrel

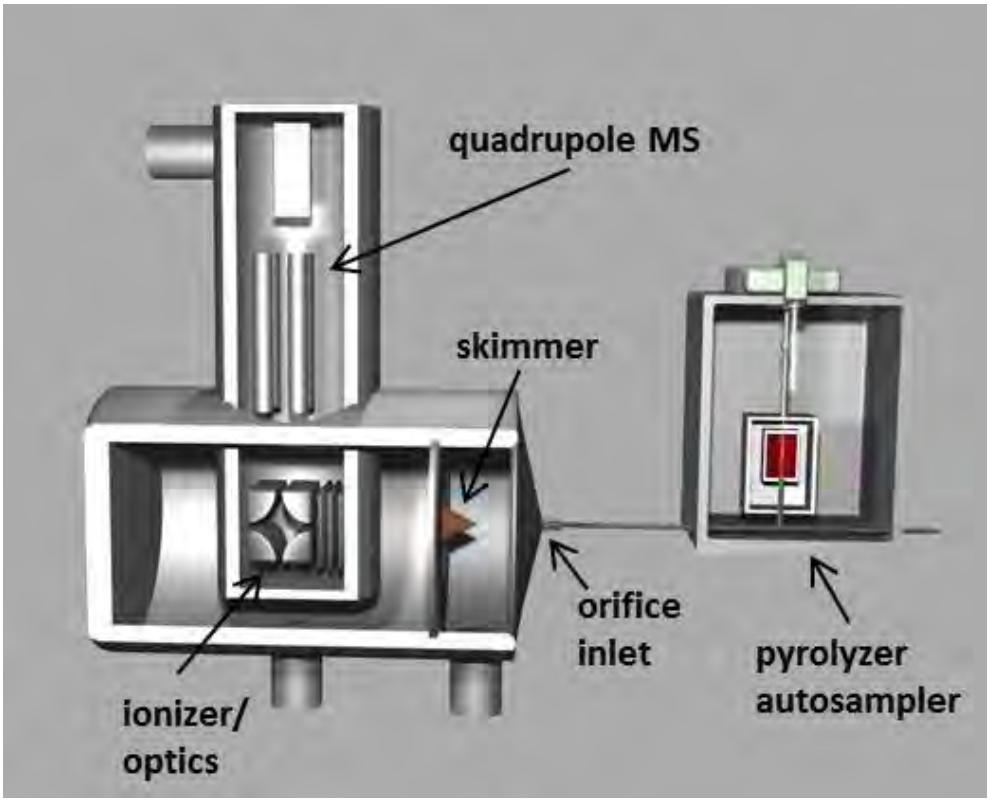

Figure 8.1: Experimental set-up schematic showing a pyrolyzer with the autosampler connected to the MBMS

mass spectrometer at a frequency of 0.5 s^{-1}. Each sample was analyzed in replicate. The MBMS was chosen for the experiments due to the following advantages: i) collisionless flow, ii) preserved reactive species (low temperature), iii) ability to record time-resolved processes, and iv) quick data collection. However, MBMS data analysis can be challenging due to the

uncertainty about the parent compounds of the detected fragment ions. Other factors which might influence the MBMS data are the electron energy, quadrupole tuning, and so called "mass separation" [39].

The experimental data from a fluidized bed reactor at NREL [88] were used for the purpose of validation of the modified cellulose pyrolysis mechanism. The reactor system is presented in Figure 8.2. Biomass was supplied to the reactor through a feed hopper with a screw conveyor. Nitrogen gas was added in the feed system for pneumatic transport of biomass. Additional 5 SLM of nitrogen were supplied to the reactor to ensure proper fluidization. The fluidized bed material was olivine with particle size of 0.5 mm and a reactor

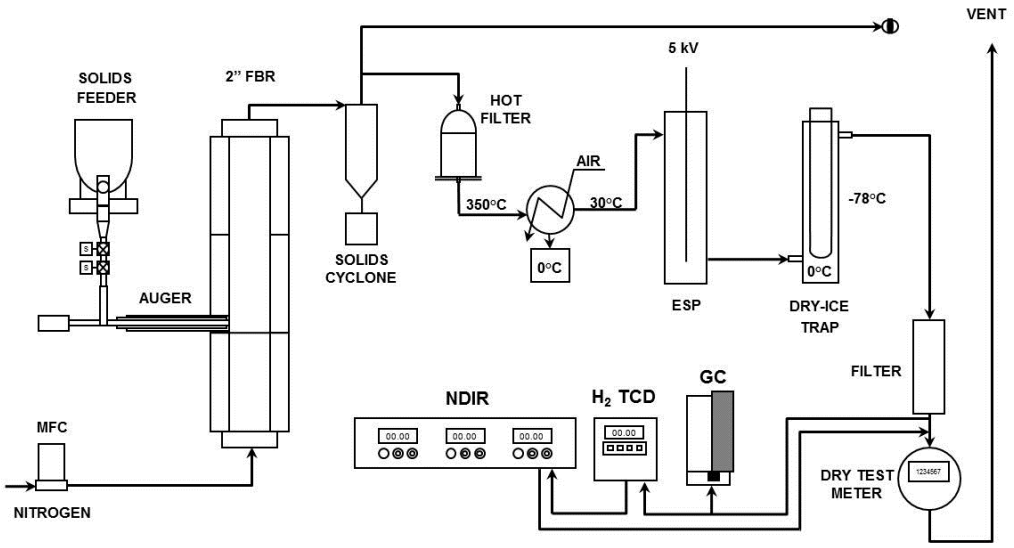

Figure 8.2: Schematic of an experimental fluidized bed reactor system at NREL

inventory of 400 g. Pyrolysis experiments were performed at 500^{o}C with the residence time of 0.5 s. Pyrolysis products were directed to a cyclone followed by a 2μm hot filter, where the char was separated from the pyrolysis gases and vapors. The reactor was equipped with a two-step oil collection system. The first step was an electrostatic precipitator (ESP), where many lignin pyrolysis products and aerosols were removed from the pyrolysis vapors. This

is because lignin products have higher molecular weights and higher condensation temperatures. Pyrolysis vapors were cooled before the ESP to approximately 30^oC in an air-cooled heat exchanger. Therefore, the ESP was also a primary condenser. The second condensation step was a dry ice condenser, which was the final liquid collection step. In order to improve mass balance closure (to $> 90\%$), the amount of liquid collected in different condensation steps was determined by weighing the entire condenser unit before and after the experiment.

8.2 Data Analysis Methodology

The recorded MBMS data presented in Figure 8.3 include the total ion current (TIC) and the respective mass spectra. TIC is the sum of all ions detected during the experiment and it provides the information about the onset, progression and completion of the pyrolysis process. The mass spectra show the relative contribution of individual fragment ions to the TIC at each time step, thus providing the information about product composition. The units of intensity have no direct physical meaning.

The collected MBMS data were preprocessed in MS Excel for further analysis in the UnscramblerX [89]. The preprocessing included normalizing the data with the highest intensity in the dataset and scaling by a factor of 1,000 in order to increase the numerical values for statistical calculations. Only masses between m/z=30-200 were considered for further analysis as the higher molecular weights accounted for a relatively low percentage of the product mass ($\leq 2\%$). A principal component analysis (PCA) was performed on the preprocessed data in order to reduce the dimensionality of the dataset and describe the statistically significant trends with a small number of lumped product classes representative of major pyrolysis products, as determined by the principal components. The mathematical basics of principal component analysis is illustrated in Figure 8.4. The first step is to calculate the covariance matrix which shows the correlations between variables. Next, eigenvectors and eigenvalues are calculated. The eigenvectors provide information about the correlation between samples and the eigenvalues describe the strength of the correlations. For large

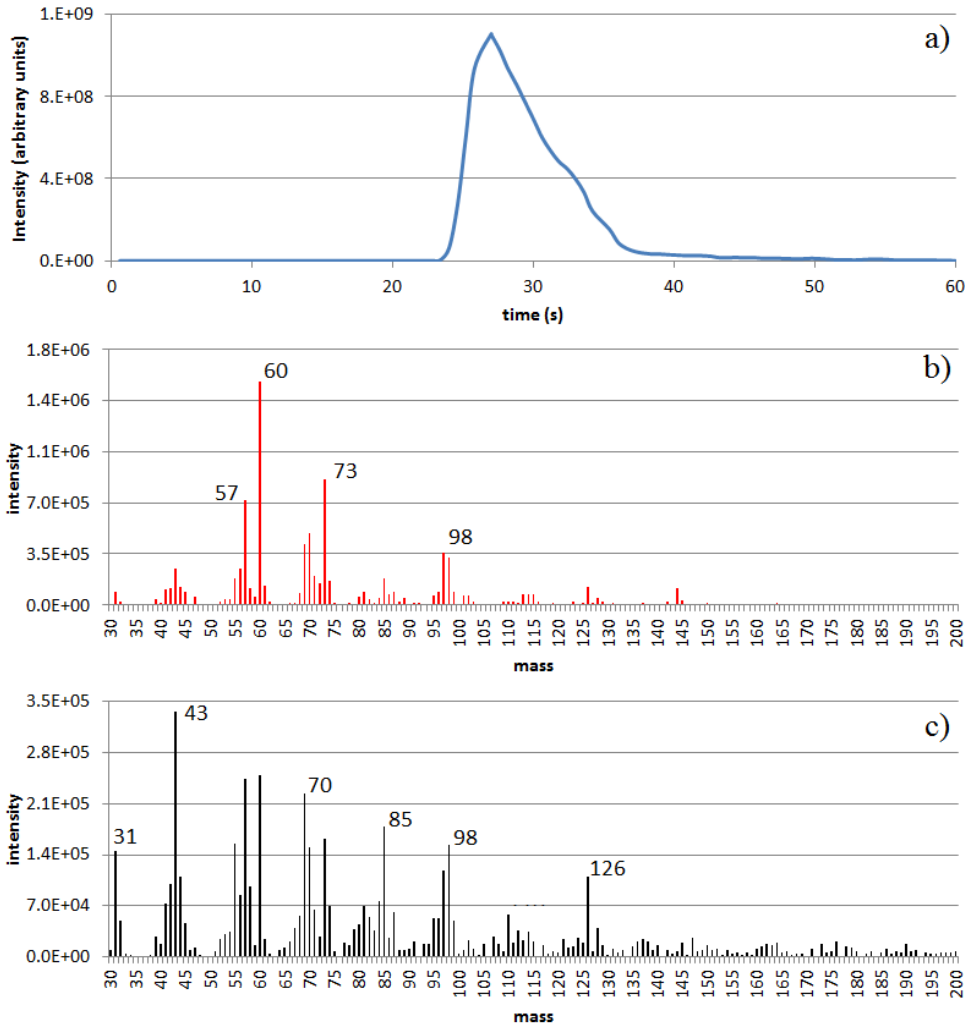

Figure 8.3: Recorded MBMS data a) total ion current (TIC) b) mass spectra of cellulose pyrolysis products, c) mass spectra of pyrolysis products of cellulose treated with 1 wt% potassium at 510°C

databases, keeping only the largest eigenvectors in the analysis offers dimensions reduction while still maintaining most information about the variance. The dataset is then transformed with the eigenvectors. The principal component analysis can be understood as looking at an object (dataset) from different angles in order to expose the features of interest (distinguish principal components). The dataset is therefore projected on a new set of orthogonal axes so that the variance explained is maximized by the fewest number of principal components. The results are then displayed with a score plot and a loading plot. A score plot shows the

calculated values of principal components for the samples and loadings typically show the grouping of clusters of samples. A loading plot shows the relative contribution of individual mass variance to each principal component. Next, the multivariate curve resolution (MCR)

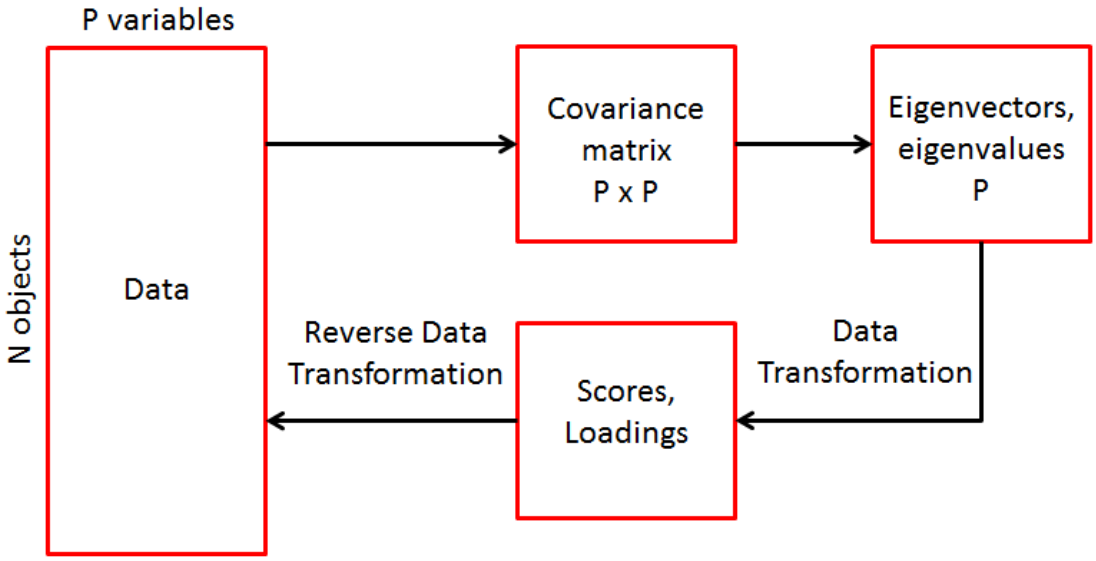

Figure 8.4: Schematic of Principal Component Analysis Methodology.

(described in detail in [90]) was used to deconvolute the time-resolved data into evolving concentration score profiles of principal components. These concentration profiles were subjected to kinetic tests to determine reaction rate constants and reaction orders. The data were subjected to zeroth order, first order and a fractional order (n) kinetic tests by performing a linear fit of the following functions plotted against time:

$$f_0(t) = \frac{\int_0^t c_{PC}(t)dt}{c_o} \tag{8.1}$$

$$f_1(t) = ln(\frac{\int_0^t c_{PC}(t)dt}{c_o}) \tag{8.2}$$

$$f_n(t) = \frac{1}{1-n} \cdot (\frac{\int_0^t c_{PC}(t)dt}{c_o})^{1-n} \tag{8.3}$$

where $f_0(t)$, $f_1(t)$, $f_n(t)$ is the zero order, first order and n-th order kinetic test function respectively, t is time, c_{PC} is the concentration score of a principal component, and c_o is the total amount of products, so that the non-dimensional concentration score changes between zero and one. The slope of the linear fit is equal to the reaction rate constant. The initial and final data were excluded from the kinetic analysis as they were likely affected by heat transfer limitations. The kinetic tests were performed for each component (PC1 and PC2) at each level of potassium treatment (0%wt, 0.01 %wt, 0.05 %wt, 0.1 %wt, 0.5 %wt, 1 %wt) and at each of the considered temperatures (480^{o}C, 490^{o}C, 500^{o}C, 510^{o}C, 520^{o}C). The size of created database and number of figures is preventive of including all the results, however in order to better explain the methodology an example linear fit for a first order kinetic test is shown in Figure 8.5. The rate constants for principal components PC1 and PC2

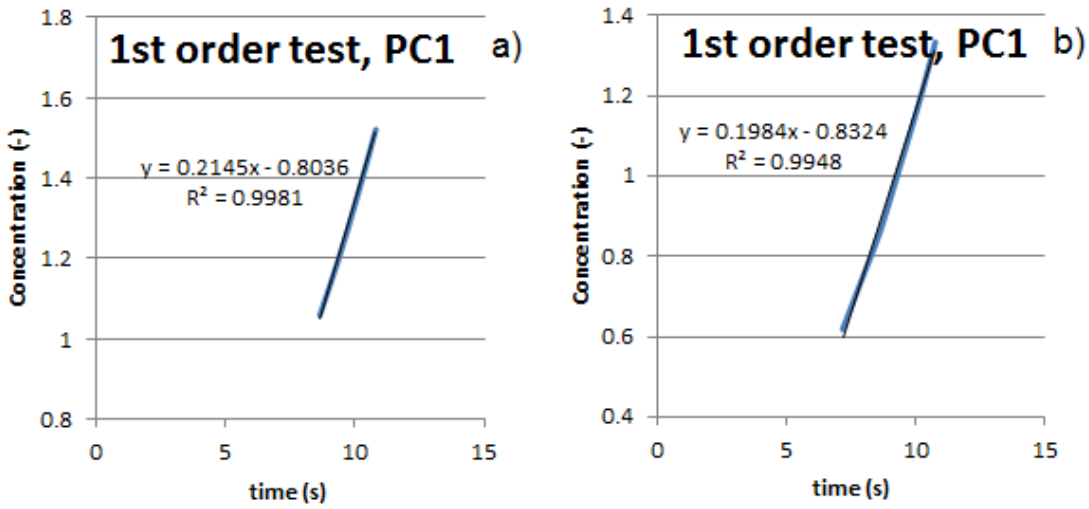

Figure 8.5: Sample results of a first order kinetic test for a) pure cellulose, b) 0.5 %wt potassium treatment at 510^{o}C.

were determined by reading the slope of the linear fit at each level of potassium treatment and at each temperature. The rate constants (for both PC1 and PC2) for each level of potassium treatment were next subjected to Arrhenius test. A sample Arrhenius test is shown in Figure 8.6. A plot of natural logarithm of the rate constant (k) vs. inverse of the temperature in Kelvin (1000/T) was made for PC1 and PC2 for all the levels of potassium

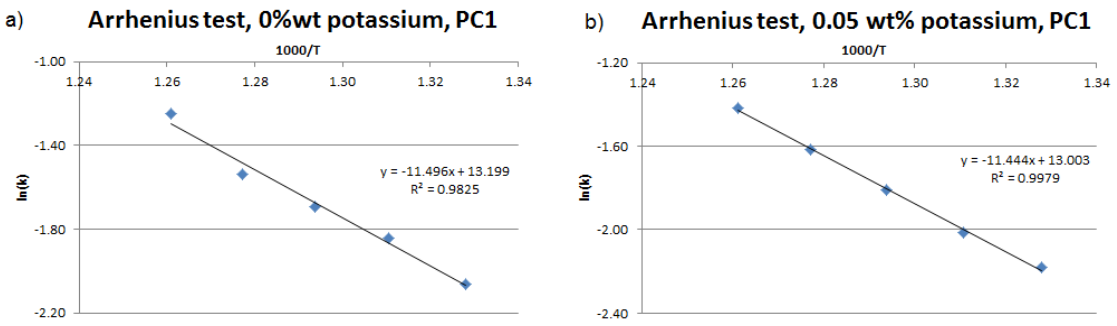

Figure 8.6: Sample results of an Arrhenius test for a) pure cellulose, b) 0.5 %wt potassium treatment.

treatment. The activation energy (E_a) was determined from the slope of the linear fit. The obtained activation enegies were next plotted vs. the level of potassium treatment and the fitted with power functions which are provided in the results section.

8.3 Results and Discussion

The recorded mass spectra show that pure cellulose gives high yields of levoglucosan (m/z=162) represented by characteristic fragment ions m/z=57, 60, 70, 73, 98 and 144, as illustrated in Figure 8.3 (b). The presence of potassium causes an increased intensity of fragment ions m/z=31, 32 characteristic of hydroxyacetaldehyde, m/z=85, 97, 126 representing 5-hydroxymethyl furfural, m/z =85, and m/z=43 (C_2H_2O), which could be assigned to acetyl compounds, as shown in Figure 8.3 (c). The relative intensity of anhydrosugars decreases with the increased potassium treatment. The general characteristics of these mass spectra are in accordance with previous studies [39, 91]. Therefore it is suspected that potassium is either inhibiting the formation of levoglucosan or catalyzing the formation of other products. The major characteristic fragment ions in the mass spectra and their possible sources are summarized in Table 8.2.

PCA analysis performed on the collected MBMS data in the UnscramblerX software distinguishes the aforementioned product groups, which are represented by two principal components PC1 and PC2. The two component model explains 98 % of the variance in the dataset

Table 8.2: Major characteristic fragment ions in cellulose pyrolysis product mass spectra and their possible sources

Ion (m/z)	Chemical Formula	Possible Source
31	CH_3O	hydroxyacetaldehyde
32	CH_4O	hydroxyacetaldehyde
43	C_2H_3O	acetyl
57	C_2HO_2, C_3H_5O	levoglucosan
60	$C_2H_4O_2$	levoglucosan, acetic acid, hydroxyacetaldehyde
70	C_4H_6O	levoglucosan
73	$C_3H_5O_2$	levoglucosan
85	$C_4H_5O_2$	5-hydroxymethylfurfural, pentosan
97	$C_5H_4O_2$	5-hydroxymethylfurfural
98	$C_5H_6O_2$	levoglucosan, furfuryl alcohol
110	$C_6H_6O_2$	5-hydroxymethylfurfural, catechol, resorcinol
126	$C_6H_6O_3$	5-hydroxymethylfurfural, trihydroxybenzene, levoglucosenone
144	$C_6H_8O_3$	levoglucosan

and it is determined by the UscramblerX as an optimal model for describing the dataset. Mass spectra of the two principal components, shown in Figure 8.7, indicate that PC1 represents sugar derived compound class and PC2 represents fragmentation products promoted by potassium carbonate (hydroxyacetaldehyde, acetyl compounds and 5-hydroxymethyl furfural).

MCR results provide the information about the changes in time resolved concentration score profiles of the two principal components (PC1 and PC2) in response to an increased amount of potassium in the sample. As shown in Figure 8.8 (a), the concentration of anhydrosugars is much higher than the concentration of the other products during the pyrolysis of untreated cellulose. Figure 8.8 (c) shows that the concentration of the anhydrosugars and other products are nearly equal at 0.5 wt% of potassium treatment, and Figure 8.8 (d) shows that there is significantly less anhydrosugars produced relative to other products

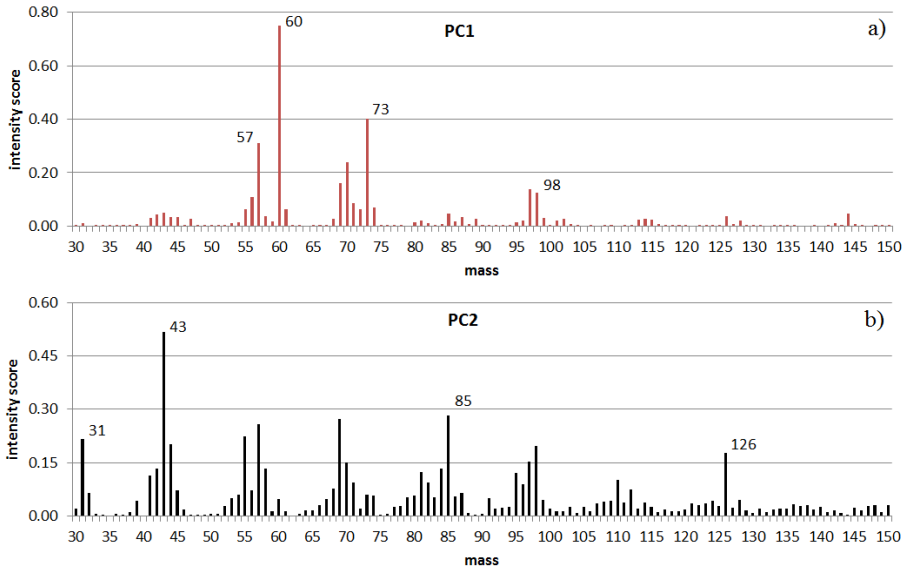

Figure 8.7: Mass spectra of principal components a) PC1, b) PC2

at 1 wt% potassium treatment. In addition, the total yield of pyrolysis vapors decreases, which results in a decreased TIC. The scale in Figure 8.8 (c) and (d) was adjusted for the decreased concentration score. The presented results were obtained at 510^{o}C, however, this trend was consistent at all considered temperatures. The Figures showing the concentration score profiles at the remaining temperatures are provided in Appendix D. The numerical values of the concentration scores have no direct physical meaning. However, their relative changes in response to increased potassium treatment provide valuable information about changes in product composition.

The kinetic tests performed on the concentration score profiles of the two principal components PC1 and PC2 reveal that the reaction order is not affected by the presence of alkali metals, and all reactions are best represented by first order. This also indicates that the data used were free from heat transfer limitations. The activation energies for the formation of the principal components PC1 and PC2 determined from kinetic tests are shown in Figure 8.9. The addition of potassium strongly inhibits the formation of levoglucosan, which manifests itself in an increased activation energy of PC1. The activation energy for the formation of

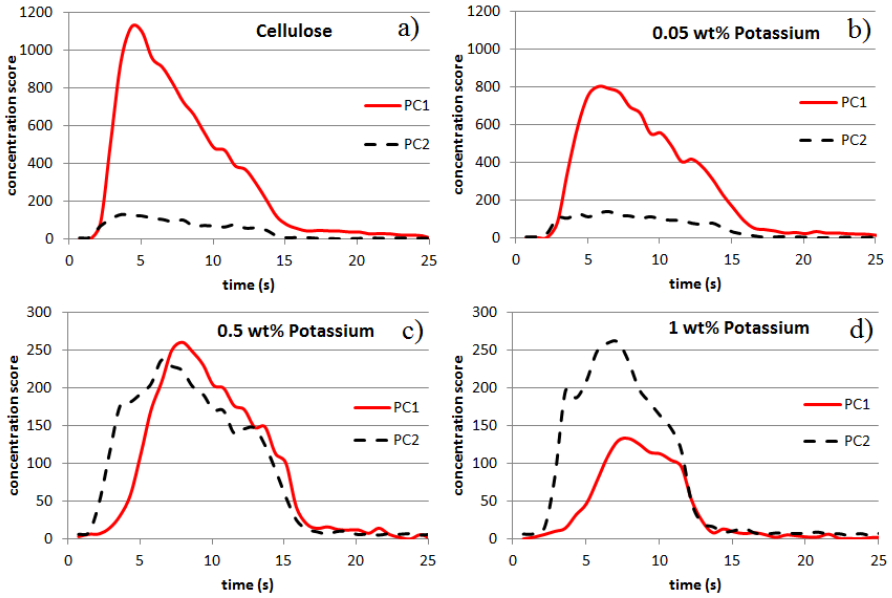

Figure 8.8: Concentration profiles of principal components PC1 and PC2 at 510°C a) pure cellulose, b) 0.05wt% potassium treatment, c) 0.5wt% potassium treatment, d) 1wt% potassium treatment

the other products represented with PC2 also increases, however, at a much lower rate. The increased activation energies for both reactions, result in decreased amount of condensables. These results are consistent with the decreased oil yield from a fluidized-bed reactor reported by Scott et al., [6]. The strong inhibition of levoglucosan formation results in the increased yield of acids and aldehydes, as shown in Figure 8.8. The increased weight fraction of acids and aldehydes caused by potassium has previously been reported by Patwardhan et al., [40]. Higher activation energy also leads to the delay in the onset of PC1 formation relative to PC2 formation (Figure 8.8 c and d).

The char yield was determined by weighing the solid residue after the experiment. As shown in Figure 8.10, char yield increases from 3.7 wt% of the pure cellulose sample to 14.0 wt% of the sample treated with 1 wt% potassium. The temperature had a negligible effect on the char yield within the considered range between 480-520°C. The char yield data were used to determine the activation energy of the char formation reaction as a function of potassium

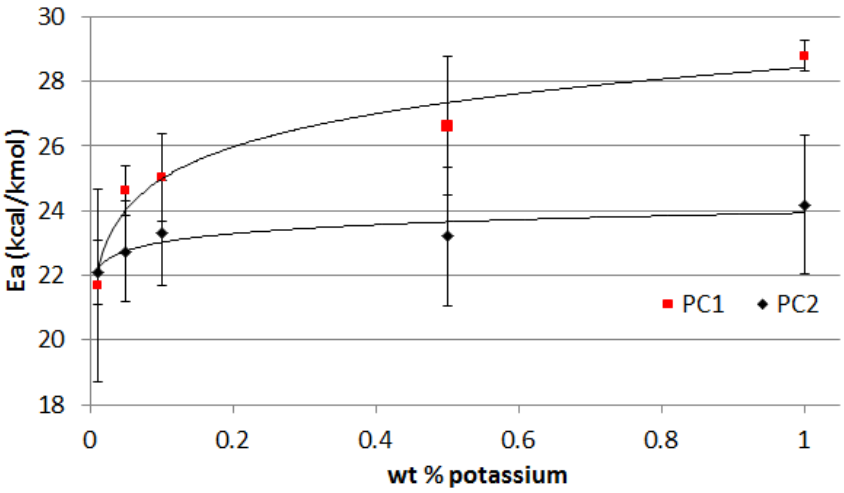

Figure 8.9: Activation energies for the formation of principal components PC1 and PC2 as a function of the level of potassium treatment

treatment. The activation energy for the char formation was calculated by matching the predicted char yields with the experimental data.

The determined activation energies and pre-exponential factors were incorporated into the cellulose pyrolysis mechanism developed by Ranzi et al., [87]. The original mechanism, shown in Figure 8.11 (a), is comprised of four reactions. Firstly, cellulose is partially depolymerized according to reaction (R1). Next, the active cellulose (at low degree of polymerization) undergoes either depolymerization leading to levoglucosan formation (R3) or fragmentation leading to the formation of acids, aldehydes, other volatiles and char (R2). In addition to this pathway, there is a competing dehydration reaction, which leads to formation of char (cross-linking) and water (R4). The products of the dehydration reaction usually also include gases [17, 92], which are missing in the presented mechanism. Therefore an additional adjustment was made in the reaction stochiometry to incorporate the produced CO, CO_2, and H_2, as shown in Figure 8.11 (b). The activation energies of reactions R2, R3 and R4 were adjusted, as functions of potassium treatment based on the experimental data. The activation energies of reactions R2 and R3 increase with the increased potassium treatment,

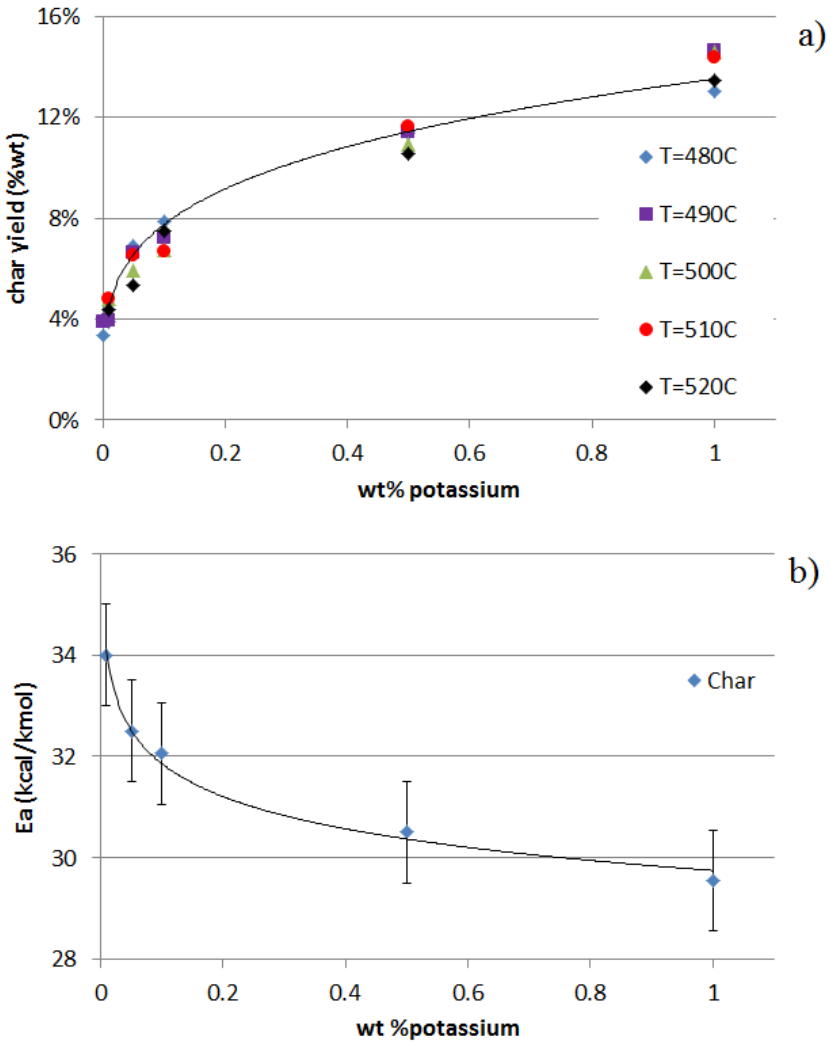

Figure 8.10: The effect of potassium treatment on a) char yield, b) activation energy of char formation

since potassium strongly inhibits levoglucosan formation (R3) and mildly inhibits the fragmentation reaction (R2). The activation energy of the dehydration reaction (R4) decreases as it is catalyzed by potassium. The activation energies and pre-exponents of reactions R2, R3 and R4 for pure cellulose are summarized in Table 8.3. Since the activation energies of reactions R2, R3, R4 change as functions of the potassium treatment (wt% K), the following functions describing these change were obtained by fitting the experimental data presented

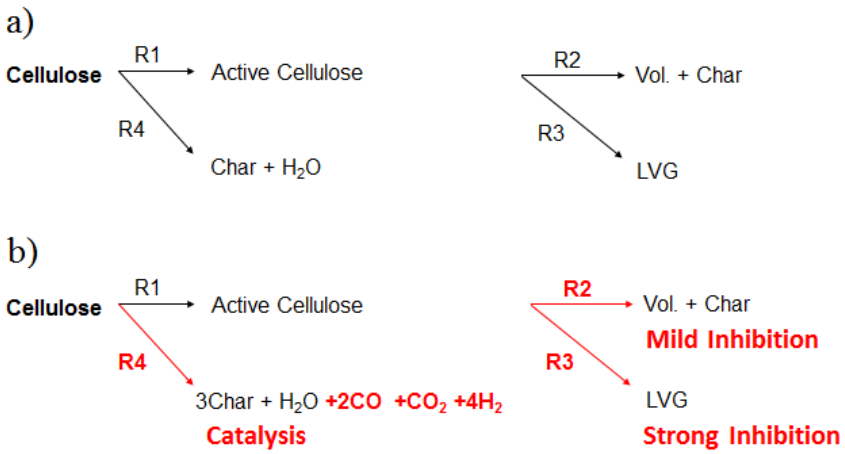

Figure 8.11: The schematic of the cellulose pyrolysis reaction mechanism a) original mechanism [87], b) mechanism with adjustments for the effect of potassium

Table 8.3: Activation energies and pre-exponents of reactions R2, R3, R4 for pure cellulose

Reaction	Activation Energy (kJ/mol)	Pre-exponent (1/s)
R2	93.6±9.6	$3.78 \cdot 10^9$
R3	90.8±0.8	$2.61 \cdot 10^9$
R4	142.3±2.1	$2.00 \cdot 10^9$

in Figure 8.9 and 8.10 (b):

$$E_{a,2}(wt\%K) = 100.16x^{0.0168} \tag{8.4}$$

$$E_{a,3}(wt\%K) = 118.99x^{0.056} \tag{8.5}$$

$$E_{a,4}(wt\%K) = 124.52x^{-0.03} \tag{8.6}$$

where x is the weight fraction of potassium (%).

The modified cellulose pyrolysis mechanism was implemented in Aspen Custom Modeler. Simulations were performed under isothermal conditions at 500^{o}C and the residence time of 0.5 s in order to investigate the effect of potassium on cellulose pyrolysis products in more details. Simulation results show that the increased potassium treatment causes a dramatic

reduction in the oil yield from 87.9 wt% from untreated avicel to 54.0 wt% at 0.5 wt% potassium treatment. Further increase in potassium treatment causes a further decrease in the oil yield to 46.2 wt% at 1 wt% potassium treatment. The decrease of the oil yield is accompanied by an increase of the gas and char yield. The predicted char yield increases from 3.7 wt% from pure avicel to 14.0 wt% at 1 wt% potassium treatment and the gas yield increases from 8.4 wt% from pure avicel to 39.8 wt% at 1 wt% potassium treatment, as shown in Figure 8.12 (a).

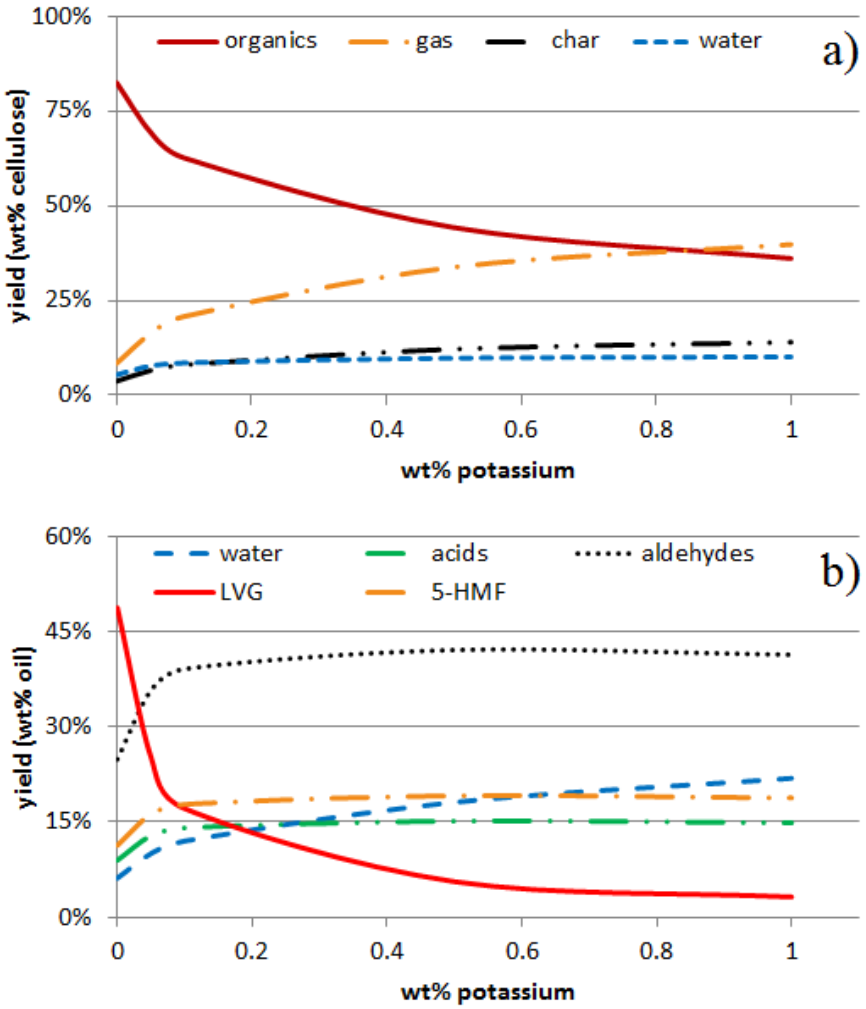

Figure 8.12: Prediction of the effect of potassium treatment on a) product yield, b) oil composition from fast pyrolysis of cellulose at 500^{o}C and 0.5 s residence time

The composition of the produced pyrolysis oil is also altered in the presence of potassium. The predicted levoglucosan weight fraction decreases dramatically from 48.8 wt% of the produced oil from pure cellulose to only 5.6 wt% of the oil at 0.5 wt% potassium treatment, as shown in Figure 8.12 (b). Further increase in the potassium treatment causes further decrease in the levoglucosan yield to 3.1 wt% at 1 wt% potassium treatment. The large initial drop of the predicted levoglucosan yield supports the theory that potassium inhibits the unzipping reactions of cellulose molecules. The inhibition of levoglucosan formation results in the increased yields of acids and aldehydes produced in the competing fragmentation reaction. Moreover, the heating value of the produced oil decreases with the increased potassium treatment due to increased predicted weight fraction of water from 6.1 wt% of the oil from pure cellulose to 21.9 wt % of the oil at 1 wt% potassium treatment. The increased water yield is due to both decreased yield of organics and additional water produced in the catalyzed dehydration reaction.

The simulation results were validated with the experimental data obtained from the fluidized-bed reactor [88]. The experiments were performed with avicel and 0.1 wt% potassium treated avicel. The addition of potassium caused a reduction of oil yield from 86.9 wt% to 68.8 wt%, an increase of gas yield from 13.0% to 22.9 %, and an increase of char yield from 0.1 % to 8.3%. The comparison of the experimental data with model results is given in Table 8.4. The

Table 8.4: Comparison of avicel and potassium treated avicel pyrolysis product yields from model prediction with experimental data

Product Yield	Avicel (Simulation/Experiment)	Avicel + 0.1%wt K (Simulation/Experiment)
Oil (%wt)	87.9/86.9	71.2/68.6
Char (%wt)	3.7/0.1	8.0/8.3
Gas (%wt)	8.4/13.0	20.8/22.9

model results are in excellent agreement with the experimental yields, with the differences in yields below 5 % points. This is a very good result, given the uncertainty related to the

experimental data. The standard deviation in the oil yield from the fluidized bed reactor was 7.1 % points. The mass balance closure in the pure avicel experiment and the potassium treated avicel experiment was 94.9 % and 90.4% respectively. The mass imbalance was related to the oil collection system and it was added to the oil yield in Table 8.4. The lower than expected experimental char yield is not completely unexpected since the experimental fluidized-bed reactor is susceptible to errors in the char collection system.

The validated cellulose mechanism was next integrated with the biomass pyrolysis mechanism [87]. The simulations were performed for pine, corn stover and switchgrass feedstocks. The purpose of these simulations was assess the following aspects of the proposed cellulose pyrolysis mechanism adjustment: i) the relative magnitude of the effect of inorganic compounds on cellulose compared to other biomass building blocks, ii) the relative importance of potassium among other inorganic compounds present in the biomass structure. The performed simulations could help with decisions regarding performing additional experimental work with hemicellulose and lignin in the future and performing additional experimental work with other metals (such as sodium or magnesium) in order to further adjust the reaction mechanism for improved accuracy and flexibility.

The activation energies of the cellulose pyrolysis reactions were adjusted based on the potassium content according to equations 8.4 - 8.6. The detailed information about the model parameters used in the simulations is summarized in Table 8.5. The pre-exponential factors were not affected by potassium, therefore the values given in Table 8.3 were used for simulations. The simulation results were validated with the experimental data presented in a milestone report within the Thermochemical Feedstock Interface [82]. The comparison of the simulation results and the experimental yield data given in Table 8.6 shows a good agreement between the gas and char yields. The predicted oil yield is higher compared with the experimental yields. However, it is important to notice that the comparison might be

Table 8.5: Reaction model parameters used for pyrolysis simulations of pine, corn stover and switchgrass feedstocks

Parameter	Pine	Corn Stover	Switchgrass
Ash (%wt)	0.7	4.3	4.2
Potassium (%wt)	0.03	0.36	0.27
$E_{a,2}$ (kJ/mol-K)	87.50	91.12	90.68
$E_{a,3}$ (kJ/mol-K)	75.84	86.82	85.41
$E_{a,4}$ (kJ/mol-K)	158.5	147.43	148.73

Table 8.6: Comparison of pyrolysis product yields from model prediction with experimental data for pine, corn stover and switchgrass

Product Yield	Pine (sim/exp)	Corn Stover (sim/exp)	Switchgrass (sim/exp)
Oil (%wt)	71.8/62.9	58.2/51.9	64.1/58.1
Char and Ash (%wt)	13.5/15	21.1/19.1	18.1/10.8
Gas (%wt)	14.7/18.9	20.7/22.3	17.8/18.1
Closure (%wt)	100.0/93.3	100.0/93.3	100.0/87.0

affected by the mass balance closure in the experiments and the low carbon balance. The carbon balance was 93.3 wt% of feed for pine, 76.7 wt% of feed for corn stover and 69.6 wt% of feed for switchgrass. The mass imbalance could be assigned to the oil yield because it is likely that some oil remained in the condensing stages and was not collected. The gas and char yields are more accurate unless there were some unexpected failures in the reactor system. According to the Thermochemical Feedstock Interface milestone report such a failure occurred in the char collection system in the experiments with switchgrass. This explains the low experimental char yield and the mismatch between the simulation results and the experiment.

8.4 Conclusions

An adjusted cellulose pyrolysis mechanism was proposed to account for the effect of potassium, which causes severe reduction of oil yield and has an adverse effect on the oil composition. The simulation results reveal that potassium strongly inhibits levoglucosan formation and promotes the formation of char, water and gases. As a result the predicted oil

yield decreases from 87.9 wt% achieved with pure avicel to 54.0 wt% at 0.5 wt% potassium treatment, the predicted char yield increases from 3.7 wt% to 12.1 wt% and the predicted gas yield increases from 8.4 wt% to 33.8 wt%. Moreover, the heating value of the produced oil decreases because of the increased predicted weight fraction of water from 6.1 wt% to 18.1 wt%. The simulation results were in good agreement with the experimental data from a fluidized-bed reactor. The differences in product yields were below 5 wt % on an absolute yield basis. The simulations of the pyrolysis process with the three representative biomass feedstocks and comparison with experimental results lead to the following conclusions: i) potassium is a reasonable approximation of the inorganic compounds present in biomass structure due to its strong catalytic effect and high mass fraction compared to other alkali/alkaline metals, ii) cellulose is the most severely affected by the alkali metals and correcting the cellulose pyrolysis mechanism alone is a reasonable approximation of the effect of inorganic compounds on biomass pyrolysis product yields and composition. This suggests that the underlying model with the proposed adjustments may be extended to derive practical value for predicting fast pyrolysis products in biorefinery plant simulations, especially when there are variations in ash in the supplied feedstock. However, it would be recommended to also compare the composition of the produced pyrolysis gases and oil (experimental data not available at present), and evaluate the effect of potassium of hemicellulose and lignin in the future in order to better validate these results.

CHAPTER 9

CONCLUSIONS

A 1-D, steady state model of a CFB reactor compatible for integration with biomass fast pyrolysis biorefinery models in Aspen Plus was proposed. The goal was to improve product yields and composition predictions and develop a computational tool for assistance with determining operating parameters under different design conditions.

The non-reactive simulations show that the hydrodynamically and thermally fully developed flow was achieved nearly at the reactor inlet due to high heat transfer rates and intense momentum transfer. These results were verified with higher order CFD models and validated with experimental data. Verification of hydrodynamics and heat transfer in the riser with a transient 1-D and 2-D multiphase model developed in MFIX software by Dr. Jack Ziegler at NREL leads to the following conclusions:

- 1-D models predict well gas velocity and temperature profiles along the reactor height,
- 1-D models consistently overpredict particle velocities and consequently underpredict solids volume fractions compared to the time and spatially averaged results from 2-D simulations. The discrepancies are due to particle clustering, which causes drag reduction and which is not included in the 1-D, steady-state approximation,
- 1-D model could be also applied for simulating the vapor phase upgrading reactors, as the drag model is also appropriate for modeling multiphase flows with smaller solid particles,
- parametric sweep shows that particle size and fluidizing gas composition are the most influential parameters for fluidization conditions, therefore changing particle size or gas

composition requires a careful adjustment of the fluidizing gas flow rate for maintaining fast fluidization

The verification of the external heat transfer coefficient and simplifying assumptions used for particle approximation (particles are represented with an average particle temperature) with a 3-D microstructure particle model constructed based on particle imaging by Dr. Peter Ciesielski at NREL leads to the following conclusions:

- the external heat transfer coefficient evaluated from the correlations provided in MFIX documentation might be overpredicted, since the heat transfer coefficient evaluated from single particle simulations is lower by a factor of two. Single particle simulations might on the other hand be underpredicting the heat transfer coefficient as they do not account for particle collisions.

- Heat transfer rates are still high and thermal equilibrium is also quickly reached with the reduced heat transfer coefficient evaluated from new correlations for the particle size class of 0.5 mm. However, heat transfer is significantly slower for the 2 mm size class biomass particles and external heat transfer might become rate limiting and lead to incomplete conversion of larger particles unless the residence time in the reactor is increased

- The heterogeneous nature of physical properties should not significantly affect the temperature profiles over the considered range of particle sizes.

Based on the performed analysis it can be concluded that the external heat transfer rates are high and at a sufficiently small particle sizes (< 2mm) are most likely not a limiting factor for the reaction rates or biomass conversion. At present, validation with experimental data is not possible due to the conditions in fast pyrolysis reactors and small particle size. However, should such measurements be possible in the future, validation of the heat transfer coefficient is highly recommended.

Validation of the 1-D, 2-D and 3-D simulation results with cold-flow experimental data shows that the 2-D models predict particle velocities more accurately compared to the 1-D models. This result confirms the existence of clustering and indicates the need to investigate the possibilities for adjusting the drag model in the 1-D model in order to more accurately predict particle residence time in the reactor (which is underpredicted by the model as a result of overpredicted particle velocities). A simple attempt of adjusting the drag by reducing the drag coefficient by a factor of 2 or increasing the effective particle size to 2 mm shows that the drag correction needs to be more sophisticated as the general characteristics of the particle velocity still do not match the experimental results. Although the 2-D model gives better predictions of particle velocities, the pressure drop and mass inventory are underpredicted, which implies that the drag model is still not accurate. The 3-D simulations predict lower particle velocities and lower gas volume fractions compared to the experimental data, however, the mass inventory and pressure drop in the 3-D simulations is still lower compared to the experiment. Based on the comparison of radial profiles of solids flux and particle velocities, it is suspected that this is due to the downfall of the solids at the riser wall witch is not captured in the measurements.

Biomass fast pyrolysis simulations with the developed reactor model lead to the following general conclusions about the proposed modeling methodology:

- the advantage of the 1-D model over a bulk model is that it provides the information about the temperature, mass flux and velocity profiles along the reactor height which is useful for determining the reactor height required for high biomass conversion and low vapor residence time,
- the 1-D model results show the onset of reactions, the rate of formation of individual product classes looks like and the degree of biomass conversion at the reactor outlet, which is important for better understanding the pyrolysis process and tuning the

selectivity for maximizing the yields of desired products,

- the advantage of the 1-D model over higher order CFD models is its low computational cost which allows for integration of a complex pyrolysis reaction mechanism with a reasonably accurate mathematical description of the fluid dynamics and heat transfer, the computational cost of 2-D and 3-D reactor models is preventive of resolving the formation of individual product classes along the reactor height,

- the 1-D simulation results show that the two most influential parameters for product yields and composition are the reaction temperature and biomass composition. Operating at higher temperature results in a reduced oil yield and adverse changes in the oil composition. The mass fractions of water, acids and aldehydes were higher and the mass fraction of sugar derived compounds was lower when the pyrolysis reaction temperature was higher. The employed reaction model gives good predictions of product classes for the low ash content feedstocks such as pine, however it significantly overpredicts the organics yields from high ash content feedstocks. This is because the catalytic effect of intrinsic contaminants is not included in the reactions. Therefore, the reaction mechanism should be corrected in order to improve the predictive capabilities of the model from feedstocks with high ash content.

- the 1-D simulation results show that changing the operating parameters (other than aforementioned reaction temperature and biomass feedstock) causes changes in velocity profiles, temperature profiles reaction onset and reaction rates. However, the final product yields at the reactor outlet remain unchanged provided that the residence time is sufficient for full conversion. This result will most likely change when a validated secondary reaction mechanism is available for integration with the model. The oil yield and composition will become dependent on the vapor residence time in the reactor and the developed model will become a useful tool for optimizing the operating conditions and reactor design for maximizing the oil yield and obtaining the most desirable oil

composition.

- the model could be applied to studying the catalytic vapor phase upgrading process in CFB risers, since it has been shown that the model is capable of predicting the fluid dynamics with the same accuracy to the 2-D model in MFIX. Once a reaction mechanism is available for integration it will be possible to obtain the information about the onset and progression of the catalytic reactions and formation of product classes, as well as catalyst deactivation along the reactor height, which will contribute to a better understanding of the process, enable optimization of the operating conditions and improving the reactor design.

The experimental and modeling work on the effect of potassium on cellulose pyrolysis reaction mechanism proved that potassium promotes the formation of char, water and gases and inhibits the formation of levoglucosan. The simulations of cellulose and biomass fast pyrolysis performed with the adjusted cellulose reaction mechanism show that potassium is a good approximation of the contaminants present in the biomass structure due to the high mass fraction and strong catalytic properties. The product yield predictions better match the experimental results after adjusting the cellulose reaction mechanism. This also leads to the conclusion that catalytic effect of the contaminants on the cellulose pyrolysis reactions is much stronger than the effect on hemicellulose or lignin pyrolysis reactions. However, it would be recommended to evaluate the effect of potassium on hemicellulose and lignin pyrolysis for completeness and further improvement of the model accuracy and flexibility. Moreover, it might be of interest to consider the combined catalytic effect of potassium and sodium on biomass pyrolysis, since sodium was also reported to have fairly strong catalytic properties, however the mass fractions are typically much lower than those of potassium.

Overall this work allowed the development of a representative, yet computationally compatible model for use in large process simulations. A good understanding was developed about the deficiencies introduced by the simplifying assumptions in a 1-D model; this un-

derstanding will be valuable for future improvements, as well as the choices of where such models may be applied.

REFERENCES CITED

[1] Dinesh Mohan, Charles Pittman, and Philip H Steele. Pyrolysis of wood/biomass for bio-oil: a critical review. *Energy & Fuels*, 20(3):848–889, 2006.

[2] AA Boateng. Pyrolysis oil–overview of characterization and utilization. 2014.

[3] M Ringer, V Putsche, and J Scahill. Large-scale pyrolysis oil production: A technology assessment and economic analysis. Technical report, 2006. P-510-37779.

[4] Mark M Wright, Daren E Daugaard, Justinus A Satrio, and Robert C Brown. Techno-economic analysis of biomass fast pyrolysis to transportation fuels. *Fuel*, 89:S2–S10, 2010.

[5] S. Jones, P. Meyer, A. Snowden-Swan, Padmaperuma, E. Tan, A. Dutta, J. Jacobson, and K. Cafferty. Process design and economics for the conversion of lignocellulosic biomass to hydrocarbon fuels, fast pyrolysis and hydrotreating bio-oil pathway. 2013.

[6] Donald S Scott, Jan Piskorz, and Desmond Radlein. Liquid products from the continuous flash pyrolysis of biomass. *Industrial & Engineering Chemistry Process Design and Development*, 24(3):581–588, 1985.

[7] Andrés Anca-Couce, Ramin Mehrabian, Robert Scharler, and Ingwald Obernberger. Kinetic scheme of biomass pyrolysis considering secondary charring reactions. *Energy Conversion and Management*, 87:687–696, 2014.

[8] MA Hastaoglu and MS Hassam. Application of a general gas-solid reaction model to flash pyrolysis of wood in a circulating fluidized bed. *Fuel*, 74(5):697–703, 1995.

[9] Manon Van de Velden, Jan Baeyens, and Ioannis Boukis. Modeling cfb biomass pyrolysis reactors. *Biomass and Bioenergy*, 32(2):128–139, 2008.

[10] Priyanka Kaushal and Jalal Abedi. A simplified model for biomass pyrolysis in a fluidized bed reactor. *Journal of Industrial and Engineering Chemistry*, 16(5):748–755, 2010.

[11] K Daizo and O Levenspiel. *Fluidization engineering*. Stoneham, MA (United States); Butterworth Publishers, 1991.

[12] Pelle Mellin, Efthymios Kantarelis, and Weihong Yang. Computational fluid dynamics modeling of biomass fast pyrolysis in a fluidized bed reactor, using a comprehensive chemistry scheme. *Fuel*, 117:704–715, 2014.

[13] R Panday, JL Shadle, M Ahahnam, R Cocco, A Issangya, SJ Spenik, JC Ludlow, P Gopalan, F Shaffer, M Syamlal, C Guenther, SBR Karri, and T Knowlton. Challenge problem 1 model validation of circulating fluidized beds. *Powder Technology*, 2014.

[14] Desmond Radlein and ALAIN QUIGNARD. A short historical review of fast pyrolysis of biomass. *Oil and Gas Science and Technology*, 68(4):765–783, 2013.

[15] AV Bridgwater and GVC Peacocke. Fast pyrolysis processes for biomass. *Renewable and Sustainable Energy Reviews*, 4(1):1–73, 2000.

[16] Sascha RA Kersten, Xiaoquan Wang, Wolter Prins, and Wim PM van Swaaij. Biomass pyrolysis in a fluidized bed reactor. part 1: Literature review and model simulations. *Industrial & engineering chemistry research*, 44(23):8773–8785, 2005.

[17] Colomba Di Blasi. Modeling chemical and physical processes of wood and biomass pyrolysis. *Progress in Energy and Combustion Science*, 34(1):47–90, 2008.

[18] Jacques Lédé. Biomass fast pyrolysis reactors: a review of a few scientific challenges and of related recommended research topics. *Oil & Gas Science and Technology–Revue dIFP Energies nouvelles*, 68(5):801–814, 2013.

[19] RS Miller and J Bellan. A generalized biomass pyrolysis model based on superimposed cellulose, hemicelluloseand liqnin kinetics. *Combustion Science and Technology*, 126 (1-6):97–137, 1997.

[20] Eliseo Ranzi, Alberto Cuoci, Tiziano Faravelli, Alessio Frassoldati, Gabriele Migliavacca, Sauro Pierucci, and Samuele Sommariva. Chemical kinetics of biomass pyrolysis. *Energy & Fuels*, 22(6):4292–4300, 2008.

[21] Matteo Calonaci, Roberto Grana, Emma Barker Hemings, Giulia Bozzano, Mario Dente, and Eliseo Ranzi. Comprehensive kinetic modeling study of bio-oil formation from fast pyrolysis of biomass. *Energy & Fuels*, 24(10):5727–5734, 2010.

[22] M Corbetta, S Pierucci, E Ranzi, H Bennadji, and EM Fisher. Multistep kinetic model of biomass pyrolysis. 2013. XXXVI Meeting of the Italian Section of the Combustion Institute.

[23] L Fagbemi, L Khezami, and R Capart. Pyrolysis products from different biomasses: application to the thermal cracking of tar. *Applied energy*, 69(4):293–306, 2001.

[24] Elly Hoekstra, Roel JM Westerhof, Wim Brilman, Wim PM Van Swaaij, Sascha RA Kersten, Kees JA Hogendoorn, and Michael Windt. Heterogeneous and homogeneous reactions of pyrolysis vapors from pine wood. *AIChE journal*, 58(9):2830–2842, 2012.

[25] Julien Blondeau and Hervé Jeanmart. Biomass pyrolysis at high temperatures: Prediction of gaseous species yields from an anisotropic particle. *Biomass and Bioenergy*, 41: 107–121, 2012.

[26] John G Olsson, Ulf Jäglid, Jan BC Pettersson, and Pia Hald. Alkali metal emission during pyrolysis of biomass. *Energy & Fuels*, 11(4):779–784, 1997.

[27] Pushkaraj Ramchandra Patwardhan. Understanding the product distribution from biomass fast pyrolysis. 2010.

[28] Stanislav V Vassilev, David Baxter, Lars K Andersen, and Christina G Vassileva. An overview of the composition and application of biomass ash. part 1. phase–mineral and chemical composition and classification. *Fuel*, 105:40–76, 2013.

[29] Daniel Carpenter, Tyler L Westover, Stefan Czernik, and Whitney Jablonski. Biomass feedstocks for renewable fuel production: a review of the impacts of feedstock and pretreatment on the yield and product distribution of fast pyrolysis bio-oils and vapors. *Green Chemistry*, 16(2):384–406, 2014.

[30] Gabor Varhegyi, Michael J Antal Jr, Tamas Szekely, Ferenc Till, and Emma Jakab. Simultaneous thermogravimetric-mass spectrometric studies of the thermal decomposition of biopolymers. 1. avicel cellulose in the presence and absence of catalysts. *Energy & fuels*, 2(3):267–272, 1988.

[31] Wei-Ping Pan and Geoffrey N Richards. Influence of metal ions on volatile products of pyrolysis of wood. *Journal of Analytical and Applied Pyrolysis*, 16(2):117–126, 1989.

[32] Paul T Williams and Patrick A Horne. The role of metal salts in the pyrolysis of biomass. *Renewable Energy*, 4(1):1–13, 1994.

[33] Michael Jerry Jr Antal and Gabor Varhegyi. Cellulose pyrolysis kinetics: the current state of knowledge. *Industrial & Engineering Chemistry Research*, 34(3):703–717, 1995.

[34] Fraidoun Shafizadeh. Pyrolysis and combustion of cellulosic materials. *Advances in carbohydrate chemistry*, 23:419–474, 1968.

[35] Michael Jerry Antal Jr. Biomass pyrolysis: a review of the literature part 1 carbohydrate pyrolysis. In *Advances in solar energy*, pages 61–111. Springer, 1985.

[36] SL Madorsky, VE Hart, and S Straus. Thermal degradation of cellulosic materials. *Journal of Research of the National Bureau of Standards*, 60(4):343–349, 1958.

[37] DP Fung, YOSHIO Tsuchiya, and Kikuo Sumi. Thermal degradation of cellulose and levoglucosan: the effect of inorganic stalts. *Wood Science*, 5(1):38–43, 1972.

[38] Jan Piskorz, Desmond St AG Radlein, Donald S Scott, and Stefan Czernik. Pretreatment of wood and cellulose for production of sugars by fast pyrolysis. *Journal of Analytical and Applied Pyrolysis*, 16(2):127–142, 1989.

[39] Robert J Evans and Thomas A Milne. Molecular characterization of the pyrolysis of biomass. *Energy & Fuels*, 1(2):123–137, 1987.

[40] Pushkaraj R Patwardhan, Justinus A Satrio, Robert C Brown, and Brent H Shanks. Influence of inorganic salts on the primary pyrolysis products of cellulose. *Bioresource technology*, 101(12):4646–4655, 2010.

[41] Kenneth W Ragland and Kenneth M Bryden. *Combustion engineering*. CRC Press, 2011.

[42] Colomba Di Blasi. Modeling intra-and extra-particle processes of wood fast pyrolysis. *AIChE journal*, 48(10):2386–2397, 2002.

[43] Kenneth M Bryden and Mathew J Hagge. Modeling the combined impact of moisture and char shrinkage on the pyrolysis of a biomass particle. *Fuel*, 82(13):1633–1644, 2003.

[44] AMC Janse, RWJ Westerhout, and W Prins. Modelling of flash pyrolysis of a single wood particle. *Chemical Engineering and Processing: Process Intensification*, 39(3): 239–252, 2000.

[45] Y Haseli, JA Van Oijen, and LPH De Goey. Numerical study of the conversion time of single pyrolyzing biomass particles at high heating conditions. *Chemical Engineering Journal*, 169(1):299–312, 2011.

[46] Henrik Thunman and Bo Leckner. Thermal conductivity of wood–models for different stages of combustion. *Biomass and Bioenergy*, 23(1):47–54, 2002.

[47] J Eitelberger and K Hofstetter. Prediction of transport properties of wood below the fiber saturation point–a multiscale homogenization approach and its experimental validation: Part i: Thermal conductivity. *Composites science and technology*, 71(2):134–144, 2011.

[48] B Peng, C Zhang, and J Zhu. Theoretical and numerical studies on the flow multiplicity phenomenon for gas–solids two-phase flows in cfb risers. *International Journal of Multiphase Flow*, 37(6):660–670, 2011.

[49] Shadle Mei. Cold flow circulating fluidized bed testing facility. 2011.

[50] A.V. Bridgwater, D. Meier, and D. Radlein. An overview of fast pyrolysis of biomass. *Organic Geochemistry*, 30(12):1479 – 1493, 1999.

[51] Wen-ching Yang. *Handbook of fluidization and fluid-particle systems*. CRC Press, 2003.

[52] Peter Nolan Ciesielski, Michael F Crowley, Mark R Nimlos, Aric Sanders, Gavin Wiggins, David J Robichaud, Bryon S Donohoe, and Thomas Foust. Biomass particle models with realistic morphology and resolved microstructure for simulations of intra-particle transport phenomena. *Energy & Fuels*, 2014.

[53] Jacques Lédé and Olivier Authier. Temperature and heating rate of solid particles undergoing a thermal decomposition. which criteria for characterizing fast pyrolysis? *Journal of Analytical and Applied Pyrolysis*, 2014.

[54] I Ph Boukis, P Grammelis, S Bezergianni, and AV Bridgwater. Cfb air-blown flash pyrolysis. part i: Engineering design and cold model performance. *Fuel*, 86(10):1372–1386, 2007.

[55] D Bai and K Kato. Quantitative estimation of solids holdups at dense and dilute regions of circulating fluidized beds. *Powder Technology*, 101(3):183–190, 1999.

[56] Richard C Senior and Clive Brereton. Modelling of circulating fluidised-bed solids flow and distribution. *Chemical Engineering Science*, 47(2):281–296, 1992.

[57] Todd S Pugsley and Franco Berruti. A predictive hydrodynamic model for circulating fluidized bed risers. *Powder Technology*, 89(1):57–69, 1996.

[58] Suneel K Gupta and Franco Berruti. Modeling considerations for large scale high density risers. *Fluidization IX, Engineering Foundation, New York*, pages 189–194, 1998.

[59] Suneel K Gupta and Franco Berruti. Evaluation of the gas–solid suspension density in cfb risers with exit effects. *Powder Technology*, 108(1):21–31, 2000.

[60] H Kagawa, H Mineo, R Yamazaki, and K Yoshida. A gas-solid contacting model for fast fluidized bed. *Circulating fluidized bed technology III*, pages 551–556, 1991.

[61] Gregory S Patience and Jamal Chaouki. Gas phase hydrodynamics in the riser of a circulating fluidized bed. *Chemical engineering science*, 48(18):3195–3205, 1993.

[62] J Werther, EU Hartge, and M Kruse. Gas mixing and interphase mass transfer in the circulating fluidized bed. *Fluidization VII*, pages 257–264, 1992.

[63] S Ouyang, X-G Li, and OE Potter. Circulating fluidized bed as a catalytic reactor: experimental study. *AIChE Journal*, 41(6):1534–1542, 1995.

[64] J Talukdar, P Basu, and E Joos. Sensitivity analysis of a performance predictive model for circulating fluidized bed boiler furnace. *Circulating fluidized bed technology IV*, pages 450–457, 1994.

[65] H Schoenfelder, J Werther, J Hinderer, and F Keil. A multi-stage model for the circulating fluidized bed reactor. In *AIChE Symposium Series*, volume 90, pages 92–104. New York, NY: American Institute of Chemical Engineers, 1971-c2002., 1994.

[66] David MJ Puchyr, Anil K Mehrotra, Leo A Behie, and Nicolas E Kalogerakis. Modelling a circulating fluidized bed riser reactor with gassolids downflow at the wall. *The Canadian Journal of Chemical Engineering*, 75(2):317–326, 1997.

[67] A Gianetto, S Pagliolico, Giorgio Rovero, and Bernardo Ruggeri. Theoretical and practical aspects of circulating fluidized bed reactors (cfbrs) for complex chemical systems. *Chemical Engineering Science*, 45(8):2219–2225, 1990.

[68] S Ouyang, J Lin, and OE Potter. Ozone decomposition in a 0.254 m diameter circulating fluidized bed reactor. *Powder Technology*, 74(1):73–78, 1993.

[69] YY Lee and T Hyppanen. A coal combustion model for circulating fluidized bed boilers. In *Proceedings of the Tenth International Conference on Fluidized Bed Combustion*, volume 2, pages 753–764, 1989.

[70] S Pagliolico, M Tiprigan, Giorgio Rovero, and A Gianetto. Pseudo-homogeneous approach to cfb reactor design. *Chemical engineering science*, 47(9):2269–2274, 1992.

[71] V Weiss and FN Fett. Modeling the decomposition of sodium bicarbonate in a circulating fluidized bed reactor. In *Circulating Fluidized Bed Technology*, pages 167–172. Pergamon Press Toronto, 1986.

[72] James R Muir, Clive Brereton, John R Grace, and C Jim Lim. Dynamic modeling for simulation and control of a circulating fluidized-bed combustor. *AIChE Journal*, 43(5): 1141–1152, 1997.

[73] Umberto Arena, Riccardo Chirone, Matteo D'Amore, Michele Miccio, and Piero Salatino. Some issues in modelling bubbling and circulating fluidized-bed coal combustors. *Powder technology*, 82(3):301–316, 1995.

[74] W Zhang, Y Tung, and F Johnsson. Radial voidage profiles in fast fluidized beds of different diameters. *Chemical Engineering Science*, 46(12):3045–3052, 1991.

[75] Peijun Jiang, Hsiaotao Bi, Rong-Her Jean, and Liang-Shih Fan. Baffle effects on performance of catalytic circulating fluidized bed reactor. *AIChE journal*, 37(9):1392–1400, 1991.

[76] Qingluan Xue, TJ Heindel, and RO Fox. A cfd model for biomass fast pyrolysis in fluidized-bed reactors. *Chemical Engineering Science*, 66(11):2440–2452, 2011.

[77] Q Xue, D Dalluge, TJ Heindel, RO Fox, and RC Brown. Experimental validation and cfd modeling study of biomass fast pyrolysis in fluidized-bed reactors. *Fuel*, 97:757–769, 2012.

[78] S Ouyang, X Li, and O Potter. Investigation of ozone decomposition in a circulating fluidized bed on the basis of a core–annulus model. *Fluidization VIII Preprints*, pages 457–466, 1995.

[79] Sreekanth Pannala. *Computational Gas-Solids Flows and Reacting Systems: Theory, Methods and Practice: Theory, Methods and Practice*. IGI Global, 2010.

[80] M Syamlal, W Rogers, and T O'Brien. Mfix documentation theory guide. 1993.

[81] Rafael A Sánchez, Jannike Solsvik, and Hugo A Jakobsen. Modeling and simulation of cold flow fluidized bed reactors. *Energy Procedia*, 26:22–30, 2012.

[82] D Carpenter and A Deutch, S andAstarace. Thermochemical feedstock interface. *Internal NREL Milestone Completion Report*, 2014.

[83] Paul C Johnson and Roy Jackson. Frictional–collisional constitutive relations for granular materials, with application to plane shearing. *Journal of Fluid Mechanics*, 176: 67–93, 1987.

[84] Sofiane Benyahia, Madhava Syamlal, and Thomas J O'Brien. Study of the ability of multiphase continuum models to predict core-annulus flow. *AIChE Journal*, 53(10): 2549–2568, 2007.

[85] Joachim Lundberg and Britt M Halvorsen. A review of some exsisting drag models describing the interaction between phases in a bubbling fluidized bed. In *Proc. 49th Scand. Conf. Simulation and Modeling, Oslo University College, Oslo, Norway*, pages 7–8, 2008.

[86] K. Agrawal, P.N. Loezos, M. Syamal, and S. Sundaresan. The role of meso-scale structures in rapid gas/solid flows. *J. Fluid Mech*, 445:151–185, 2001.

[87] Eliseo Ranzi, Michele Corbetta, Flavio Manenti, and Sauro Pierucci. Kinetic modeling of the thermal degradation and combustion of biomass. *Chemical Engineering Science*, 110:2–12, 2014.

[88] GJ Schlichting. Thermochemical conversion of biomass to hydrogen via fast pyrolysis and catalytic reforming. feedstock variability for distributed reforming. *Master's Thesis at Colorado School of Mines, Department of Chemical Engineering*, 2009.

[89] The unscramblerx 10.3. *CAMO Software*, 2013.

[90] C. Ruckebusch and L. Blanchet. Multivariate curve resolution: A review of advanced and tailored applications and challenges. *Analytica Chimica Acta*, 765(0):28 – 36, 2013. ISSN 0003-2670. doi: http://dx.doi.org/10.1016/j.aca.2012.12.028.

[91] Robert J Evans, Dingneng Wang, Foster A Agblevor, Helena L Chum, and Sheryl D Baldwin. Mass spectrometric studies of the thermal decomposition of carbohydrates using 13 c-labeled cellulose and glucose. *Carbohydrate research*, 281(2):219–235, 1996.

[92] Manon Van de Velden, Jan Baeyens, Anke Brems, Bart Janssens, and Raf Dewil. Fundamentals, kinetics and endothermicity of the biomass pyrolysis reaction. *Renewable energy*, 35(1):232–242, 2010.

APPENDIX A - BIOMASS PYROLYSIS REACTIONS

Reaction	*Kinetic constant [1/s]*	ΔH^0_R *[kJ/kg]*
CELL→CELLA	$4 \times 10^{13} \exp(-45000/RT)$	0
CELLA→.8HAA+.2GLYOX+.1C_2H_4O+.25HMFU+.3C_3H_6O+.21CO_2 +.1H_2+.4CH_2O+.16CO+.1CH_4+.83H_2O+.02HCOOH+.61Char	$5\times10^{8} \exp(-29000/RT)$	620
CELLA→LVG	$1.8\times T \exp(-10000/RT)$	364
CELL→5H_2O+6Char	$4\times10^{7} \exp(-31000/RT)$	-1913
HCE→.4HCE1+.6HCE2	$3.3\times10^{9} \exp(-31000/RT)$	100
HCE1→.025H_2O+.5CO_2+.025HCOOH+.5CO+.8CH_2O+.125C_2H_5OH+. 1CH_3OH+.25C_2H_4+.125H_2+.275CO_2+.4COH_2 +.45CH_3OH+.325CH_4+.875Char	$1\times10^{9} \exp(-32000/RT)$	-92
HCE1→.25H_2O+.5CO_2+.05HCOOH+.3CO+.15CO+.25CO_2 +1.7COH_2+.625CH_4+.375C_2H_4+.675 Char	$.05\times T \exp(-8000/RT)$	-1860
HCE1→XYLAN	$.9\times T \exp(-11000/RT)$	588
HCE2→.2H_2O+.175CO+.275CO_2+.5CH_2O+.1C_2H_5OH+.2HAA +.025HCOOH+.25CH_4+.3CH_3OH+.275C_2H_4+.4CO_2+.925COH_2+Char	$3.3\times10^{9} \exp(-33000/RT)$	212
LIGC→.35LIGCC+.1COUMARYL0.08PHENOL+.41C_2H_4+H_2O +.3CH_2O+.32CO +.7COH_2+0.495CH_4+5.735Char	$1.33\times10^{15} \exp(-48500/RT)$	-490
LIGH→LIGOH+C_3H_6O	$6.7\times10^{12} \exp(-37500/RT)$	100
LIGO→LIGOH+CO_2	$3.3\times10^{8} \exp(-25500/RT)$	446
LIGCC→.3COUMARYL+.2PHENOL+.35HAA+.7H_2O+.4CO +.65CH_4+.6C_2H_4+COH_{20}+.4CO+6.75Char	$1.6\times10^{6} \exp(-31500/RT)$	-503
LIGOH→LIG+.15H_2+.9H_2O+.1CH_4+.5CH_3OH+.5CH_3OH +.05CO_2+.3CO+CO+.05HCOOH+.6COH_2+.35CH_4 +.2C_2H_4+4.15Char	$5\times10^{7} \exp(-30000/RT)$	-120
LIGOH→1.5H_2O+.5CO+.1CH_4+.5H_2+1.6CO+3.9COH_2 +1.65CH_4+.3C_2H_4+.5CH_3OH +10.15Char	$33. \exp(-15000/RT)$	-1604
LIG→FE2MACR	$2.4\times T \exp(-12000/RT)$	686
LIG→.95H_2O+.2CH_2O+.4CH_3OH+CO+.2CH_4+.05HCOOH +.45CO+.5COH_2+.4CH_4+.65C_2H_4+.2C_2H_4O +.2C_3H_6O+5.5Char	$4\times10^{8} \exp(-30000/RT)$	-470
LIG→.6H_2O+.4CO+.2CH_4+.4CH_2O+.2CO+.4CH_4 +.5C_2H_4+.4CH_3OH+2COH_2+6Char	$.083\times T\times\exp(-8000/RT)$	-1663

Figure A.1: Biomass fast pyrolysis reaction mechanism

APPENDIX B - PARAMETRIC STUDY OF FLUIDIZATION IN A RISER

B.1 The Effect of Elevated Pressure on Fluidization

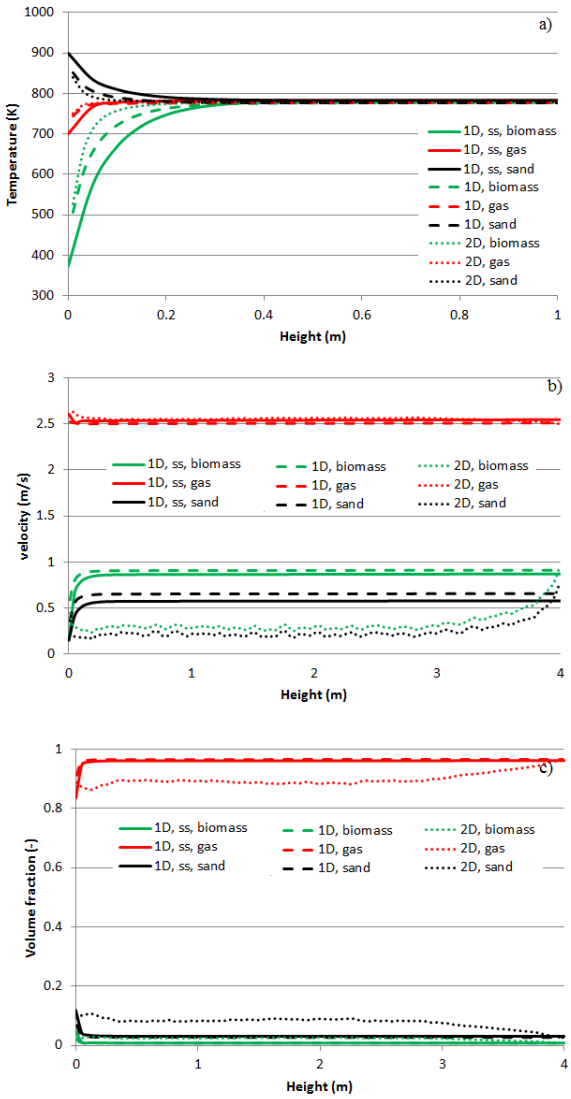

Figure B.1: Comparison of the simulation results between the 1-D steady state model, averaged 1-D transient MFIX model and averaged 2-D transient MFIX model at fluidizing gas pressure of 8.5 bar a) temperature profiles, b)velocity profiles, b) volume fraction profiles

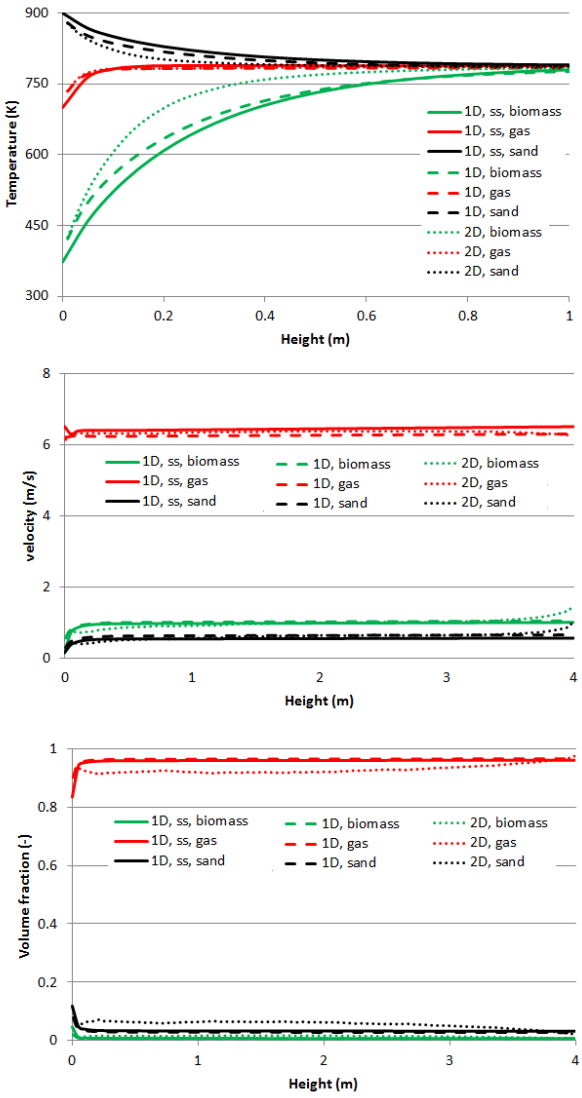

Figure B.2: The Effect of Particle Size on Fluidization. Comparison of the simulation results between the 1-D steady state model, averaged 1-D transient MFIX model and averaged 2-D transient MFIX model with particle size of 1mm a) temperature profiles, b)velocity profiles, b) volume fraction profiles

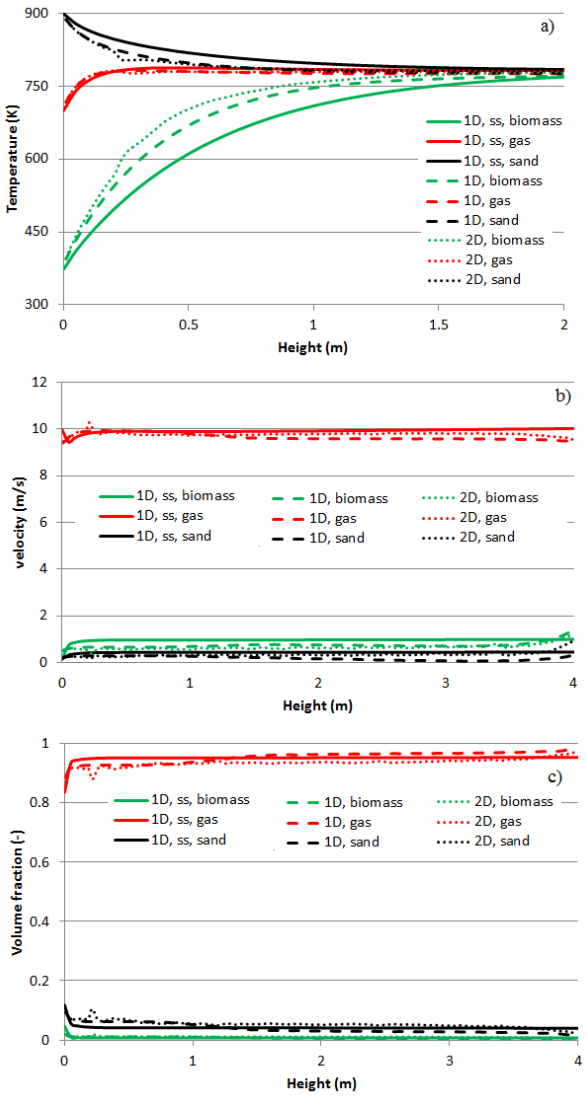

Figure B.3: The Effect of Particle Size on Fluidization. Comparison of the simulation results between the 1-D steady state model, averaged 1-D transient MFIX model and averaged 2-D transient MFIX model with particle size of 1mm a) temperature profiles, b)velocity profiles, b) volume fraction profiles

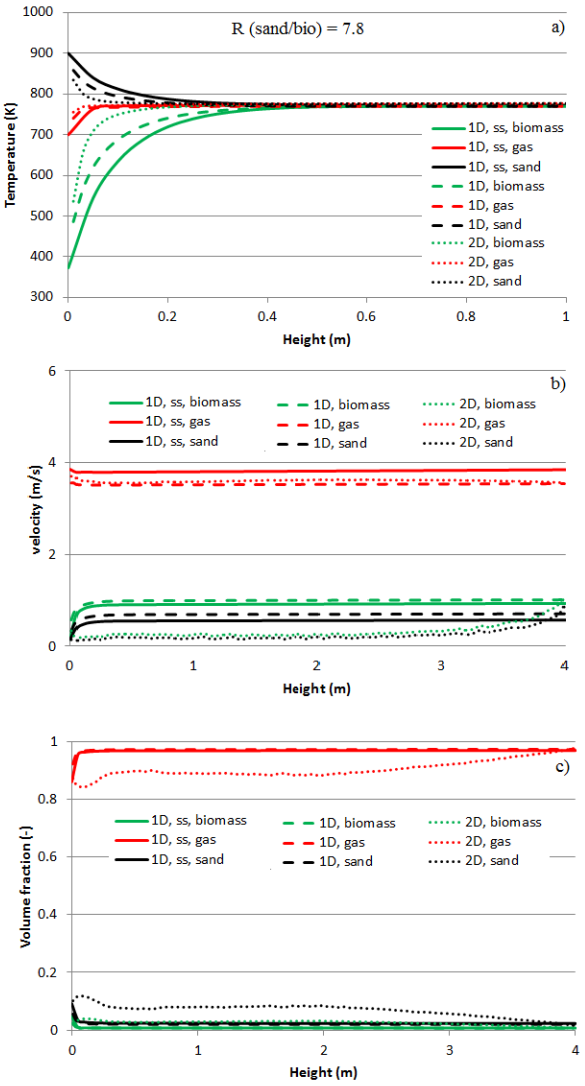

Figure B.4: The Effect of Sand-to-Biomass Ratio on Fluidization. Comparison of the simulation results between the 1-D steady state model, averaged 1-D transient MFIX model and averaged 2-D transient MFIX model with sand-to-biomass ratio of 7.8 a) temperature profiles, b)velocity profiles, b) volume fraction profiles

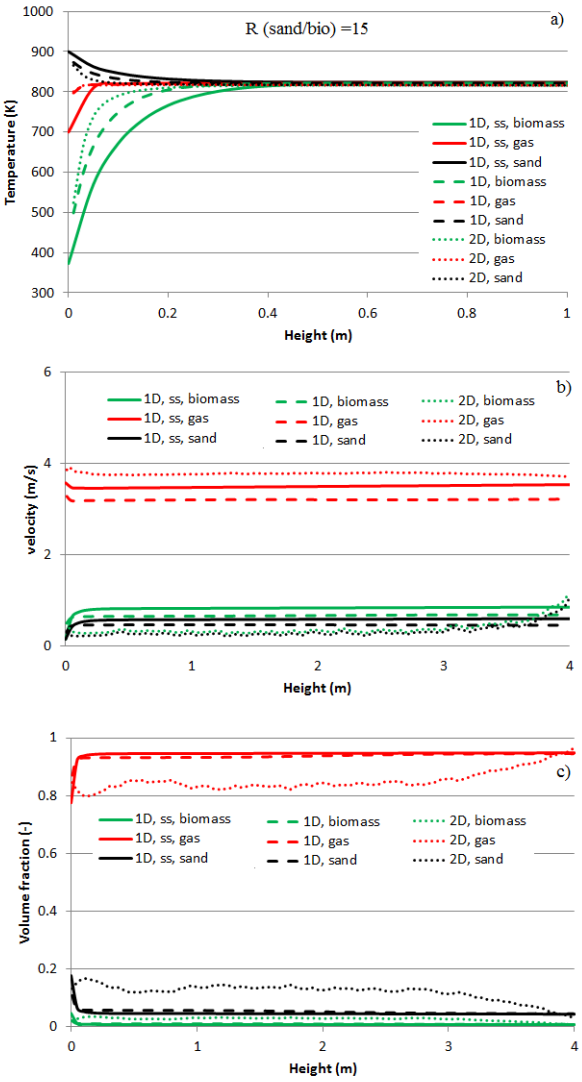

Figure B.5: The Effect of Sand-to-Biomass Ratio on Fluidization. Comparison of the simulation results between the 1-D steady state model, averaged 1-D transient MFIX model and averaged 2-D transient MFIX model with sand-to-biomass ratio of 15 a) temperature profiles, b)velocity profiles, b) volume fraction profiles

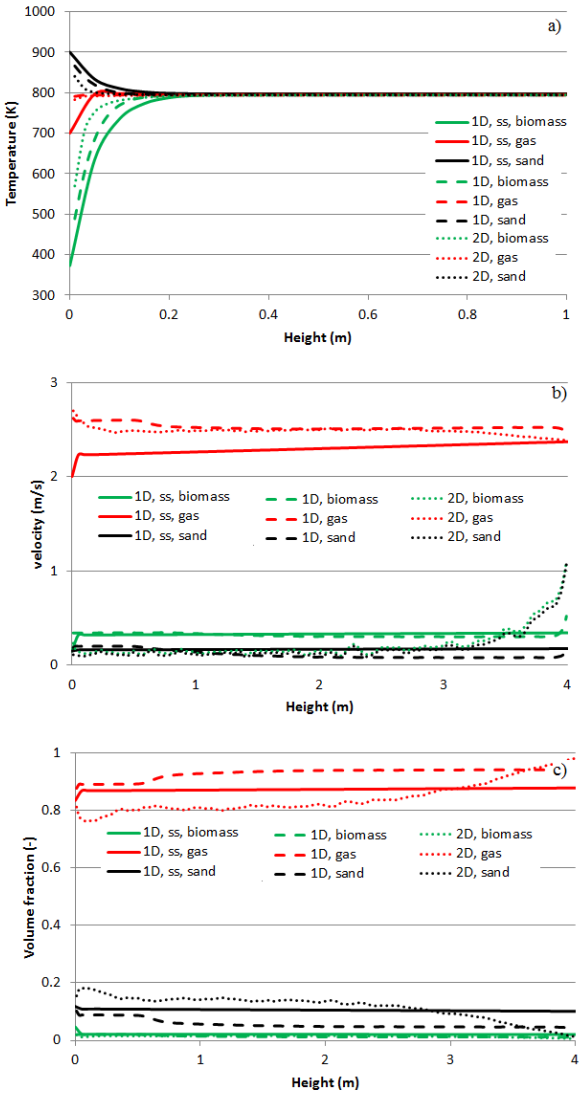

Figure B.6: The Effect of Gas-to-Biomass Ratio on Fluidization. Comparison of the simulation results between the 1-D steady state model, averaged 1-D transient MFIX model and averaged 2-D transient MFIX model at gas-to-biomass ratio of 0.5 a) temperature profiles, b)velocity profiles, b) volume fraction profiles

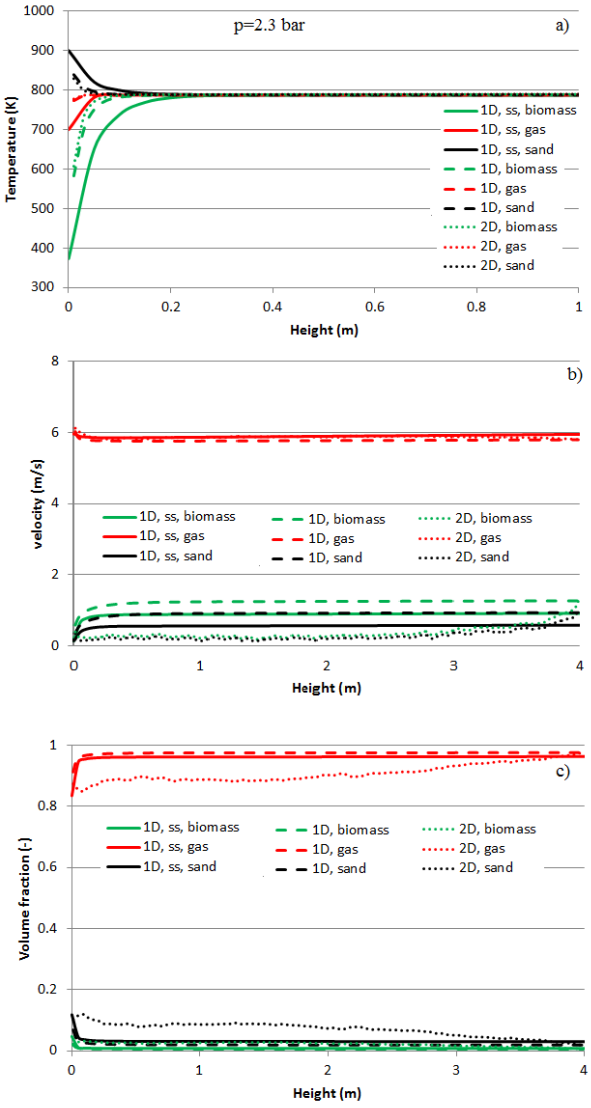

Figure B.7: The Effect of Hydrogen Addition on Fluidization. Comparison of the simulation results between the 1-D steady state model, averaged 1-D transient MFIX model and averaged 2-D transient MFIX model with hydrogen rich gas at 2.3 bar a) temperature profiles, b)velocity profiles, b) volume fraction profiles

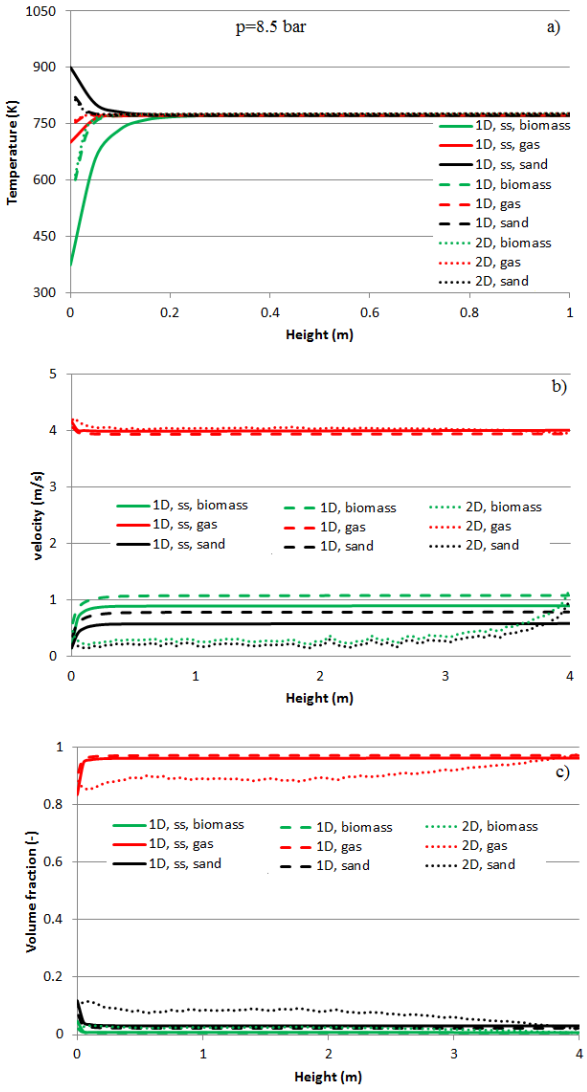

Figure B.8: The Effect of Hydrogen Addition on Fluidization. Comparison of the simulation results between the 1-D steady state model, averaged 1-D transient MFIX model and averaged 2-D transient MFIX model with with hydrogen rich gas at 8.5 bar a) temperature profiles, b)velocity profiles, b) volume fraction profiles

APPENDIX C - PARAMETRIC STUDY OF PYROLYSIS IN A RISER

C.1 The Effect of Sand-to-Biomass Ratio on Pyrolysis

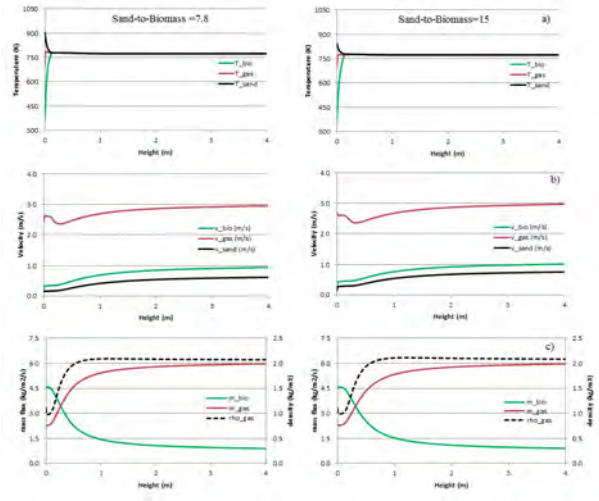

Figure C.1: The Effect of Sand-to-Biomass Ratio on Pyrolysis. Comparison of the simulation results with sand-to-biomass ratio of 7.8 (left) and 15 (right) a) temperature profiles, b)velocity profiles, b) mass flux and gas density profiles

C.2 The Effect of Gas-to-Biomass Ratio on Pyrolysis

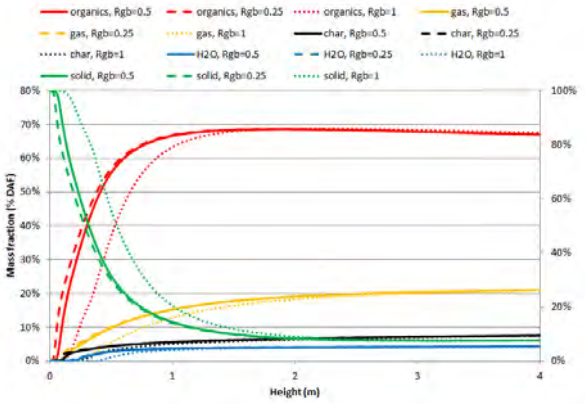

Figure C.2: The Effect of Gas-to-Biomass Ratio on Pyrolysis. Comparison of the mass fraction profiles of organics, gas, solid residue and water at gas-to-biomass ratios of 0.25, 0.5 and 1.

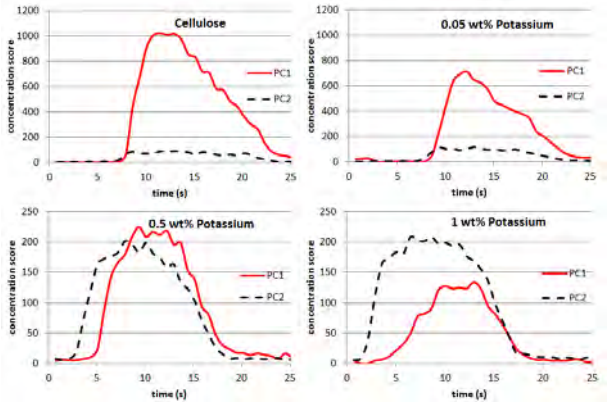

Figure D.1: Concentration profiles of principal components PC1 and PC2 at 480°C at different levels of potassium treatment; pure cellulose, 0.05wt% potassium treatment, 0.5wt% potassium treatment, 1wt% potassium treatment

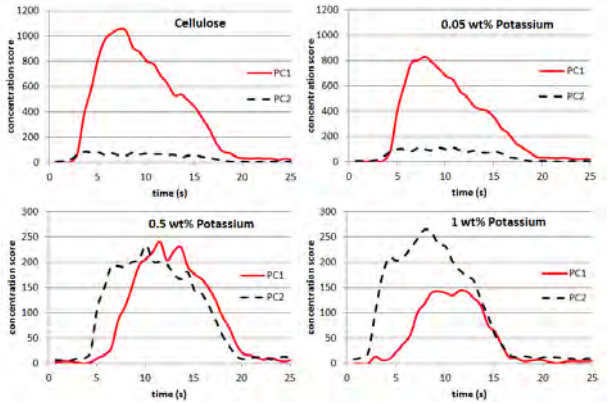

Figure D.2: Concentration profiles of principal components PC1 and PC2 at 490°C at different levels of potassium treatment; pure cellulose, 0.05wt% potassium treatment, 0.5wt% potassium treatment, 1wt% potassium treatment

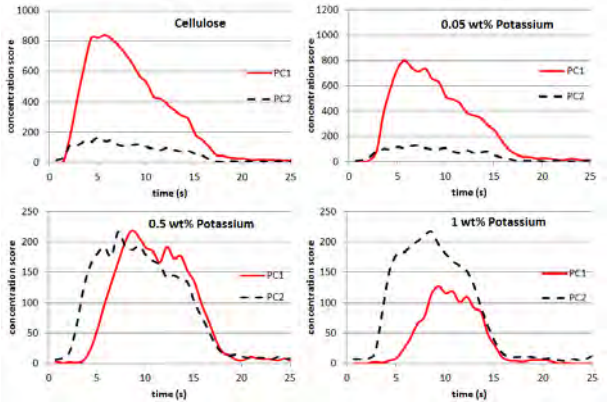

Figure D.3: Concentration profiles of principal components PC1 and PC2 at 500°C at different levels of potassium treatment; pure cellulose, 0.05wt% potassium treatment, 0.5wt% potassium treatment, 1wt% potassium treatment

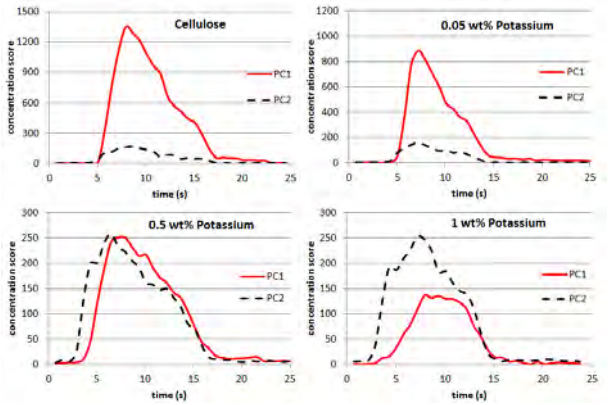

Figure D.4: Concentration profiles of principal components PC1 and PC2 at 520°C at different levels of potassium treatment; pure cellulose, 0.05wt% potassium treatment, 0.5wt% potassium treatment, 1wt% potassium treatment